1-4-2023

Measurement of Near-Threshold Proton Branching Ratios in 31S Important for Novae

Sudarsan Balakrishnan
Louisiana State University and Agricultural and Mechanical College

MEASUREMENT OF NEAR-THRESHOLD PROTON BRANCHING RATIOS IN ^{31}S IMPORTANT FOR NOVAE

A Dissertation

Submitted to the Graduate Faculty of the
Louisiana State University and
Agricultural and Mechanical College
in partial fulfillment of the
requirements for the degree of
Doctor of Philosophy

in

The Department of Physics and Astronomy

by
Sudarsan Balakrishnan
B.S&M.S.(Physics), IIT Madras, India, 2015
May 2023

Dedicated to Ammamai, to my family, and to all loved ones near and far

What's learnt, spans a handful of sand;

What's left, spans the universe

— Avvaiyar

Tamil Poet, 4th century BC

Acknowledgments

Foremost, I must express my deep gratitude to my advisors, Drs. Jeffery C Blackmon and Catherine M Deibel for their generous guidance and support throughout graduate school, for the chance to participate and gain experience in a broad roster of research, for their patience with and nurturance of my questions and ideas, and for the pleasant, co-operative, engaging and inspiring work environment during my time at LSU. I also thank the other members of my doctoral committee, Dr. Kristina Launey, Dr. Richard Litherland and Dr. Manos Chatzopoulos. A note of gratitude also to Dr. Scott T Marley for his introducing me to Experimental Nuclear Physics, and for the several enriching and informative discussions about topics on and off the field.

My sincere gratitude to everybody at FSU John D Fox Laboratory, where I performed a significant part of my research. I must, in particular, mention Dr. Ingo Wiedenhoever whose guidance, feedback, insights, and willingness to provide clarifications for my many questions during experiments I will always be thankful for. I also am indebted to Dr. Lagy Baby, Dave Caussyn, Brian Schmidt, Powell Barber, Dave Springler, Jason Aragon and Richard Boisseau for helping us put together experiments from scratch, and sharing the immense wealth of their experience to help get us back on track during snags and moments of confusion.

A big thank-you goes out to LSU post-doc Kevin Macon for his invaluable assistance and participation in the run-up to and execution of this experiment, and for the many physics/computation/instrumentation insights and lessons before, during and after. Heartfelt gratitude to Will, Keilah, David, Sergio, Zach and Rachel at LSU and Samuel, Ben, Caleb, Ken, Alex C, Chris, Bryan, Jesus, Gary C, Eilens, Eli, and Catur at FSU who were generous with their time covering shifts during the experiment, and making sure nothing went wrong. Big gratitude to Gordon McCann for his several robust programming contributions and help, and to Erin Good for showing me the workings of the apparatus many times over during my initial trips to the lab and answering my many questions. I cherish memories of learning a lot from everyone's shared expertise in the early days of SPS+SABRE, helping

figure out the right approach one small insight at a time. A separate note of thanks to Khang P and Rachel M for the many fruitful discussions on data analysis subsequently, and for all the office banter.

A kind note of gratitude to the many good souls that recruited and reminded the author to keep life light-hearted and memorable during the grind of graduate school. Particular mention to Eklavya, Sahil and Karunya for the many laughs, rants, banter, and passionate discussions over food, drinks and bus/cab trips around town. A million thanks to Jivante O and Brice F for helping me overcome my difficulty with driving a little, and for accompanying me to purchase a car. Hat-tip to Anthony B, Siddharth S, Eneet K, Kevin J, Siddhartha Das, Kunal S, Vishal K, Emily J, Kevin K, Tyler E, Graeme M, Thomas R, Ashley H, Alex L, Grigor S, David K, Kevin B, David A, Yessie G, Anthony G, Raven N, David Munoz, Kristina R, Danny Cruz, Anushka S, WJ Khoo, Justin PJ, Ishani M, Akhil B, Ogooluwa A, David I, Mohan D, Anjira S, Isam K, Manjishtha B, Tarun S, Arshad N, Anoop V, Aditya T, Rinshad K, Deepak M, Karthik R, Abhijith T, and others I worry I may have missed, for their many little acts of humanity and friendship that added up to much more than the sum of their parts.

My greetings, love and gratitude to my parents and extended family for their constant love, encouragement and support even through their occasional amusement and confusion at physics research. Much love to my brother and his family for all the jokes, humor, goodwill and encouragement. Lastly, my humble greetings to the fabled, animated mystery sleeping within all matter that bears silent witness to the world, and invites hearts and souls to go seeking its nature.

Table of Contents

List of Tables

Abstract

Classical novae are stellar explosions that contribute to the nucleosynthesis of isotopes on the proton-rich side of the valley of stability up to ^{40}Ca. In ONe novae, the incompletely understood reaction rate of ^{30}P(p,γ)^{31}S is known to strongly influence the production rate of several stable isotopes such as ^{30}Si, ^{31}P, and ^{32,33,34}S. A precise measurement of this reaction rate has several potential implications towards matching astrophysical observables to the physical composition of the nova site – the observed elemental abundance ratios of O/S and S/Al have been suggested as useful 'thermometers' to gauge the temperature of nova explosions, while the Si/H ratio observed is predicted to be correlated with the degree of mixing between accreted hydrogenic matter and the heavier elements in the white-dwarf surface. In addition, the abundance of ^{30}Si relative to ^{28}Si has been suggested as a potential tracer to distinguish between pre-solar meteoritic grains with ONe nova origins and grains with supernova/solar origins. We used the Super Enge Split-pole spectrograph (SE-SPS) at Florida State University to study levels close to the proton threshold of ^{31}S using the ^{28}Si(^{6}Li, t)^{31}S transfer reaction. The Silicon Array for Branching Ratio Experiments (SABRE) was used to detect protons emitted from unbound states in ^{31}S, in coincidence with tritons detected at the focal plane of the SE-SPS. Decay protons from the E_x = 6.636 MeV resonance in ^{31}S were observed for the first time. The measured ^{31}S level structure, proton-branching ratios and spin-parities were used to determine an updated ^{30}P(p,γ)^{31}S reaction rate.

Chapter 1. .Introduction

The origin of matter in the universe and its distribution has enjoyed considerable interest as an open question in physics, in pursuit of which extensive observation and analysis of solar and stellar spectra have been performed over many decades. This data, along with careful measurements of isotopic abundances within the earth's crust and other objects in the solar system, has aided the efforts to systematically tabulate isotopic abundances found within our Galaxy. The first attempts to arrive at a distribution of cosmic elemental abundances were taken up by Goldschmidt, Russel and Brown, among others, and their findings were systematized in a 1956 review by Suess and Urey [1]. In these works, the resulting elemental/isotopic abundance pattern as a function of the atomic/mass number was seen to have a nearly identical profile for all population I stars and interstellar media — a pattern which was labeled the 'cosmic abundance pattern' (CAP). (Population I stars refer to the younger stars in the Galaxy, that have been formed much later following the Big Bang. Studying these stellar objects helps us identify the chemical composition of the universe as it is today. [2])

Parallel to the emergence of the CAP, the field of nuclear astrophysics began to emerge with some of its major goals being to understand the details of microscopic nuclear phenomena taking place in different cosmic environments, and using those data to provide a coherent explanation for the observed CAP. The field of nuclear astrophysics was summarized in detail for the first time in a collection of seminal papers published in 1957 by Burbidge, Burbidge, Fowler and Hoyle (B^2FH), and by Cameron [3, 4, 5], which described the various processes by which the synthesis of heavier elements took place within stars by nuclear fusion as opposed to their synthesis during the Big Bang. This particular hypothesis of a continuously evolving universe with active nucleosynthesis sites proved to be extremely consistent with astronomical observations, and to date the field has evolved to accommodate a vast majority of newly observed stellar phenomena.

In B^2FH and subsequent works, several key processes that drive nucleosynthesis were

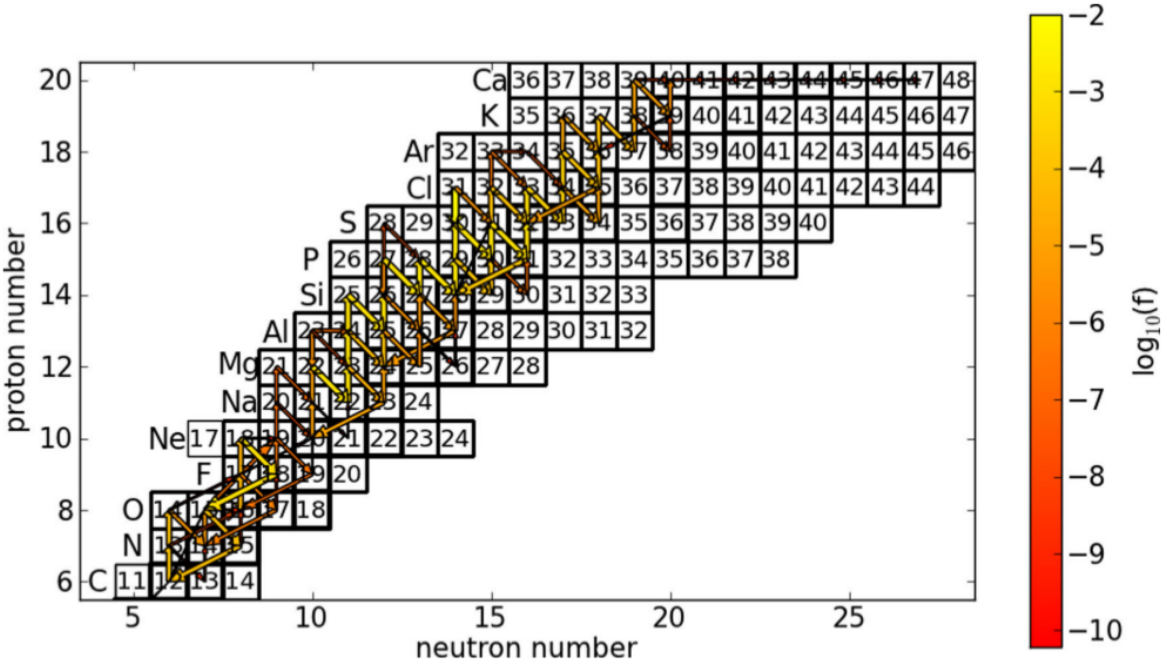

Figure 1.1. Chart of nuclides showing a typical ONe nova reaction network. The boxes with bold boundaries are stable nuclei. The arrows pointing down-right are beta decays, straight-up are proton captures, and down-left are (p, α) reactions. The colour of the arrow represents the variation rate (f) in final abundances due to the reaction. Larger values of 'f' indicate a more significant contribution of the reaction to the final abundance distribution. Figure reproduced from [6].

identified at different regions in the chart of nuclides. This helped make the study of stellar burning more systematic, since each of these processes required particular physical conditions. Knowledge of these necessary physical conditions and comparisons with observed astronomical data indicating elemental abundances in stars helped point to the possible stellar environments that drive the synthesis of particular isotopes, and refine our understanding of these processes in light of new observations. In addition, the energy scales and precision required to measure some of the astrophysically relevant nuclear reactions were found to be within reach of available nuclear physics experimental capabilities, which kick-started efforts to utilize laboratory-measured nuclear reaction data in macroscopic models of various stellar burning scenarios when possible.

Starting with early attempts by Hoyle in 1954 to predict known relative elemental abundances using nuclear reaction cross-sections [7], significant progress has been made to date in our ability to combine astronomical data, nuclear reaction inputs and inferred information regarding the chemical/physical conditions that exist in various sites of nucleosynthesis to generate light-curves and spectra of observed stellar objects/events, and use the results to model the observed CAP with increasing accuracy. The precise nature of nucleosynthesis occurring within particular sites can be quite diverse — within most main-sequence stars, as lighter elements fuse to form heavier isotopes, the radiation pressure of the energy released helps balance the gravitational instability of stellar matter against collapse. This process of hydrostatic burning thus proceeds along the line of stability over longer periods of time. By way of contrast, in explosive events such as X-ray bursts, classical novae or Type Ia supernovae, nucleosynthesis proceeds via thermonuclear runaway (TNR), synthesizing a large multitude of isotopes within a short period of time (e.g. seconds to days). For the interested reader, the review articles [8, 9] offer a detailed summary of the history, present status, and open problems in stellar nucleosynthesis.

Thus, the universe as we know it today can be regarded as an aggregate of several interesting sites where heavier isotopes are being synthesized from lighter ones via nuclear

reactions, the rates of some of which are measurable in laboratory experiments. The identification and measurement of key nuclear-reaction cross-sections at astrophysically relevant energy scales has hence been a major focus of nuclear astrophysics. In addition to nuclear reaction rates, details regarding the chemical and physical conditions (temperature, density, phase of matter, presence/absence of convection leading to mixing of matter between layers) in the particular stellar environment, as well as initial 'seed' abundances of nuclei present, are used in modern numerical models of nucleosynthesis for various stellar objects [10].

As these models improve, they've been better able to explain features in the observed elemental abundance pattern. This in turn has aided in our understanding of the chemical evolution of our Galaxy via the comparison of elemental abundances seen in stars of varying ages indicating the elemental distribution at different epochs during galactic evolution. The theory of stellar nucleosynthesis has been robust enough to incorporate a host of new observations such as the observation of characteristic γ rays in the interstellar medium [11], the presence of rare-earth elements in the outer layers of asymptotic giant branch stars [12], and exotic, non-solar abundance patterns observed in some meteoritic grains (see references within [13]). The next section will focus on a particular region of the chart of nuclides, concerning the nucleosynthesis of elements up to ^{40}Ca via thermonuclear runaway in classical novae (see Fig. 1.1).

1.1. Classical Novae

Hydrostatic equilibrium within stars ensures a balance between gravitational attraction and radiation pressure, which can cool the star via expansion when the pressure becomes higher. Most nuclear burning scenarios in sun-like stars (T<<0.1GK, rich in hydrogen) are hence determined by the timescale of proton-captures onto heavier nuclei. The beta-decay lifetimes of the proton-capture byproducts are the only other important nuclear timescale in the scenario. Since the beta-decay lifetimes are typically much faster than the mean proton-capture timescales, nucleosynthesis in these conditions ensure that the unstable products

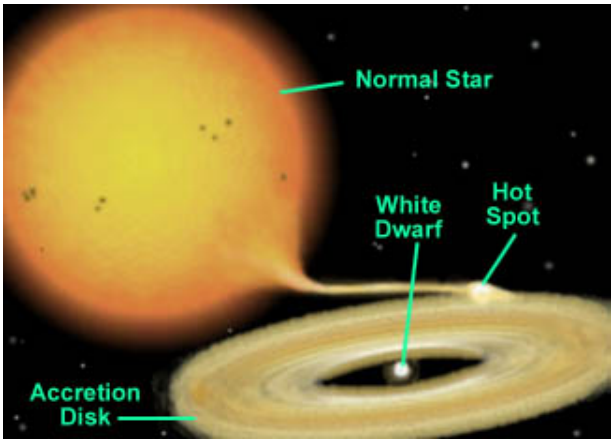

Figure 1.2. Schematic of a binary star system leading to a classical nova explosion. Reproduced from [15].

decay back to the valley of stability before undergoing a proton capture again, leading to a steady synthesis of nuclei along the valley of stability. By way of contrast, in elevated temperature/density conditions as found in, e.g., X-ray bursts and classical novae, nucleosynthesis of isotopes far away from the valley of stability can occur, synthesizing nuclei up to the proton-drip line in some cases[14].

Classical novae occur in accreting binary stars where the donor is a hydrogen-rich star, and the recipient is a white dwarf (see Fig. 1.2). As accreting stellar matter makes contact with the recipient's surface at high velocities, it builds up an envelope that undergoes compression and a new series of nucleosynthetic processes can now take place at the white dwarf's surface. The degenerate nature of the compressed matter found in the white dwarf prevents it from cooling via expansion as the temperature begins to rise due to nuclear reactions. Thus, the temperature and density at the site of accretion increases without being regulated by expansion, and this eventually sets up convection currents and a thermonuclear runaway (TNR) at temperatures of ≈0.1-0.4GK. This TNR drives the outbursts known as nova explosions, observed as large increases in luminosity ($L > 10^4 L_\odot$) that can last anywhere from a few days to a few hundreds of days. A nova explosion typically ejects 10^{-4} to 10^{-5} solar masses worth of matter into the interstellar medium. After the outburst, the

binary system is left largely intact, and the phenomenon can recur with a period of 10^4–10^5 years [9]. The temperature and luminosity observed, and the types of nuclear reactions that occur in novae depend on the rate of mass accretion, and the elemental composition of the recipient white-dwarf star — CO or ONe [14]. This is discussed in more detail in the next subsection.

1.1.1. Using numerical models to study nucleosynthesis in classical novae

CO white dwarfs are abundant in elements up to oxygen, with no significant presence of higher Z elements. In general, nucleosynthetic activity in novae involving these white dwarfs tends to be largely restricted to the region of $A \leq 20$, driven initially by the 'cold' (proton-capture limited) CNO cycles and subsequently by the 'hot' (β-decay limited) CNO cycles. ONe white dwarfs possess a larger proportion of heavier seed nuclei before the nova phenomenon is onset. In contrast to CO white dwarfs, the lower proportion of ^{12}C present in ONe novae reduces the initial activity within the CNO cycles — causing a slower rate of energy generation at the start, allowing the build up of accreted matter over a longer time before the TNR onset. The resultant higher density leads to higher peak temperatures attained (T$>$ 0.2 GK) in ONe novae in comparison with CO novae, which allows nuclear activity in ONe novae to extend to higher Z nuclei (up to $A = 40$). Thus, in order to model nova outbursts, we only require a limited number of nuclei to be studied, in the range $A \lesssim 40$. The nuclear process signatures required to be studied are mostly limited to 1) (p,γ) reaction cross-sections, 2) nuclear beta-decay lifetimes (See Fig. 1.1) and 3) a few (p,α) reaction cross-sections.

In contrast to main-sequence stellar burning, the absence of hydrodynamic equilibrium makes modeling novae outbursts challenging. The earliest models performed nuclear network calculations (calculations that connect the production/destruction of many nuclei in the medium at once), while varying the background temperature/density profile over time as predicted by separately performed hydrodynamic simulations of observed outbursts

('parametrized one-zone' models [14]). More recent models semi-analytically couple the numerical reaction networks to temperature/density conditions predicted by analytical models that make physical assumptions about the nature of the envelope ('hydrostatic' models). The complete numerical treatment would involve numerically modeling both parts of the problem simultaneously and coupling them. This approach, though challenging, is being attempted more often with advancements in computational methods (see Section 3 in [14]).

Robust numerical models for nova outbursts are important because in addition to shedding light on the nova phenomenon, they also allow us to: 1) predict the light curve observed and its spectral composition, and 2) pick out particular reactions from the network that have the largest impact on the synthesized isotopic abundances. Reference [16] and similar sensitivity studies (performed under suitable assumptions regarding the mass and initial composition of the white dwarf) have tabulated lists of nuclear reaction cross-sections that need precise measurement in order to lower the uncertainties in the predicted isotopic abundances within the ejected matter. To identify these important reactions, reference [16] determines which reactions lead to the largest changes in the final model abundances when their rates are varied within their currently-known uncertainties. In this study, parametrized one-zone models were used for the vast majority of reactions studied. Further, the results from these were checked for agreement with hydrodynamic models for a few select cases. (It should be noted that in the previous decade, a more rigorous evaluation of reaction-rate probability densities at all relevant temperature grid-points is being performed and updated using platforms like STARLIB [17]. Utilizing a database of probability densities as a function of physical conditions - rather than just rate uncertainties - allows for a more meaningful coupling of this information to nuclear reaction networks that simulate nucleosynthesis, and the interpretation of results that emerge.)

Among other results, the 2002 study [10] indicated a strong dependence of the final abundances of heavier isotopes such as ^{30}Si, ^{32,33,34}S and isotopes of P, Cl and Ar on the $^{30}\mathrm{P}(\mathrm{p},\gamma)^{31}\mathrm{S}$ reaction rate. For example, the predicted ^{30}Si and S abundances are found to

vary by factors $\leq$100 and $\leq$12, respectively, when the ^{30}P(p,γ)^{31}S reaction rate is changed up and down by a factor of 100 in the study.) The beta-decay half-life of ^{30}P ($t_{1/2}$ = 2.498 min) is considerably long on the time-scale of nova nucleosynthesis, which makes it a potential bottleneck in the nova nucleosynthesis network. Consequently, precise knowledge of this reaction rate becomes important towards understanding many astrophysical observables during the nova phenomena including, but not limited to, the identification of presolar grain origins [18], the temperature of the nova environment [19], and the degree to which accreted hydrogenic matter mixes with the white-dwarf surface [20].

1.1.2. Nova nucleosynthesis: Observable astrophysics signatures

About 10 to 15 novae are observed each year by astronomers, and about 50 are estimated to occur in our Galaxy annually [21]. Over the past several decades, we have accumulated a considerable amount of data detailing the electromagnetic radiation arising at the site of nova outbursts. Characteristic γ-ray signatures at particular energies arising from particular nuclear reactions have been proposed, but their detection has proven to be difficult due to the γ-ray flash reaching the earth before the visible signature [14]. ONe novae are also thought to contribute a fraction of the 1.809-MeV galactic γ-ray background caused by galactic nucleosynthesis of ^{26}Al.

Outside of these precise γ-ray signatures, observed nova spectra have not been easy to interpret self-consistently. The present results show large variability in predicted elemental abundances within ejecta, depending on the assumptions made by the photoionization codes performing the analysis. The estimation of ejected mass in a particular nova explosion also suffers from the same sources of uncertainty. Were these disagreements to be resolved in the future, Optical/UV/IR spectra would allow us to differentiate between the concentration of elements of different Z values — though not conclusions about mechanisms at the isotopic level. Careful analysis of optical spectra for elemental signatures has nevertheless been proposed as a useful tool towards constraining physical properties of ONe nucleosynthesis

sites, provided we could identify such sites by other means (see later discussion in 1.1.2). The difficulties involved in gleaning isotopic information for nuclear matter at the site of the outburst – from only looking at γ-ray spectra and/or other electromagnetic signatures – force us to look for additional astronomical observables that are sensitive to isotopic abundance information. In this context, the observation of anomalous isotopic abundances in meteoritic grains and the questions surrounding their paternity has garnered considerable interest in nuclear astrophysics.

^{30}Si : Marker for novae stardust

The presence of abundance ratios that disagree with the solar/cosmic abundance pattern (CAP) has been detected within multiple meteoritic grain samples that have fallen to the earth. Significant deviations from the average solar abundance pattern in these grains is a useful indicator of their possible origin outside of the solar system, and aid in their classification [22]. Presently, a subclass of these grains are thought to have originated from novae that pre-date the solar system. It is postulated that these grains survived spallation, cosmic-ray activity, and the energetic formation of the solar system by having been in a solid state, preserving their oldest abundances deep within the crystal structure. Since the measurements of abundances in meteoritic stardust can be performed with better precision than astronomical measurements, it is useful to test improved nova model calculations against their utility in classifying stardust, in addition to their ability to accurately capture features in nova luminosity profiles.

In one of the first thorough studies performed on grain formation in classical novae, Clayton and Hoyle [23] in 1976 used a model for nova optical and infrared light-curves to predict large overproduction factors for ^{13}C, ^{14}C, ^{18}O, ^{22}Na, ^{26}Al and ^{30}Si relative to solar abundances, as characteristics of stardust with nova origins.

While the principal nova signature used to be only the lower-than-solar ^{20}Ne/^{22}Ne abundance ratio (which indicates excesses in ^{22}Na), the first successful analysis [24] of SiC and

graphite grains from the Murchison and Acfer 094 meteorites found additional signatures of low $^{12}C/^{13}C$ ratios, low $^{14}N/^{15}N$ ratios, ^{30}Si excesses and large $^{26}Al/^{27}Al$ ratios in a few meteorite samples. The findings in [24] were arrived at in comparison to the best available 1D hydrodynamic models at the time, and these grains were proposed as candidates for ONe novae origin. However, these abundances agreed with those predicted by nova models only when up to 95% dilution with close-to-solar abundance materials was considered prior to grain formation in the models [24]. This assignment was debated in 2005 [25] because of the measurement of ^{44}Ca enrichment — which points to an initial presence of ^{44}Ti, an isotope exclusively synthesized in Type II supernovae.

As illustrated by the case discussed above, a well-identified set of nova grain candidates - the abundances of which match with predictions from models when treated over multiple isotopic ratios - is an active area of research. It thus becomes important to have a larger number of characteristic isotopic ratios simultaneously measured in samples and used as tracers, in order to be able to differentiate between nova stardust and stardust having other stellar origins. In addition to the ones mentioned above, isotopic ratios of $^{32}S/^{34}S$, $^{32}S/^{33}S$ and $^{29}Si/^{30}Si$ have been discussed as potential candidates that could unambiguously differentiate between grains with solar origin and those with their origin in ONe novae [26, 27, 22]. Figure 1.3, reprinted from [22], plots the $^{29,30}Si$ abundance ratios observed in several presolar Si_3N_4 and SiC meteorite grains. The data is divided into subgroups based on the Si, C and N isotopic ratios present in the grains. The publication reports that 90% of grains belong to the 'mainstream' group that has a slope of 1.3. To the left of this graph is a Scanning-Electron micrograph of a presolar SiC grain, reprinted from the same publication.

Since the assignment/rejection of ONe nova paternity to candidate meteoritic grains depends on the poorly understood $^{30}P(p,\gamma)^{31}S$ reaction rate informing ^{30}Si abundances among others, a precise determination of this reaction rate is necessary. If we experimentally determine higher reaction rates than currently assumed for this reaction, it would serve to lower the concentration of ^{30}P available at the waiting point to β^+ decay to ^{30}Si, instead contribut-

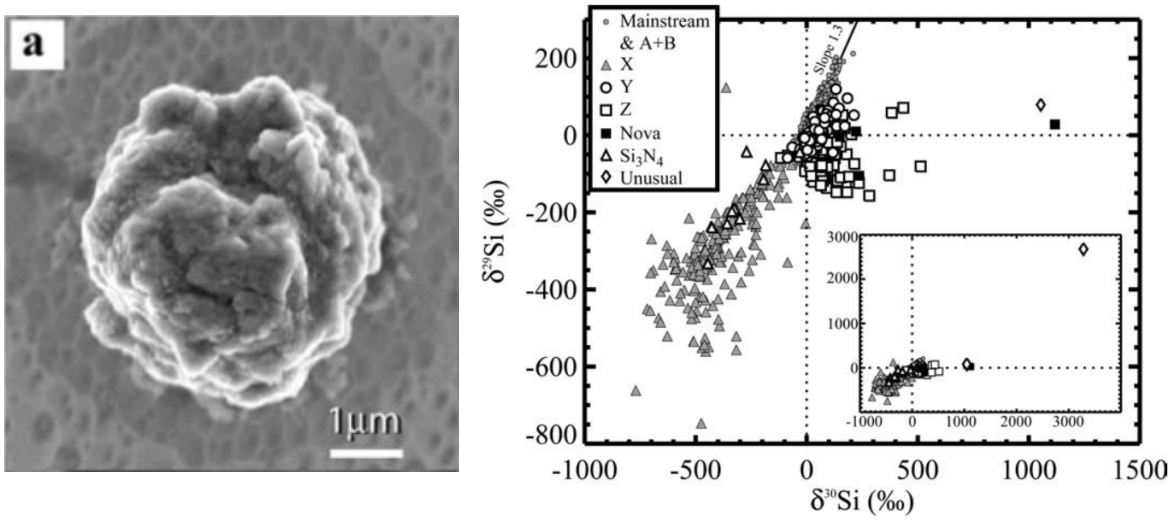

Figure 1.3. (Left) Scanning electron (SE) micrograph of a 3-μm presolar SiC grain, reprinted from [22]. (Right) Silicon isotopic ratios found in several such presolar grains expressed as delta values, defined as $\delta^i\mathrm{Si} = 10^3 \times [(^i\mathrm{Si}/^{28}\mathrm{Si})_{grain}/(^i\mathrm{Si}/^{28}\mathrm{Si})_{Sun} - 1]$. The symbols used classify the grains on the combined basis of C, N and Si isotopic ratios they carry, with 90% of them falling into the mainstream group.

ing more to the nucleosynthesis of heavier nuclei such as ^{32,33,34}S. A pictorial representation of the nuclear reaction network in the relevant section of the chart of nuclides is shown in Figure 1.4.

$^{30}\mathrm{P}(\mathrm{p},\gamma)^{31}\mathrm{S}$ reaction rate: Elemental abundance ratios as nova thermometers

In addition to the above, in a recent publication by Downen *et al.*. [19] in 2013 reaction rates adopted from the STARLIB [17] reaction-rate library were coupled with hydrodynamic information generated by the code SHIVA [28] over 4 different nova models each utilizing 45 envelope zones. Downen *et al.*. identified several elemental abundance ratios that were observed to show strong correlations with the peak temperatures attained in the simulated ONe nucleosynthesis. Some of these – namely O/S, S/Al, O/P, P/Al – had large uncertainties in these correlations, but it was observed that this uncertainty primarily arose from the currently large uncertainty in the $^{30}\mathrm{P}(\mathrm{p},\gamma)^{31}\mathrm{S}$ reaction rate. An improvement in our estimation of this reaction rate could thus facilitate the use of observed spectral lines from

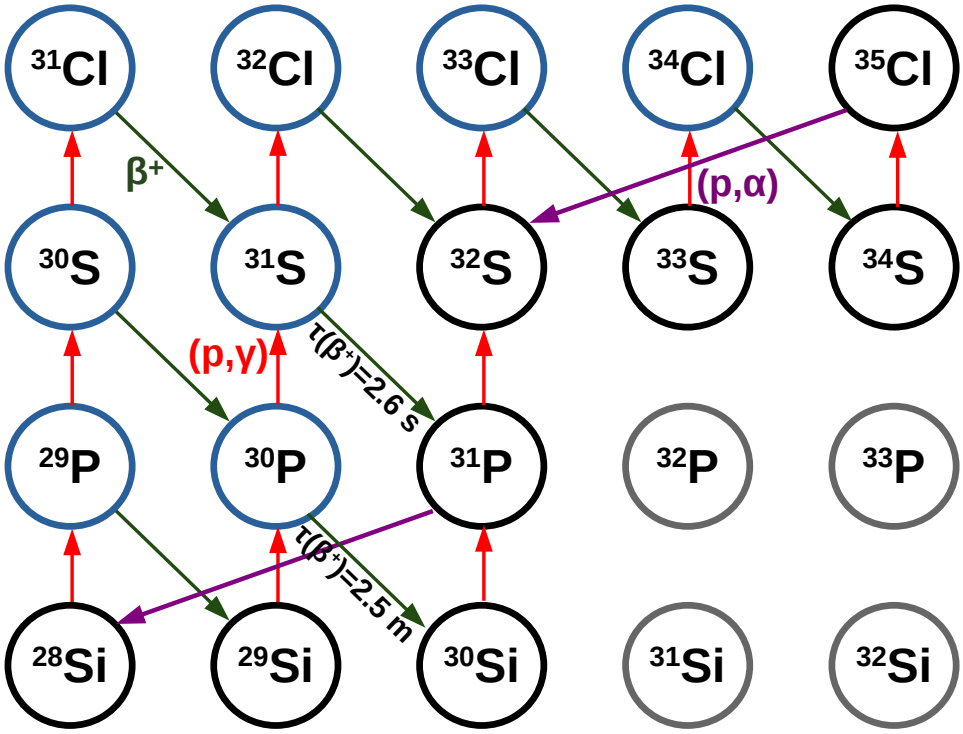

Figure 1.4. Schematic figure showing the part within the nova nucleosynthesis reaction network that contains the ^{30}P(p,γ)^{31}S waiting-point reaction. The nuclei labeled with black rings are stable, the grey/blue ones are β^-/β^+ unstable. The red, violet and green arrows represent proton capture, (p,α), and β^+ decays respectively. The ^{30}P(p,γ)^{31}S reaction acts as a waiting point in the synthesis of the isotopes ^{30}Si, ^{31}P, and ^{32,33,34}S.

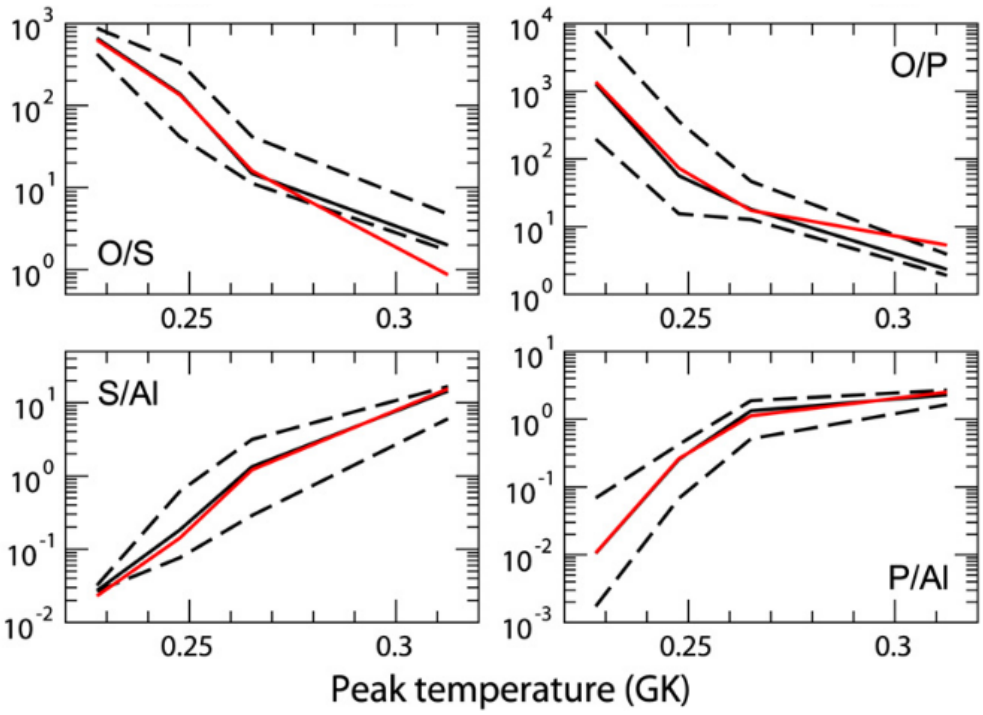

Figure 1.5. Plot reprinted from [19] — the solid lines show simulated ratios of final abundances O/S, S/Al, O/P and P/Al as a function of peak simulation temperatures attained in ONe nova nucleosynthesis. The uncertainties in all four cases - indicated by the dashed lines - are dominated by the uncertainty in the $^{30}\mathrm{P}(\mathrm{p},\gamma)^{31}\mathrm{S}$ reaction rate.

O, S, P, and Al isotopes in ONe nova spectra to estimate the temperature of the burning environment. Figure 1.5, reprinted from [19], shows the dependence of the aforementioned elemental abundance ratios to the peak temperatures attained in this study.

The following subsection describes the basic connection between laboratory measurements and the reaction rate of interest, before moving on to review our current understanding of the $^{30}\mathrm{P}(\mathrm{p},\gamma)^{31}\mathrm{S}$ reaction by highlighting a few recent measurements. In subsequent chapters, we discuss our laboratory setup that improved upon these measurements, e.g. [29].

1.2. Indirect Determination of Reaction Rates

1.2.1. Experimental challenges

In order to make cross-section measurements of a reaction such as ^{30}P(p,γ)^{31}S, it is not possible to use the direct approach of letting a proton beam impinge on a ^{30}P target followed by the detection of gamma rays as the short half-life of ^{30}P ($t_{1/2}$ = 2.498 min) makes it impractical to synthesize targets that last long enough to perform such measurements.

Alternatively, one could perform a direct measurement in inverse kinematics, with a radioactive ion beam of ^{30}P impinging on a hydrogen target, as has been done in some cases using recoil separators [30]. When using this approach, the ability to develop high-intensity radioactive ion beams 'in-situ' provides a suitable way around having to use short-lived targets for unstable nuclei. Although the method is well suited to study reactions on short-lived heavy nuclei, the development of radioactive beams with good intensity has proved challenging, resulting in an inability to provide sufficient statistics in a reasonable amount of time. Many proton-capture cross sections are quite low at the astrophysically relevant energy scales, which makes it necessary to have a high beam intensity to collect data at a satisfactory rate during an experiment. Developing radioactive ion beams with sufficient intensities is an active area of research that still needs improvement to meet the required intensities on the order of $\geq 10^{10}$ particles per second and above needed for reactions such as ^{30}P(p,γ)^{31}S. As with many other active areas of research within nuclear astrophysics, the Facility of Rare Isotope Beams (FRIB) [31] at Michigan State University is expected to play an important role towards these measurements, where newly developed experimental facilities such as SECAR [32] aim to make these direct measurements, once their operations go into full swing.

A common workaround to both the roadblocks discussed above is to use a different reaction (e.g. a transfer reaction), where the beam and target are chosen such that the net effect of the reaction is the creation of resonances in the desired heavy nucleus, such as ^{31}S,

within the relevant energy range. This approach also allows us to utilize stable nuclei and high-intensity beams to populate states in nuclei off of the valley of stability. The freedom to use projectiles with larger atomic numbers Z also allows us to attain projectile kinetic energies larger than a proton beam in an accelerator, which could help design experiments that more easily overcome the repulsion between the projectile and target due to the Coulomb barrier. A carefully designed transfer reaction could thus permit us to prepare short-lived ^{31}S excited states 'in-situ' and detect their proton (and potentially γ-ray) decays to constrain the $^{30}\mathrm{P}(p,\gamma)^{31}\mathrm{S}$ reaction rate. As we shall see, the approach presented in this document attempts to avoid potential difficulties of direct measurements by using a stable beam and a stable target in a transfer reaction.

1.2.2. Reaction rates: A simple mathematical model

In order to better discuss nuclear reactions that happen during nova explosions, we must first recognize that the majority of reactions that drive nucleosynthesis in these environments involve the interaction of charged, quantum-mechanical particles - typically protons and heavy nuclei. The total interaction between these particles is dominated by strong nuclear interactions and Coulomb interactions at the energy scale kT characteristic of their thermal motion, where T is the temperature of the stellar medium and k is the Boltzmann constant. Particles interacting at a given temperature can be assumed to have their energy population distributed in a Maxwell-Boltzmann (MB) distribution which assumes the probability of particles moving with kinetic energy E is proportional to $Ee^{-E/kT}$ [2]. This distribution peaks at $E = kT \sim 35$ keV when $T \sim 0.4$ GK. Were the interacting nuclei strictly classical particles separated by a distance 'r' having their radii at nuclear length-scales ($\sim$fm), they would need to overcome the repulsive Coulomb interaction between them, which has a potential of the form

$$V_C = \frac{Z_1 Z_2 e^2}{r} \tag{1.1}$$

which is as high as 4 MeV for the ^{30}P+p system (assuming nuclear radii $r = r_0 A^{1/3}$ with $r_0 = 1.25$ fm). Here 'e' is the elementary charge, and Z_1 and Z_2 are the atomic numbers of the interacting nuclei. This would imply a very insignificant probability for the reaction to proceed via the tail of the Maxwell-Boltzmann distribution (Probability $\sim e^{-E/kT} \sim e^{-V_C/kT} \sim 10^{-51}$). As we shall see, the ability of quantum-mechanical particles to tunnel through such potential barriers increases the odds for the interaction considerably, facilitating stellar nucleosynthesis.

When one treats the problem quantum mechanically, one can simplify the problem to ignore the many-body correlations between constituents of the nuclei (individual protons and neutrons), and treat the system as made up of only two particles (in our case, a proton and a ^{30}P nucleus, we assume the participants are *not* identical here on out) interacting via a single intermediary potential. A typical landscape of this approximate interaction potential is shown in Fig. 1.6, as a function of the separation 'r' between the particle centers. This model is commonly referred to as the Woods-Saxon potential for a single-particle interaction [2]. The characteristic length-scales for the nuclear interaction sets the nuclear boundary where the potential changes sign and becomes attractive, while the $1/r$ nature of the Coulomb repulsive interaction dominates more and more as their separation increases. We thus expect the two positively charged particles to experience Coulomb repulsion at large separations 'r'. However, at high enough temperatures that are attained in nova environments, the relative nuclear motion in the stellar medium picks up kinetic energies large enough to permit quantum-mechanical tunnelling of the proton into the heavy nucleus with sufficient probability. As a result of this process, the protons are captured into the heavy nucleus to form resonant states in ^{31}S that can undergo γ decays, proton decays, or decays via another particle channel if energetically allowed.

If we were to assume a classical turning point R_C for the interacting particles at the MB peak, and a nuclear radius R_n, the probability P that the particle penetrates the barrier

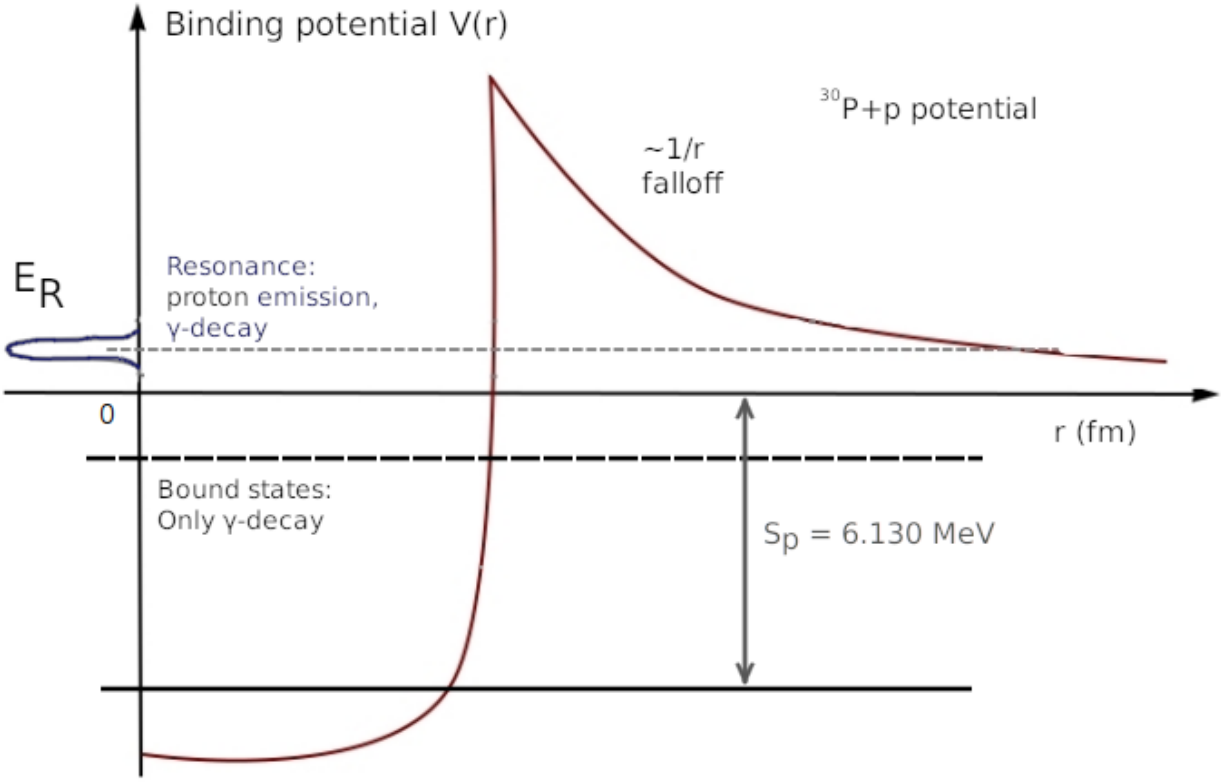

Figure 1.6. Sketch of the typical potential landscape that exists between a pair of charged particles such as proton (p) and ^{30}P, as a function of r, their radial separation. At long range, the potential is dominated by Coulomb repulsion which falls off as $1/r$. At smaller r, the potential is attractive, and supports bound states that correspond to states in ^{31}S, the combined nucleus.

The combined quantum-mechanical system typically has two types of states: 1) bound states that possess $V < 0$, from which only decays via γ-ray emission are permitted to states of lower excitation energy, and 2) resonant states, from which both γ-ray decays and tunnelling charged-particle decays (in our case, proton decays) are allowed, each with its own lifetime. Every lifetime τ corresponds to a notional 'width' Γ of the state in units of energy with $\Gamma \approx \hbar/\tau$. The proton-decay lifetimes (widths) broadly decrease (increase) as we go up in excitation energy, since the Coulomb barrier becomes thinner and thinner. The proton-separation energy S_p is also indicated.

(also called Penetrability) can be expressed as

$$P = \frac{|\psi(R_n)|^2}{|\psi(R_C)|^2} \tag{1.2}$$

Since the quantum-mechanical wavefunction ψ is finite and non-zero at $r = R_n$, we have a non-zero tunnelling probability. The exact expression for P in the case of the Woods-Saxon potential was originally derived by Bethe [33], which is recreated in [2]. At $R_C << R_n$ [2], it can be shown that P can be approximated by the simpler expression

$$P = exp(-2\pi\eta) \tag{1.3}$$

where

$$\eta = \frac{Z_1 Z_2 e^2}{\hbar v} \tag{1.4}$$

with e being elemental charge, $\hbar$ Planck's constant, v, the relative velocity of interaction in the center of mass frame, and Z_1, Z_2 the atomic numbers.

Since the nuclear reaction cross-section for proton capture is expected to be proportional to the 'penetrability' P and the characteristic 'cross-section' σ of a particle in an MB distribution by virtue of its de-Broglie wavelength λ ($\sigma \propto \pi\lambda^2 \propto \frac{1}{E}$ can be shown, assuming an ensemble of free particles),

$$\sigma(E) = e^{-2\pi\eta}\frac{1}{E}S(E) \tag{1.5}$$

where $S(E)$ represents the astrophysical S-factor, that encapsulates all the corrections that arise due to nuclear effects beyond what is captured in our simple model. Typically, contributions to the S-factor arise from the presence of resonant states that lie close to the proton threshold, that serve to boost/suppress the cross-section in the region around selected energies.

All of the above discusses the problem on the basis of a single nucleus. We now expand it to include the entire stellar system, and explicitly incorporate the Maxwell-Boltzmann distribution. Assuming that there are N_1, N_2 particles per volume of the heavy and light reactants respecively, the total cross-section that is seen by the light nuclei in unit volume is $N_1\sigma(v)$, where we have expressed the cross-section above as a function of the relative velocity v. With N_2 light nuclei moving at the same relative velocity v distributed in the MB distribution, the total flux of light nuclei is seen as J = $N_2 v$. Combining the two, we have the reaction rate H

$$H = N_1 N_2 v \sigma(v) \tag{1.6}$$

Now, we know that v is distributed in a Maxwell-Boltzmann distribution $\phi(v)$, which in 3 dimensions takes the form

$$\phi(v) = 4\pi v^2 \left(\frac{\mu}{2\pi kT}\right)^{3/2} e^{-\frac{\mu v^2}{2kT}} \tag{1.7}$$

where μ is the reduced mass in the COM frame, $\mu = \frac{m_1 m_2}{m_1 + m_2}$, in amu.

Now, we estimate the ensemble average of the reaction rate H above, by performing

$$< H >=< \sigma v >= \int_0^\infty \phi(v) H(v) dv = N_1 N_2 \int_0^\infty 4\pi v^3 \sigma(v) \left(\frac{\mu}{2\pi kT}\right)^{3/2} e^{-\frac{\mu v^2}{2kT}} dv \tag{1.8}$$

Performing a coordinate transformation to energy units using $E = \frac{\mu v^2}{2}$, we obtain

$$< \sigma v >= \left(\frac{8}{\pi\mu}\right)^{\frac{1}{2}} \frac{1}{(kT)^{3/2}} \int_0^\infty E\sigma(E) e^{-\frac{E}{kT}} dE \tag{1.9}$$

Using our prior form for σ as given in equation 1.5, we can write this as

$$< \sigma v >= \left(\frac{8}{\pi\mu}\right)^{\frac{1}{2}} \frac{1}{(kT)^{3/2}} \int_0^\infty S(E) exp\left(-\frac{E}{kT} - \frac{b}{E^{1/2}}\right) dE \tag{1.10}$$

with $b = \frac{(2\mu)^{1/2}\pi e^2 Z_1 Z_2}{\hbar}$ where the exponential expression is known as the the Gamow peak depicted in Fig. 1.7. The Gamow peak illustrates how quantum-mechanical tunnelling couples with the Maxwell-Boltzmann distribution of particle energies, to provide a region around a characteristic energy (also called the Gamow Energy) $E_G = b^2$ where the reaction has a higher probability of proceeding than it would have had in a purely classical case. If S(E) is assumed to be independent of E, the integrand in Eq 1.10 can be maximized in E via differentiation to give the energy E_0 at which the reaction rate becomes maximum as:

$$E_0 = \left(\frac{bkT}{2}\right)^{2/3} = 0.1220(\mu Z_1^2 Z_2^2 T_9^2)^{1/3}\text{MeV} \tag{1.11}$$

Now, the above analysis for E_0 reflects the case when there are no resonances present in the Gamow window. The evaluated reaction rate in this case is commonly referred to as caused by 'direct' or 'non-resonant' radiative capture, since it does not have a contribution from the nuclear interaction via the S-factor. In case there are additional resonances in the region, S(E) will reflect their structure, and modify the results. If we assume the resonances are narrow and isolated, each of them can be represented by the Breit-Wigner formula as:

$$\sigma(E) = \frac{\lambda^2}{4\pi}\omega\frac{\Gamma_x\Gamma_y}{(E - E_r)^2 + (\Gamma/2)^2} \tag{1.12}$$

where the factor ω takes into account the spin degeneracy of the states, $\omega = \frac{(2J_r+1)}{(2J_A+1)(2J_B+1)}$ where $J_{A,B}$ are the spins of the reactant nuclei, and J_r is the spin of the resonance. $\Gamma_{x,y}$ represent the widths of the two decay modes of the resonance in question, which, in the case of (p,γ), would be Γ_p and Γ_γ, and Γ is the total width that includes the sum of Γ_x, Γ_y and widths of any other decay channels that may be energetically allowed. In the context of

the present measurement, $\Gamma = \Gamma_x + \Gamma_y = \Gamma_p + \Gamma_\gamma$ since these are the only decay channels available to the ^{31}S states under investigation.

Inserting the above form into equation 1.9, we obtain

$$< \sigma v >= \left(\frac{8}{\pi\mu}\right)^{\frac{1}{2}} \frac{1}{(kT)^{3/2}} \int_0^\infty \frac{\lambda^2}{4\pi}\omega \frac{\Gamma_x\Gamma_y}{(E-E_r)^2 + (\Gamma/2)^2} e^{-\frac{E}{kT}} E dE \tag{1.13}$$

Following the argument in [2], if we now use the slow-varying nature of the factor $Ee^{-\frac{E}{kT}}$, and widths $\Gamma_{x,y}$ over the narrow width of the resonance, we are left with

$$< \sigma v >= \left(\frac{8}{\pi\mu}\right)^{\frac{1}{2}} \frac{1}{(kT)^{3/2}} \frac{\lambda^2}{4\pi}\omega\Gamma_x\Gamma_y e^{-\frac{E_r}{kT}} E_r \int_0^\infty \frac{1}{(E-E_r)^2 + (\Gamma/2)^2} dE \tag{1.14}$$

$$= \left(\frac{8}{\pi\mu}\right)^{\frac{1}{2}} \frac{1}{(kT)^{3/2}} \frac{\lambda^2}{2}\omega \frac{\Gamma_x\Gamma_y}{\Gamma} e^{-\frac{E_r}{kT}} E_r \tag{1.15}$$

Now, using $E_r \approx \frac{h^2}{2\mu\lambda^2}$, i.e $E_r\lambda^2 \approx \frac{(2\pi\hbar)^2}{2\mu}$

$$< \sigma v >= \left(\frac{8}{\pi}\right)^{\frac{1}{2}} \frac{1}{(\mu kT)^{3/2}} \frac{4\pi^2\hbar^2}{4}\omega \frac{\Gamma_x\Gamma_y}{\Gamma} e^{-\frac{E_r}{kT}} \tag{1.16}$$

$$= \left(\frac{2\pi}{\mu kT}\right)^{3/2} \hbar^2\omega \frac{\Gamma_x\Gamma_y}{\Gamma} e^{-\frac{E_r}{kT}} \tag{1.17}$$

$$= \left(\frac{2\pi}{\mu kT}\right)^{3/2} \hbar^2(\omega\gamma)_r exp\left(-\frac{E_r}{kT}\right) \tag{1.18}$$

where we use the definition of the resonance strength $(\omega\gamma)_r = \omega\frac{\Gamma_x\Gamma_y}{\Gamma}$ in the last step.

If there are many isolated narrow resonances in the region, the contribution due to each can just be summed over to obtain the total resonant reaction rate. The expression above is often represented in molar units as

$$N_A < \sigma v >= N_A \left(\frac{2\pi}{\mu kT}\right)^{3/2} \hbar^2 \sum_r (\omega\gamma)_r exp\left(-\frac{E_r}{kT}\right) \tag{1.19}$$

where N_A is the Avogadro number.

Knowing all isolated resonance strengths and energies ($(\omega\gamma)_r$ and E_r respectively, both

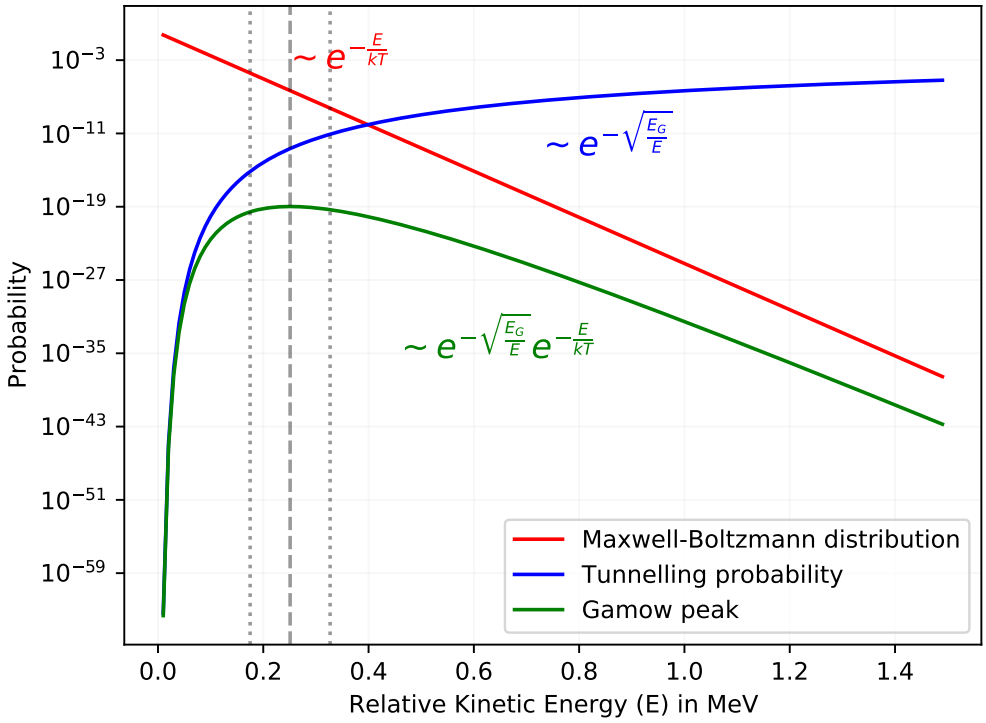

Figure 1.7. Schematic plot showing the Gamow peak for $^{30}\mathrm{P}(p,\gamma)^{31}\mathrm{S}$ in an astrophysical environment at temperature $kT = 0.2$ GK. E_G is the Gamow energy, and is related to the coulomb barrier penetrability [2] between the participants. The Gamow energy E_0 is shown in a bold vertical dashed line. The end points of the Gamow window as discussed in [2] are shown as fainter dotted vertical lines at $E = E_0 \pm \Delta/2$.

in units of MeV) in the region, the reaction rate due to all resonances at a temperature of T_9 (GK) between two initial reactants having reduced mass μ atomic mass units between them is found as [2, 10]:

$$N_A\langle\sigma v\rangle = \frac{1.5399 \times 10^{11}}{(\mu T_9)^{3/2}} \sum_r (\omega\gamma)_r e^{-11.605 E_r/T_9} \left[\frac{cm^3}{mol.s}\right] \tag{1.20}$$

Indirect determinations of reaction rates, thus require us to measure/constrain properties of narrow resonances within the Gamow window experimentally - like J_r, $\Gamma_{x,y}$ values and resonance energies E_r. Very often, one performs angular-distribution measurements to estimate spin values J_r, and either measures the particle widths directly, or tries to measure the Branching Ratio (B_x) Γ_x/Γ for one or both of the decay channels. In cases where one or both of the partial widths is not measured, theoretical estimates must be relied on. For Γ_γ widths, these are found using γ-decay lifetime data, or theoretical estimates such as those using the Weisskopf method. For a theoretical determination of the charged particle width, one utilizes estimates Γ_{sp} of the state's width using suitable evaluations of the nuclear potential. The real charged-particle width Γ_p is related to this theoretical estimate as $\Gamma_p = C^2S\ \Gamma_{sp}$ [34] where C is the Clebsch-Gordon coefficient, and S is the spectroscopic factor, which can be determined from states in the mirror nuclei, or measured experimentally. It should be noted that disagreements with estimated single-particle calculations are observed in experiment from time to time, which point to the limitations of the simplifying assumptions we make in this analysis. Direct reaction rate measurements, and better theoretical estimates that include collective/many-body effects are hence an active and fruitful area of research that has the power to help inform in detail the process of stellar nucleosynthesis in particular, and nuclear astrophysics phenomena in general. In the absence of better informed estimates, indirect measurements using the single-particle treatment have served as a useful starting point.

Surveys of recent experimental results that attempt to determine the level structure of

^{31}S within the Gamow window for ^{30}P(p,γ)^{31}S consist of a wide variety of measurements that largely utilize the single-particle approximation that assumes narrow, isolated resonances. The prolific and continued interest in the properties of this nucleus is a testament to the importance of this hitherto elusive reaction rate. The next section briefly reviews a few of the recent experiments that studied the level structure of ^{31}S within the energy region of interest.

1.3. Prior Studies of ^{31}S Resonances Near Proton Threshold

Until around 2004, astrophysicists largely relied on the theoretical Hausner-Feshbach model to estimate the ^{30}P(p,γ)^{31}S reaction rate. This estimate does not take into account real individual resonances in the energy region of interest - instead choosing to estimate the statistically expected density of states in the region [35]. However, the assumption of a high-enough density of states to warrant this approach is expected to be less accurate for nuclei with smaller masses, and those that are close to shell closures and drip lines. This makes the experimental investigation of narrow resonances in this region necessary. Nuclear physics evaluations combining the many varied measurements of ^{31}S level structure have been performed several times in the past - including in 1978 [36], 1990 [37], 1998 [38], 2013 [39], and 2022 [40]. These evaluations have currently identified the position of thirteen resonances of interest in the region $E_x = 6.130 - 6.7$ MeV, and firmly determined the proton-separation energy in ^{31}S at 6.13065(24) MeV.

The measurements reported in these evaluations have used several experimental techniques, of which a sailent few – most relevant to levels in the Gamow window – are discussed further. The interested reader is referred to the latest evaluation [40] for details, and to the review at reference [35] for a discussion focused on measurements predating 2014. Several of the measurements in the literature employed transfer/charge-exchange reactions such as ^{32}S(p,d)^{31}S [41, 42], ^{32}S(d,t)^{31}S [29, 43], ^{32}S(^{3}He,α)^{31}S [44], ^{33}S(p,t)^{31}S [45] and ^{31}P(^{3}He,t)^{31}S [35, 46, 47, 40]. Many of the studies prior to the mid-2000s were originally motivated by

interests in the nuclear structure of ^{31}S, including the estimation of single-particle spectroscopic factors, and mirror-level assignments between ^{31}S and ^{31}P. They still served as a reference point that helped inform the more astrophysics-focused experimental campaigns that began in earnest in the early years of the 21st century and offered initial estimates to the spectrscopic properties of several of these states by mapping them to their mirror states in ^{31}P.

Most of these transfer-reaction measurements detected charged particles utilizing a magnetic spectrograph or a scattering chamber as a precision spectrometer. Many of these studies measured angular distributions of the reaction ejectiles to ascertain spectroscopic properties of ^{31}S levels using the Distorted-Wave Born Approximation, or in more recent cases, more detailed analyses using tools like FRESCO that rely on the coupled-channels formalism [48]. An important subset among these measurements complemented the high-resolution measurements of ^{31}S spectra, with the detection of decay protons and/or coincident γ-ray emissions. The experiment described in this thesis follows this approach closely, where decay protons, but no γ rays, were detected in coincidence with momentum-analyzed tritons corresponding to states in ^{31}S populated by the (^{6}Li,t) transfer reaction. These coincident charged-particle measurements offer spectroscopic information and branching-ratio measurements of states in ^{31}S above the proton threshold. Of particular importance among these, is Wrede *et al.*'s 2009 ^{31}P(^{3}He,t)^{31}S*(p)^{30}P measurement [29], which determined proton-branching ratios of states down to $E_x = 6.720$ MeV, just outside the Gamow window, and provided constraints to several of the states' spin-parity information. Two other important measurements, Parikh [^{31}P(^{3}He,t)^{31}S] [46] and Irvine [^{32}S(d,t)^{31}S] [43], used QQQD spectrographs to offer measurements with the best resolution of the excitation energies in the region of interest – with reported precision below 2 keV – in addition to angular distributions for their spectroscopic properties. The only other measurements that have offered better precision involved γ-ray detection, to be discussed later. A promising new technique that has gathered much recent interest, detects both decay protons and γ rays simultaneously. Very recent work at

Texas A&M University by Burcher *et al.* [49] reports a proof-of-concept for this approach using the Hyperion array [50] to measure ^{32}S(p,d)^{31}S*(pγ). This measurement reported proton-branching ratios down to $E_x = 6.87$ MeV, with good agreement with those measured by Wrede *et al.* [29]. Future upgrades to the experimental setup are expected to provide proton-branching ratio information for ^{31}S states within the Gamow window, and constrain their spectroscopic properties and γ widths.

Parallel to the many charged-particle detections discussed above, there has also been a steady pursuit of utilizing γ-ray and neutron based measurements to ascertain the spectroscopic properties of ^{31}S states. Many of these studies utilize various fusion-evaporation reactions, including ^{12}C(^{20}Ne,nγ)^{31}S, ^{16}O(^{16}O,nγ)^{31}S [51, 52, 53, 54], ^{24}Mg(^{12}C,αnγ)^{31}S [55], ^{24}Mg(^{16}O,n$\alpha\alpha\gamma$)^{31}S [56], and ^{28}Si(α,nγ)^{31}S [40]. In addition to these, there are also transfer reactions that involve the detection of neutrons and γ rays such as ^{2}H(^{30}P,^{31}S)nγ [51], ^{29}Si(^{3}He,nγ)^{31}S and ^{29}Si(^{3}He,n)^{31}S [57]. These measurements, many of them originally aimed at investigating the nuclear structure of ^{31}S, measured γ-ray cascades using High-Purity Germanium (HPGe) arrays to make precision measurements of excitation energies corresponding to several unknown levels in ^{31}S. All of them involve the fusion of heavy nuclei followed by selective gating on the lighter fragments evaporated from the system, to identify only those that arise from ^{31}S levels being populated. Of particular importance is the Gammasphere measurement of ^{28}Si(α,nγ)^{31}S [58]. This measurement reported 10 levels in the region of interest, determined the excitation energies to very high precision of all the ^{31}S states under 6.7 MeV, matched all of them to their analogs in ^{31}P, and used the angular distribution of detected γ rays to make unambiguous spin-parity assignments for them. Unlike many of the prior fusion-evaporation measurements that selectively populated high-spin resonances, this experiment demonstrated the ability to also populate low-spin resonances in the region of interest [35]. The advantage to fusion-evaporation techniques lies in the ability to simultaneously measure properties of states in mirror nuclei, such as ^{31}S and ^{31}P. The ^{28}Si(α,nγ)^{31}S measurement in particular is a very good illustration of the power of combining shell-model

calculations, mirror symmetry, and γ-ray measurements towards filling gaps in our knowledge of nuclear levels, and applying them to shine light on astrophysically important problems. Lastly, a third family of measurements involves the use of a complicated transfer reaction followed by mass separation to generate a steady beam of β^+-unstable ^{31}Cl, the decay of which creates ^{31}S in several excited states with high selectivity. Coincident detection of the decayed β^+ along with the decayed protons and/or γ rays from states in ^{31}S above the proton-threshold (beta-delayed particle/γ-ray detection), allows the determination of proton and/or γ partial widths. In an early measurement using this technique [59], ^{31}Cl nuclei were created by the ^{32}S$(p, 2n)$ fusion evaporation reaction, which was then implanted into a Carbon foil. The β^+ particles arising from decays are detected in coincidence with protons and γ rays emitted by ^{31}S resonances arising from the β^+ decay. Charged particles were detected by double-sided silicon strip detectors, and γ rays by High-Purity Germanium detectors. Having both these detections performed in coincidence allows for simultaneous estimation of γ-ray and proton-branching ratios, and reconstruction of level schemes. This measurement reported one state in the region of interest, and served as a proof-of-concept towards the utility of β^+-delayed measurements toward spectroscopy of states in this region. Further studies that utilized similar methods were undertaken at the National Superconducting Cyclotron Laboratory synthesizing a ^{31}Cl beam using a fragment separator analyzing resultant products from a ^{36}Ar$(^9Be, X)$ fusion evaporation [60, 61, 62]. A plastic scintillator was used to record the β-decay trigger, followed by the detection of γ-ray cascades in the Clovershare array of HPGe detectors to measure γ-ray transitions up to a ^{31}S excitation energy of 6390 keV. This left the proton-branching ratios from these resonances unknown, but suggested the 6.390 MeV state assigned as $J^\pi = 3/2^+$ may significantly contribute to the ^{30}P(p,γ) reaction rate. Very recently in 2022, there was an exciting new study [63, 64] conducted at NSCL using the newly developed GADGET detector. GADGET stands for Gaseous Detector with Germanium Tagging, which combined a gaseous proton detector with a Micromegas readout with the SeGA high-purity Germanium array. β-delayed protons from the important

J^{π} =3/2^{+}, 6.390 MeV state were detected for the first time in this experiment, offering the first experimental observation of proton branching from states in the region. It was also confirmed, by virtue of the γ-ray tagging capabilities of the apparatus, that the proton emission from this state was to the ground state in ^{30}P, since there were no coincident γ-ray peaks observed. Thus, β-delayed particle/γ detection forms yet another active area of research towards experimental evaluation of the ^{30}P(p,γ)^{31}S reaction rate.

In this study, we synthesized ^{31}S excited states using a $(^{6}\mathrm{Li}, t)$ transfer reaction on a stable $^{28}SiO_2$ target. This particular transfer reaction was chosen for the ease of availability of a suitable target, and of the potential to use the SNICS (Source of Negative Ions by Cesium Sputtering) source at FSU's John D Fox Laboratory, which was capable of delivering sufficiently large beam currents. There had also not been any previous experimental study performed of this nucleus using this reaction mechanism, which offered the possibility of selectivity to states different from those seen in other measurements. A QQQD-spectrograph measurement conducted in 1978 by Woods *et al.* [66] had reported cross-sections comparable to those in (^{3}He,t) charge-exchange reactions ($\sim$ 10 μb/sr) for (^{6}Li,t) transfer reactions. This information, along with the available beam intensity from the SNICS source at FSU indicated the viability of this measurement towards recording sufficiently large statistics within the Gamow window. Table 1.1 lists ^{31}S states with known properties in the Gamow window prior to the current measurement, cited from the latest nuclear data evaluation [40]. The single-particle Wigner limit assuming the formalism in [65] is reported for all states, which provides a theoretical estimate of the maximum proton width in each case. In addition, proton-branching ratios are reported for states where they have been successfully measured.

During the experiment, the SNICS source provided around 100 enA of $^{6}\mathrm{Li}^{3+}$ beam on target for over 96 hours of runtime. The tritons associated with the populated ^{31}S states were momentum analysed by the Super Enge Split-pole Spectrograph. The resultant ^{31}S excited states were further analyzed for proton emissions coincident to the detection of momentum-analyzed tritons, which allowed direct measurement of the states' proton-branching ratios.

Table 1.1. Properties of ^{31}S states within the Gamow window associated with ONe nova nucleosynthesis, cited from the latest evaluation [40]. Excitation energies, adopted spin-parity information, and known proton-branching ratio are included. For states with unknown proton-branching ratios, the final column evaluates single-particle wigner limits assuming L=0, $C^2S = 1$, following the approach described by ref [65].

Excitation Energy in ^{31}S (MeV)	J^π	Branching ratio (Γ_p/Γ)	Single-particle Wigner limit (keV)
6138.3(6)	(7/2+)		2.E-65
6157.7(3)	(5/2,7/2)		2E-31
6255.1(3)	1/2+		7.E-11
6279.10(13)	3/2+		2.E-09
6326.8(5)	(3/2)		3.E-07
6357.06(22)	(5/2-)		3.E-06
6375.6(3)	9/2-		1.E-05
6390.46(16)	3/2+	0.025% $^{4}_{-3}$[63]	2.E-05
6392.16(22)	(5/2+)		2.E-05
6392.93(20)	11/2(+)		3.E-05
6402(2)	(7/2-)		4.E-05
6541.6(4)	3/2(-)		0.0074
6582.4(20)	(5/2-,7/2-)		0.021
6634.64(23)	9/2(-)		0.063
6720(1)	5/2	25% $^{7}_{-20}$[29]	0.28
6749(2)	3/2+	57% $^{7}_{-32}$[29]	0.44
6796(25)			0.83
6832.7(3)	11/2(-)		1.30

The subsequent chapter shall describe in more detail, the experimental setup utilized towards the current measurement.

Chapter 2. .Instrumentation

The ^{28}Si(^{6}Li,t)^{31}S$^{*}(p)^{30}$P reaction was studied at Florida State University (FSU)'s John D. Fox Superconducting Accelerator Laboratory using the Super Enge Split-Pole Spectrograph (SE-SPS) which was originally located at the Wright Nuclear Structure Laboratory (WNSL) at Yale University. Following the closure of the WNSL in 2011, the setup was transported to FSU in 2013 and reassembled with a few upgrades in the subsequent years. A simplified schematic of the original design's operation is shown in Fig. 2.1. The typical measurements made with the SE-SPS are performed in regular kinematics, with a light beam impinging on a heavy target. At suitable energy scales, we expect multiparticle transfers to occur between the beam nuclei and the target nuclei, to produce one light and one heavy reaction product. For a review of the utility and range of transfer reactions used to study nuclear astrophysics phenomena, the interested reader is directed to this 2016 review [34].

The light products carry the bulk of the momentum forward, and move into the SE-SPS where they are momentum analyzed by the magnetic fields and focused onto a detector placed along the focal plane (the focal plane detector, hereafter). The position of the light particles detected at the focal plane can be calibrated to a high degree of precision to the momentum of the detected particle. In turn, this allows us to use energy conservation to determine the excitation energy of the heavy product synthesized, that is stopped in the target due to the low momentum transferred to it.

These heavy reaction products may decay via particle emission if their excitation energy is larger than the particle-emission threshold. The emitted decay particles can then be detected at backward angles by semiconductor charged-particle detectors placed in the target chamber, in time coincidence with the light reaction products detected at the focal plane. The segmented nature of the semiconductor detectors used to detect the heavy product's charged-particle decay, allows us to identify the decay particle's angular distribution with respect to the beam axis [67]. This angular distribution can be used to constrain specific spectroscopic properties (i.e. the spin, parity, and branching ratio) of the excited state of

the heavy product which undergoes the charged-particle decay.

When the SPS was moved from Yale to FSU, the detector systems were given upgrades. In particular, the silicon detector array used at Yale, YLSA (Yale Lampshade Array) was redesigned to its present form, SABRE — the Silicon Array for Branching Ratio Experiments [68]. The signal processing capabilities also received a major overhaul, moving from use of shaping amplifiers, Analog-to-Digital converters (ADCs) and Time-to-Digital converters (TDCs) to digitizer units, offering improved timing resolution and detection of lower energy particles seen by SABRE. The next few sections detail a few experimental capabilities at the FSU John D. Fox Laboratory that were used in making the reported measurement, and discuss the efforts at LSU that went into their development where relevant.

2.1. SNICS Beam Source for ^{6}Li, and the FSU Tandem van de Graaff Accelerator

As described in previous sections, the measurement at hand requires us to accelerate charged particles, specifically ^{6}Li, to kinetic energies that are large enough to cause the reaction to proceed, and for astrophysically relevant states in ^{31}S to be populated. In order to accomplish this, we utilized the FSU Tandem van de Graaff accelerator, which is shown in Fig. 2.2 along with all the other sailent elements of the beamline at the John D. Fox laboratory at FSU. (For a light review that discusses the Tandem van de Graaff and its applications in various fields, the curious reader is referred to reference [69] and citations within.) Negatively charged ^{6}Li ions are synthesized by an NEC SNICS II source (Fig. 2.2, lower right corner), which stands for National Electronics Corporation Source of Negative Ions by Cesium Sputtering. This source works by having hot, vaporized cesium metal strike a negatively-biased ^{6}Li rod that then releases ^{6}Li atoms off its surface via the eponymous sputtering process. The dramatically low electron affinity in cesium atoms causes the relatively more electronegative ^{6}Li atoms that pass through it to become negatively charged ^{6}Li^{-} ions. (SNICS II is dedicated for use with production of negative-ion beams of solid elements — to produce gaseous beams, the laboratory also has in place an RF-discharge source, which is the pink feature to the

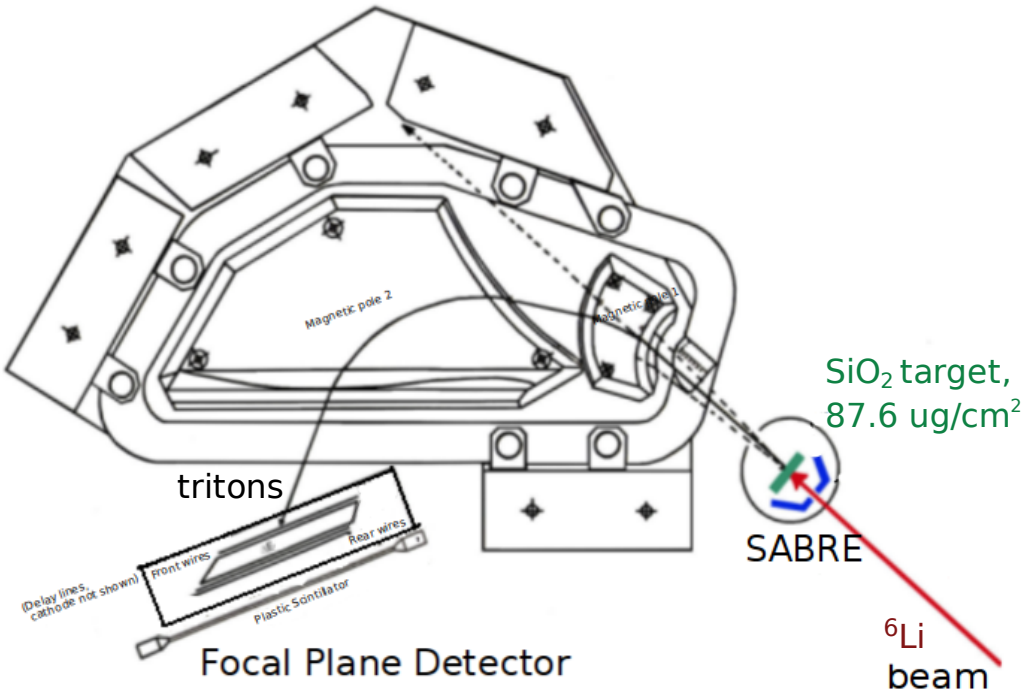

Figure 2.1. Schematic of the SE-SPS setup used to study the ^{28}Si(^{6}Li, t)^{31}S*(p)^{30}P reaction. The ^{6}Li beam (red line) accelerated by the Tandem Van de Graaff accelerator impinges on the 87.6-μg/cm^2 thick natural SiO_2 target (green), and the spectrograph selects the tritons by momentum, focusing them on the focal plane detector. The magnetic field $\vec{B}$ is fine-tuned so as to focus the tritons corresponding to the population of astrophysically relevant excited states in ^{31}S onto the focal plane. Coincident charged-particle decays of the heavy product ^{31}S get detected by SABRE (shown in blue) at backward angles from the beam, whose energies and angular distributions can then be studied to constrain their properties.

lower-right in Fig. 2.2). For further discussion of SNICS, the reader is referred to the review article at [70] and references therein.

The stream of negative $^6Li^-$ ions generated in the SNICS II source is then momentum analyzed and injected to the Super-FN Tandem van de Graaff accelerator, which can support a terminal voltage of up to +9MV. The terminal, in essence, is a large positively-charged sphere maintained at its constant high potential by a carefully designed feedback mechanism. The terminal rests inside a large tank of Sulfur Hexafluoride (SF_6) gas. SF_6 is well-known to possess a high dielectric strength [71], and a similarly large dielectric breakdown limit, which offers good protection against excessive leakage of the terminal potential through the medium. The large positive charge of the terminal accelerates the incoming $^6Li^-$ ions via the beamline into the center of the terminal, where they pass through a carbon stripper foil which completely ionizes most ions to $^6Li^{3+}$ at the energies used in this experiment. Owing to the positive charge experiencing repulsion from the terminal, these $^6Li^{3+}$ ions get accelerated once more from the terminal 'in tandem', increasing their energy. The total kinetic energy of the charged-particle beam can be calculated as $E_{beam} = eV_{tandem}(Z+1) + E_{injection}$, where $E_{injection}$ is the kinetic energy at injection, Z is the final charge-state of the beam ($Z = 3$ in our case) and V_{tandem} is the terminal potential.

The positively-charged beam is subsequently taken through several stages of beam optics that serve to keep the beam from diverging, and direct it to the desired target chamber. A high degree of stability ($<0.1\%$) in the Tandem's terminal potential (and thus, the beam energy) is achieved by using a high-resolution bending/analyzing magnet (HRBM) at its exit, and feeding back to the control system regulating the Tandem's potential an error signal derived from beam currents detected on either side of the selection slit in the HRBM. On its way to SE-SPS target chamber, the beam passes through the Superconducting Linear Accelerator (LINAC), which is unused for the present measurement. The LINAC could be used in applications that require beams with a higher kinetic energy than those capable of being provided solely by the Tandem van de Graaff accelerator.

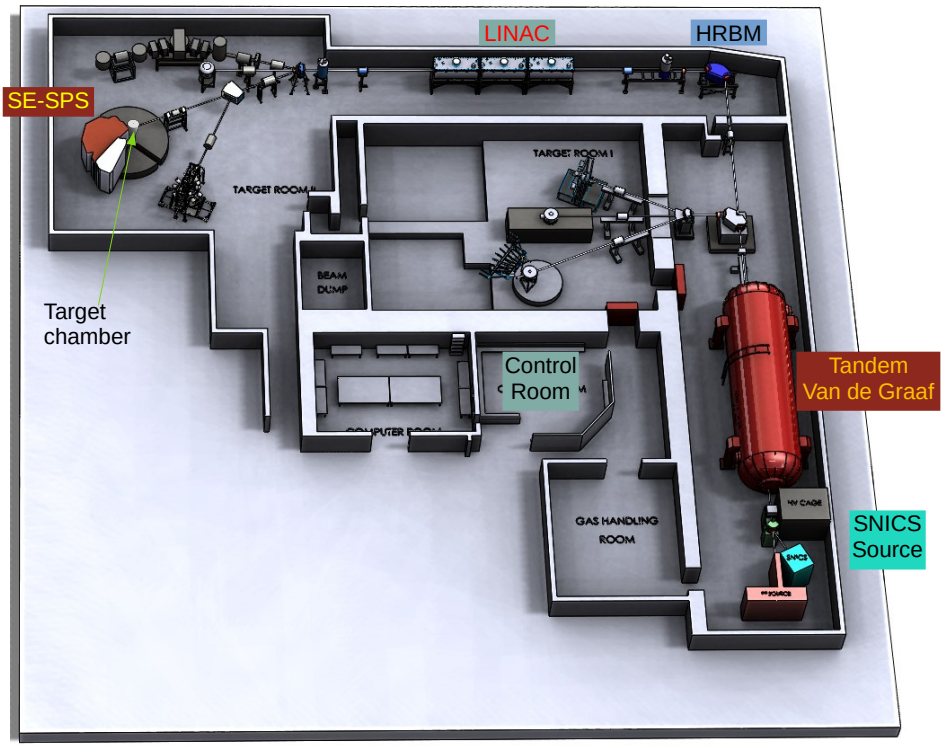

Figure 2.2. Floor layout at the FSU John D. Fox laboratory, showing key features that are of relevance to the beamline used in the present experiment. The LINAC was not used in the experiment. The pink box next to the SNICS source to the bottom right is the RF-discharge source used to synthesize beams of gaseous elements. This element is also unused in the present experiment. Reproduced from [72].

2.2. Super Enge Split-Pole Spectrograph

The successful development of particle accelerators such as the Tandem van de Graaff accelerator capable of producing beams of well-defined energy and stability in the 1960s made it important to develop spectrometers that could fully exploit the precision afforded by these beams. The design and development of the Split-Pole Spectrograph (SPS) by Harald A. Enge was intended to meet this demand, with the original design providing a momentum resolution of 2×10^{-4} [73]. True to its name, the Super Enge Split-pole Spectrograph (SE-SPS) utilizes a magnet split into two pole pieces with a field-free region in between (Fig. 2.1). Charged particles emerging from the irradiated target experience the field's ($\vec{B}$) magnetic Lorentz force ($\vec{F}$), and are bent in circular trajectories within the two poles — resulting in the separation of the particles to a high precision based on their momenta. If the particle has mass m and charge q, moving at velocity $\vec{v}$, the force acts perpendicular to its trajectory forcing it to move in a circular trajectory of radius ρ. At the energy ranges of interest, the equations governing the motion of the charged particle within a single magnetic region are found as [73, 74]:

$$\vec{F} = q\vec{v} \times \vec{B} \tag{2.1}$$

$$B\rho = \frac{mv}{q} = \frac{\sqrt{2mE}}{q} \tag{2.2}$$

where E is the non-relativistic kinetic energy of the particle. The quantity $B\rho$ is labeled the magnetic rigidity, and is directly proportional to the particle's momentum for a particular m and q. The chief operating principle of the SPS is contained within the expressions above. At constant magnetic field, particles with a larger momentum move in trajectories with larger radii of curvature ρ. All additional corrections in the design — including the split pole and the differing pole shapes — aid in minimizing higher-order aberrations within the spectrograph caused by various effects such as fringe fields at the magnet boundaries, and effects of kinematic broadening. The existence of two split poles with a field-free region in

between is crucial to the design of the SPS, with the fringe-field regions being deliberately designed to focus particles of a given species horizontally to second order with additional vertical focusing.

The current FSU Super Enge SPS [75] weighs about 35 tons, has an acceptance of 12.8 msr (one of the largest of its kind, which gives it the 'super' in its name), and is capable of a maximum magnetic field of 16.3 kG. The geometry of its design permits a range of $51 - 92$ cm for ρ. For a particle with momentum p detected at focal-plane position x, the SPS has a resolving power close to the original design with $\delta p/p = 1/4290$, and a dispersion $D = \Delta x/\Delta p \approx 1.96$. (Quantities Δx, Δp represent the full width at the base of each position, momentum peaks). The installation of the spectrograph at its present location in the John D. Fox Laboratory began in the Spring of 2016, with the first successful in-beam test completed in June 2018, using only the focal plane detector. The first successful test using both the focal plane detector and SABRE was completed in September 2019 as discussed below [68].

2.3. Focal Plane Detector and Electronics

At the exit of the spectrograph a chamber houses a position-sensitive ionization detector positioned along the focal plane, where the outgoing momentum-analysed particles are focused (Fig. 2.3). The focal plane detector is equipped with capabilities to perform particle identification, and redundant position measurements along two planes that allow corrections to the recorded position spectra to higher orders.

At its core, the focal plane detector is an ionization chamber with 6.35-micron aluminized mylar foils as its entrance and exit windows, holding isobutane gas within its volume at typical pressures of $100 - 300$ Torr. Charged particles traverse the active volume of the detector at an angle of 45 degrees to the plane of the entrance/exit windows, ionizing the isobutane gas. Field shaping elements are used to create a highly uniform vertical electric field in this active volume, i.e. the drift region. The drift region is defined by a cathode

plate that spans the entire extent of the detector's bottom, biased field-shaping wires on all four sides that are biased through a voltage divider, and a Frisch grid at the top of the drift region. The cathode plate is held at a negative potential with respect to the Frisch grid, while the Frisch grid itself is held at ground potential. The field-shaping wires on the sides serve to ramp up the potential smoothly and linearly through the entire volume of the grid — from the negative cathode plate to the grounded Frisch grid.

Above the Frisch grid sits two wire assemblies (front and rear) each with three anode wires, that are typically biased at a large positive voltage with respect to ground, in order to significantly increase the field density close to the wires. Above the two sets of anode wires are pick-up pads, which are connected to delay-line chips. The pick-up pads are separated into strips angled at about 45^o relative to the sides of the detector, which makes them parallel to particle trajectories. The pick-up pads are 0.09" wide each, and 1.4" long along their length, with a gap of 0.01" between successive pads, and are used for position sensing as described below. For additonal details about the position-sensitive ionization chamber and the field shaping wires, see references [76, 77, 78].

When the momentum-selected particles emerging from the magnetic pole pieces enter the detector, they ionize the gas as they move through the uniform-field drift region. After electrons produced via this ionization pass through the Frisch grid, the positive-biased anode wires attract the electrons towards them with the electric field increasing with approach as $1/r$, causing a Townsend avalanche of more electrons within the gas as they are accelerated towards the anode wires. This induces a signal in both the anode wires and the pick-up pads above them. The signals in each pick-up pad gets transmitted to the two ends of the focal plane via 50-ns delay-line integrated circuits that possess 10 taps, each tap thus offering a delay of 5 ns per pad. There being 440 pick-up pads in total along the detector's length, the overall time delay between signals reaching opposite ends of the delay-line spans a range of up to 2.2 μs, and the time difference between the delay-line signals at the ends of the detector can thus determine the particle position to high precision ($\approx$ 0.5mm, or 1 ns) [76].

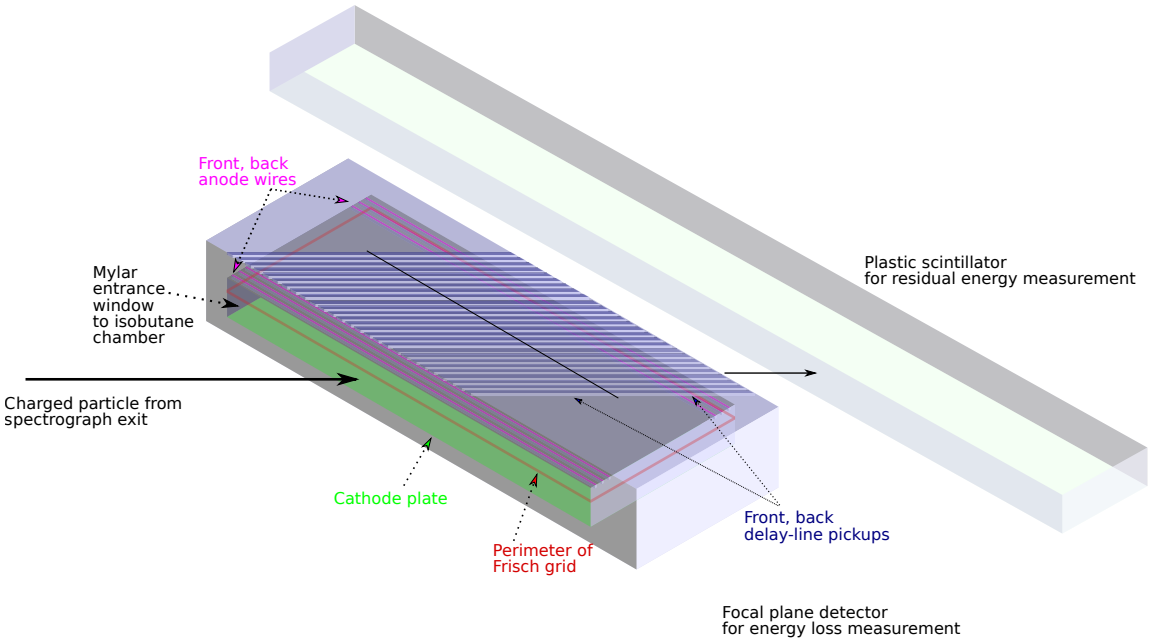

Figure 2.3. Simplified diagram of the focal plane detector, showing the position of various signal sources labelled by color. Not to scale.

The position of detected particles along the focal plane as determined using the delay-line readouts can be directly related to their momenta, and thus their kinetic energy, which in turn is related to the excitation energy of the state populated in the heavy reaction product.

At the same time, the cathode plate attracts the positively charged ions of the ionized gas towards it, capturing a measurement of particle energy loss (ΔE) within the gas. The induced signals on the anode wires are also read out and provide a redundant measurement of the same quantity. After the charged particle from the spectrograph exits the detector via the exit window, it is stopped in a thick plastic scintillator. The scintillator bar is attached to photomultiplier tubes on either end, providing a measurement of the residual energy (E) of the particle after its passage through the ionization chamber. Combining the position, ΔE and E information recorded over multiple events, it becomes possible to perform particle identification by exploiting the Bethe-Bloch equation, which relates the energy loss ΔE of a particle with mass A, charge Z, and initial kinetic energy E in a medium [77] with the approximate relationship given by

$$\Delta E \propto AZ^2/E \tag{2.3}$$

Figure 2.4 gives an example spectrum from a prior Split-pole spectrograph measurement that performed particle identification using this approach.

The plastic scintillator also performs the important function of providing a fast readout signal that is generated within a few nanoseconds of the particle traversing through the focal plane detector, which is crucial for precisely timing the event. As will be seen in detail subsequently, this nearly instantaneous scintillator readout of the residual energy event unobstructed by inherent delays due to gas ionization and delay-line timescales, proves vital towards engineering a time-coincidence logic that automatically selects events in other detectors within a fixed time-window of the arrival of the charged particle to the focal plane.

To perform two separate position measurements, the detector has two sets of pick-up pads and delay-line chips, one set closer to the entrance window and another close to the

exit window. Combining position information from these two planes (which also possess separate anode wires) during post-processing can provide particle trajectory information for particular energies, which can be used to correct for higher order kinematic aberration effects than those accounted for by the spectrograph offering improved resolution of the measured particle momenta.

In a typical experimental setup, signals from all the different parts of the focal plane detector system are read out for further analysis using suitable preamplifiers. The output signals from the photomultiplier tubes coupled to the scintillator are preamplified by ORTEC 113 scintillation preamplifiers [79] before they are sent to the data-acquisition system. Signals from delay-line readouts are preamplified by Canberra/Mirion 2003BT charge-sensitive preamplifiers [80], followed by pulse-shaping using a timing-filter amplifier (TFA) such as ORTEC 474 [81]. Use of TFAs in this manner allows finer control of the signal's shape before it gets processed by CAEN digitizers that calculate their arrival time to high precision using a digital constant-fraction disciminator algorithm, as will be discussed later. Careful pulse shaping and noise suppression aimed at achieving precise timing recorded by the digitizers is an important component of recording a reliable focal-plane spectrum.

Signals arising from the focal-plane gas-ionization chamber's cathode plate and anode wires are similarly preamplified and passed through ORTEC 474 timing-filter amplifiers prior to their being sent to CAEN digitizers. The choice of preamplifier used with these signals is less critical than for those for the scintillator and delay-line signals, since there is relatively less of a demand on these signals to have very precise timing characteristics. Models such as ORTEC VT120B fast-timing preamplifiers [82], Canberra/Mirion 2003BT charge-sensitive preamplifiers [80] and other preamplifiers have been successfully used for these signals in prior experiments, with the emphasis in each case placed on achieving the best possible separation between particle energy-loss (ΔE) signals arising from different particle groups entering the detector, which is also a function of other variables such as the particle kinetic energy, the isobutane gas pressure used, and the bias applied to the detector components.

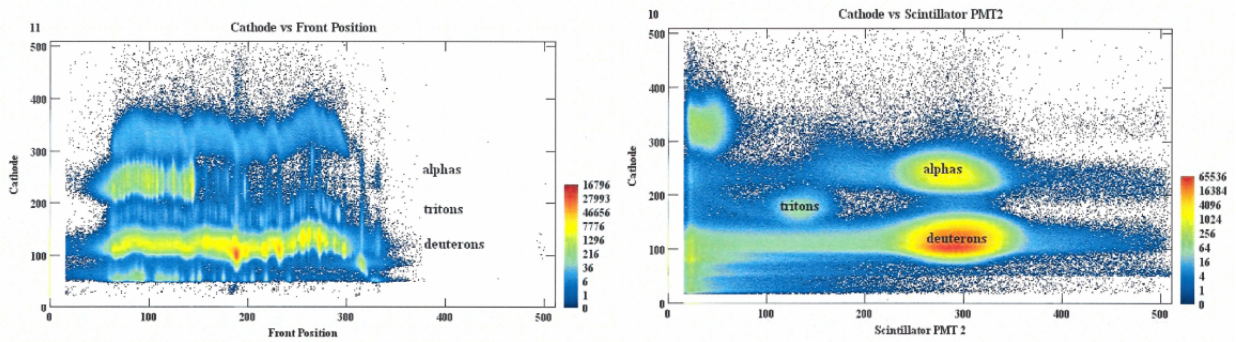

Figure 2.4. Sample particle ID spectra using cathode signals as ΔE versus focal-plane position (left), and the same cathode signals versus the scintillator readouts as the E signal (right), for a measurement using a ^{27}Al target and a ^{3}He beam. Reproduced from [76].

2.4. SABRE: The Silicon Array for Branching Ratio Experiments

When the SPS was in use at Yale, YLSA, the five-detector, lampshade-shaped silicon semiconductor array was used to detect charged-particle decays of the heavy product. The five segments of YLSA were YY1 Si detectors manufactured by Micron Semiconductor Ltd. The lampshade design was chosen to allow the best possible geometric efficiency given the shape of a single detector. The total solid-angle coverage of YLSA was $\sim$ 14% of 4π [76]. During the design of SABRE performed in 2016, YLSA's main features were retained — the lampshade design with the beam passing through its central axis, and oriented at backward angles upstream of the target. However, the redesign incorporated new $400\mu m$-thick MMM model Si-strip detectors from Micron, which have a larger surface area in comparison to YY1's arising from a larger outer radius, and a smaller inner radius (see Fig. 2.5). The resulting mount design was optimized using Monte Carlo simulations to maximize solid-angle coverage with respect to the target position by former LSU graduate student Dr. Erin Good, and adjusted subsequently by then LSU post-doctoral fellow Dr. Kevin Macon. The optimized design combined with the increased surface area of the detectors more than doubled SABRE's solid-angle coverage as compared to YLSA, allowing about 30% geometric efficiency in detecting coincident events with respect to the focal plane (see Fig. 2.5).

Two different types of MMM detectors were purchased for SABRE. Both possess identical

external geometry, but differ in their thickness, and in the depth of their so-called 'dead layer'. The dead layer of a semiconductor detector in operation under reverse bias, is the region of semiconductor (silicon in our case) that does not form a part of the depeletion region of the P-N junction. A charged particle entering the detector only causes an increase in the reverse leakage current (leading to its detection) when it arrives at the depeletion region. This means that the dead layer only serves to degrade the incoming charged particle's energy without providing measurable current [77]. The first set of MMM detectors purchased has a nominal thickness of 400 μm, with a dead-layer thickness of 500 nm. Using particle energy-loss tables [83], this can be verified to be a 90 keV minimum kinetic energy for protons before they reach the depeletion region and produce measurable current - making up a particle detection 'threshold' in energy. This set, owing to its thickness, is better suited for measurements involving higher-energy charged particles for which loss in the dead layer results in a relatively small correction to their energy.

For measurements that prioritize precise detection of low-energy charged particles in SABRE, the second set of MMM detectors are better suited since they come with a nominal thickness of 500 μm and a dead-layer thickness of 50 nm, which translates into a proton energy threshold of only 10 keV. As will be seen subsequently, it is this set that was utilized in the measurements described in this thesis in the interest of optimizing the apparatus for the best chance at reliably detecting proton decay events with energies < 240 keV expected to be deposited in the silicon detectors.

The YY1 detectors used by YLSA had 16 annular segments along the junction side that parametrized the polar angle θ corresponding to the detection, and a single segment in the ohmic side, providing no finer parametrization along azimuthal angle ϕ. The MMM detectors retain the 16 annular segments in the junction side, but possess 8 sector-shaped segments along the ohmic side that also provide angular information along the azimuthal angle ϕ for each particle detection. The segments along θ in the MMM detectors have larger radii, subtend larger solid angles around the target in comparison to the YY1 detectors, and cover

a wider overall angular range. While this increases the angular position uncertainty along θ for particles detected in each segment, it allows for larger statistics to be gathered in each angular bin and a wider angular range to be covered, which enhances SABRE's capability in measuring particle angular distributions. In particular, for the present measurement, we use SABRE to measure the angular distributions for the decay particles in time coincidence with precisely-timed focal plane events from the scintillator that correspond to excitation energies of the heavy product undergoing the charged-particle decay. Analysis of these angular distributions can then provide us with further information about the spectroscopic properties of the heavy product's quantum state that leads to the decay, such as their spin and/or their branching ratios. As indicated by Monte Carlo simulations of the current design, SABRE covers an angular range in the polar angle θ of approximately 110 to 165 degrees in the lab frame.

Signals from SABRE are preamplified using LSU-designed preamplifier boxes [84] that are attached to the target chamber, which also carry the reverse-bias voltage that gets applied to each of SABRE's MMM detectors. Each preamplifier box contains up to 72 charge-sensitive preamplifier chips with a gain of 27 mV/MeV [85]. After preamplification, signals are sent to Mesytec MDU-16 modules [86], which add a differential linear-amplification stage to the tail pulse generated by preamplifier chips. These modules are capable of applying a global gain to all 16 input channels that is variable via a rotary switch on the front panel. LEMO outputs from the MDU-16s are then sent via LEMO-MCX cables to CAEN digitizers. Ribbon cables transporting preamplified signals between the preamplifier boxes and MDU-16 modules act as a significant source of noise to SABRE signals. Sufficient shielding of these cables, and careful elimination of ground loops makes up a significant part of configuring SABRE for effective detection of low-energy charged particles.

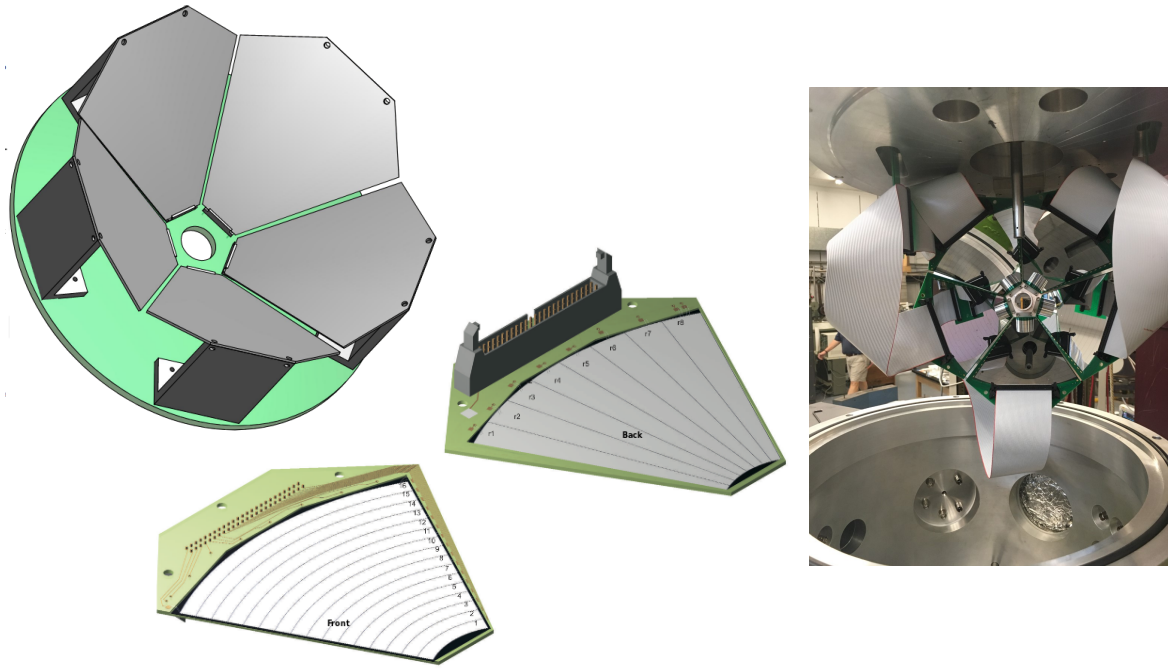

Figure 2.5. 3D rendering of the lampshade-shaped SABRE array (top left), along with the junction-side (left bottom) and the ohmic-side (middle) views of the segmented Micron MMM Si-strip detectors used in its design. On the right, is a photograph of SABRE mounted onto the lid of the target chamber, prior to being lowered into the chamber for a measurement, reproduced from [87].

2.5. Signal Processing and Data Acquisition Using CAEN Digitizers

2.5.1. Introduction: analog vs digital signal processing

Traditionally, raw signals from a detector are usually preamplified before being sent over longer signal lines so as to reduce distortions due to attenuation/dispersion. Considerable thought also goes into signal processing to gather physically meaningful data, which typically involves extracting the pulse's properties such as its charge content (integral of current over time in a current pulse), the pulse amplitude (pulse height in the case of a preamplified voltage pulse), and/or their timing with respect to other detected pulses.

During its operation at Yale, the SPS used conventional electronics based on NIM and VME standards for data acquisition [76]. Analog shaping amplifiers were used with peak-sensing Analog-to-Digital (ADC) and Time-to-Digital (TDC) converters that recorded energy and timing signals, respectively, arising from the focal plane detector and YLSA. Data was readout over a VME bus and transferred to a computer via an ethernet link. Coincident detection was ensured using a suitably tailored 'gate' pulse, which was triggered by a fast pulse from the spectrograph's focal plane detector (typically the scintillator signal) and stayed open for a long enough time duration to ensure no correlated event in other detectors was missed during the interval. NIM logic ('veto') was also utilized in this system to avoid recording new data when prior events were still being processed by the data-acquisition system (DAQ). While this approach was able to attain dead times of less than 5% during some experiments [76], there was potential for improvement *vis-a-vis* maximum data-acquisition rates and the lower limit on pulse energies measurable above noise. Since charged-particle captures to resonant states close to the particle thresholds are important towards better understanding of astrophysical phenomena, it becomes crucial to develop and improve experimental capabilities to reliably detect low-energy charged-particle decays. Particle decays from states closer to emission thresholds in astrophysically important nuclei are typically associated with smaller proton-branching ratios Γ_p/Γ. This makes it important to develop

experimental capabilities that can reliably detect the small number of expected particle decays from these states, and clearly separate them from random background counts.

Progress in semiconductor electronics over the past decades, especially with regard to Field-Programmable Gate Arrays (FPGA) [88, 89] have offered additional improvements to the workflow discussed above. Since the fastest timescale seen in the SE-SPS's detector pulse waveforms is $\approx 10^{-9}s$, available programmable logic switching at that timescale can now digitize each received signal to then process the waveforms using a suitable algorithm and dispatch/store the processed results to a data-acquisition system. These new modules, aptly named digitizers, greatly simplify the signal chain involved in the data-acquisition process, encapsulating the shaping amplifier+ADC/TDC system in a single digital unit. FPGAs can be regarded as a collection of semiconductor logic blocks that re-wire interconnections between themselves at power-on by reading once from a user-defined lookup table. In essence, this creates a circuit capable of re-wiring itself at startup. The digitizer clock sets up the sampling interval of the internal ADC, and assigns timestamps to each detected event. Interfacing the FPGA to a high-level computer allows manipulation of contents of the lookup table, which helps fine tune pulse-shaping and detection parameters at the per-channel level so as to allow for optimization of the signal processing routine. Once the optimization is performed, the FPGA system behaves identically to the analog system in detecting signals and transmitting their properties to the data-acquisition computer over a suitable communication interface — with the added benefits of fine-grained control for each channel via a software interface leading to less physical manipulation of cables/components, and easy addition/removal of custom digital filtering stages to the signal-processing chain. Digitizing waveforms this way also offers better correction for pileup events via deconvolution of waveforms when possible, and the possibility of monitoring real-time waveforms using software, without having to physically move cables.

Depending on the kind of signals involved, there are well-established filtering algorithms that can generate energy/timing information from the signals such as Trapezoidal Filtering

[90], and Charge Integration [91]. Trapezoidal filtering essentially transforms long-tailed energy pulses from a preamplifier into a shorter trapezoidal-shaped signal whose height is a robust measure of the pulse amplitude [90]. Performing a similar transformation as an analog shaping amplifier, this algorithm is useful in processing energy pulses such as those output by SABRE and the anode/scintillator signals from the focal plane detector (see Fig. 2.6 right).

In other applications, we require precise timing information from a sharp, narrow pulse. The energy information contained in these pulses would now be better represented by the pulse integral instead of the height, owing to its shorter duration (see Fig. 2.6 left). An example of this situation is the analysis of signals arising from the ends of the focal-plane delay-lines, the timing of which needs to be known to high precision in order to maximize position resolution of the spectrograph. The energy information in these signals is auxiliary and less important in the analysis.

In order to generate preamplifier-signal triggering information in Trapezoidal Filtering, it is sufficient to utilize a second-derivative filter like RC-CR2 [77]. However, for shorter pulses for which numerical derivatives could degrade the signal amplitude, performing a digital Constant-Fraction Discrimination (digital CFD, which mimicks the methods of analog Constant-Fraction Discrimination) can offer a sharper precision for pulse arrival timing via interpolation to arrive at the zero-crossing [77]. Digital CFD also has similar resistance as analog CFD to jitter in the recorded timestamp caused by distortions in pulse-shape across energy. The charge-integration algorithm utilized in the present setup uses CAEN's PSD (Pulse Shape Discrimination) firmware, the features of which are very close to the discussion in Ref. [91, 92].

One major challenge in utilizing digitizers for data analysis arises from the comparatively larger volume of data that they generate, at much higher rates than conventional electronics. The CAEN v1730/25 digitizer modules used with SABRE generate independent trigger timestamps for every channel, as opposed to the use of a gate pulse to achieve efficient

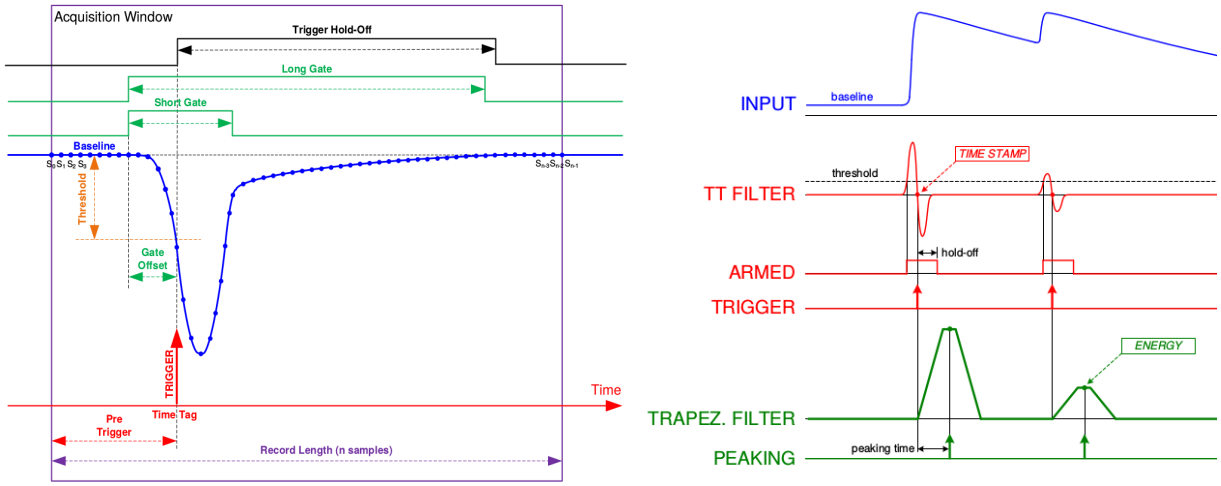

Figure 2.6. Schematic of digital pulse processing under various FPGA algorithms. Left: The PSD (Pulse Shape Discrimination) algorithm shown uses leading-edge detection for trigger timing (shown in red), and calculates the energy by numerically integrating the input (in blue) over the long-gate's duration. Right: In the case of the PHA (Pulse Height Analysis) algorithm, the TT (timing-threshold) filter signal is the numerical second-derivative of the input. This generates the time trigger at the first zero-crossing after the TT signal exceeds threshold. The conversion of the input to the trapezoidal profile is detailed in [90]. The energy of the pulse is estimated by the height of the trapezoid. Images sourced from [93].

rejection of uncorrelated events. Thus, there is a need to sort through recorded data and match timestamps to study and analyse correlated events periodically during the course of an experiment, to provide feedback on the quality of data being gathered. The capability to tailor the FPGA structure offers the possibility of rejecting events that are not in suitable coincidence. This feature, if carefully implemented, is capable of allowing reduction in data throughput and offer faster post-processing. This shall be the focus of Section 2.5.3.

2.5.2. Developing a fully digitized data-acquisition system for coincident measurements

In order to develop a robust, improved data-acquisition scheme that incorporated all components of the FSU SE-SPS, several alternative approaches were initally explored. The first scheme implemented used conventional electronics, and only handled signals from the focal plane detector. This data-acquisition system (DAQ) utilized NSCLDAQ [94], a software

widely used in low-energy nuclear physics experiments, developed at the National Superconducting Cyclotron Lab (NSCL) at Michigan State University. Under this scheme, all the different focal plane detector signals arising from various ADC/TDC modules were encapsulated into a suitable readout program that utilized a Wiener VM-USB module to interface data transfer between the VME ADC/TDC modules and the computer via a USB link. The program saved all focal plane data in binary format while offering capabilities to generate real-time spectra using NSCL SpecTcl [94]. This was the status of the project when the author started working on incorporating SABRE into the DAQ scheme in Summer 2018. The original goal was to retain conventional electronics for the focal plane detector while extending the program to additionally handle, in real time, the coincident data generated by CAEN digitizers connected to SABRE.

During the development and testing of the NSCLDAQ-based integrated DAQ system, a few issues emerged. First, the large event rates encountered (> 2 kHz per channel) when the digitizers operated at sufficiently low discriminator thresholds demanded excellent software optimization for both the proprietary CAEN libraries [95] that made up the backend, and NSCLDAQ data structures and eventbuilder that made up the frontend. This often translated into the experience of encountering bugs in either component that were not always simple to isolate, and increased development times. Second, the integration of conventional and digitizer-based DAQ systems in a single program led to difficulties when attempting repeated reconfigurations of FPGA settings during the course of an experiment. Due to these reasons, this appoach was de-prioritized in Fall 2019 in pursuit of a simpler approach that used digitizers for all signals, both from the focal plane detector and SABRE. It bears mentioning here that many of these issues were subsequently resolved, with much invaluable assistance from Dr. Ron Fox at NSCL. As of Fall 2021, well-developed C++ data structures that encapsulate capabilities derived from CAEN's CAENDigitizer libraries [95] to generate derived classes representing sources and triggers were developed and bench tested at LSU for CAEN Digitizer models 1730 and 1725, running firmwares DPP-PHA and DPP-PSD. In

order to aid with editing the digitizer parameters in real time, a Tcl [96] front-end was also developed.

The new approach sought to eventbuild in post-processing, using data recorded by CAEN's proprietary digitizer frontend CoMPASS [93]. This had the advantage of encapsulating all the software control components into one unit, with the focus of all the subsequent development resting on analyzing the gathered data. To encapsulate all signals into a single CAEN CoMPASS [93] graphical frontend, dedicated tests that processed focal plane detector signals using digitizers were performed and a one-to-one comparison with data processed via analog electronics was done to validate performance when making the transition from the well-characterized TDC/ADC system. CAEN digitizers of different models, running both DPP-PSD and DPP-PHA firmware had already been well interfaced using CoMPASS by CAEN, and this method quickly evolved to become capable of performing tests with real data in order to benchmark the overall setup, and ensure the central logic involved in accurately identifying coincidences was fleshed out.

Upon performing a few tests using just the focal-plane signals, it was found that the use of a single digitizer running the digital CFD based PSD firmware [92] would be suitable for all the signals arising from the focal plane detector: delay-line outputs, anode/cathode readouts, and scintillator pulses from the two Photomultiplier tubes (PMT). This particular setup also provided the additional advantage of individual timestamps on each focal-plane signal. This capability provided more fine-grained information about signal timings within the focal plane, compared to the conventional 'gate'-based acquisition which assigned one timestamp for all focal-plane signals within the gate.

A handful of ROOT [97] macros to perform post-processing and eventbuilding of recorded timestamped data were originally developed during Fall 2019, so as to periodically generate histograms to assess an experiment's progress. The author was part of a small team of LSU and FSU graduate students and post-doctoral fellows involved in developing this post-processing algorithm, which has since evolved to incorporate varied applications. In

Sept-Oct 2019, the all-digitized DAQ approach discussed above was to be used in an in-beam commissioning run of the SE-SPS+SABRE apparatus to study the ^{19}F(p,α)^{16}O(α)^{12}C reaction populating excited states in ^{16}O with well-known α-branching ratios. In preparation for this test, the following studies were performed:

- The focal-plane position resolution obtainable using digitizers running PSD firmware on delay-line readouts was verified to be comparable to that obtained using the VME-bus based system in use previously. The best available focal-plane energy resolution achieved is currently about 30-keV FWHM at 5.486 MeV using either approach when using a ^{241}Am radioactive source. The resulting focal-plane spectrum is shown in Fig. 2.7, where the two intense α decays separated by around 40 keV in energy, are visibly resolved.

- The dead-layer thickness present in each of the MMM-type detectors was measured at LSU in Summer 2019, and verified to be close to the nominal value of $\sim$ 50 nm as provided by the manufacturer.

- The combination of preamplifier chips used and V1730/25 digitizers were also verified to lead to no significant degradation in energy resolution when signals with low pulse heights were detected using the system at low rates. In a bench test using input signals sent through the same preamplifier circuits as used by SABRE, the energy resolution generated by the trapezoidal filter stayed constant at $\sim$ 25 keV when the input pulse height was lowered in small steps to well below (down to mean $\sim$250 keV) the detection threshold set for the timing-trigger RC-CR2 filter at $\sim$ 400 keV.

To expand on the final bullet-point above, the differential nature of the RC-CR2 filter used for channel self-triggering was sensitive to shape distortions (particularly rise-time distortions) seen in the preamplifier output. As the input pulse's energy was lowered below the RC-CR2 detection threshold set at 400 keV, the variability in pulse-shapes cause the trigger condition to be met for a small subset of pulses with distortions amplified by the RC-CR2

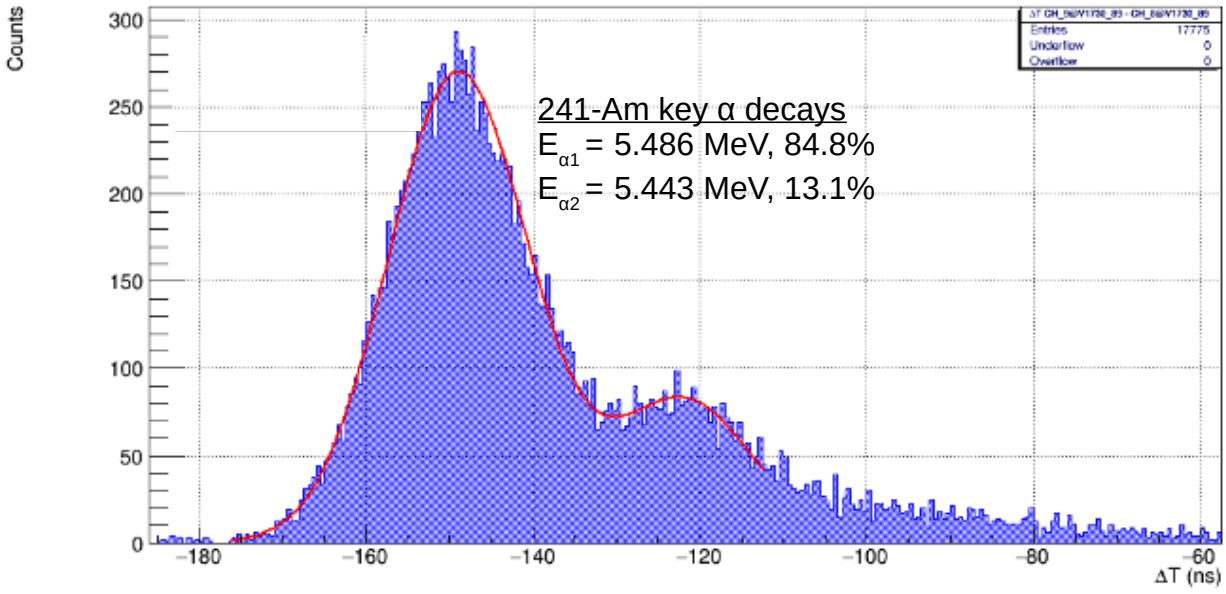

Figure 2.7. Focal-plane spectrum from an ^{241}Am source recorded using a CAEN v1730 digitizer running DPP-PSD, showing clear resolution of the two decay α peaks with an energy difference of roughly 40 keV. Subsequent tests revealed the best focal-plane resolution attainable using digitizers to be ≈30 keV at this energy, which was comparable to the results found using the analog DAQ setup that preceded the digitizers. Figure courtesy of Dr. Kevin Macon.

filter. When these detected pulses are shaped to measure their energy, the trapezoidal filter used for the purpose does not lead to distorted energy measurements even when pulses are detected below the set threshold. (see Fig. 2.8). The absence of a sharp cut-off at a chosen threshold highlights the importance of setting RC-CR2 detection thresholds as low as possible when detecting low-energy signals. In turn, this requires careful elimination of as much hardware noise in the system as is attainable.

A basic implementation of the eventbuilder macro, the central logic of which shall be discussed subsequently, was used to successfully analyze data from the Sept-Oct 2019 measurement, the results of which are discussed in detail in [68, 87]. Briefly, this test involved the coincident detection of light reaction products at the focal plane and decay particles in SABRE from excited states in ^{16}O with 100% α-branching ratios populated by the reaction

^{19}F(p,α)^{16}O. One key takeaway from this experiment was the need to fully implement, and exploit the digitizers' capability to perform real-time selection of coincident events to be written to disk, which the author was subsequently tasked with implementing in full. The following key conclusions emerged during this study:

- The absence of any hardware coincidence capabilities in the setup meant that signals in SABRE were only resolved above the noise floor when they had an energy deposit larger than $\approx$ 1000 keV. This was not all that surprising, due to the large rates of background particle detections seen in SABRE channels due to beam backscattering from the target at close proximity.

- Another difficulty that became apparent during several tests before and after this measurement, was the instability observed when writing large data throughputs recorded over more than 120 channels. Discriminator thresholds lower than 100 LSB in DPP-PHA led to hardware or software overheads becoming unsustainable, and programs and/or kernels crashing during data acquisition.

- As an indication of the limits of hardware capabilities observed during this experiment, the most optimized DAQ setup free from software crashes during the ^{19}F(p,α)^{16}O(α)^{12}C study required every SABRE channel see an event rate not more than 1000 Hz, when thresholds were set low enough (100 LSB) to reliably detect $\approx$1 MeV α-particles. Lower discriminator thresholds caused the trigger rates to increase further, leading to hardware/software instabilities.

- The successful determination of well-known α-particle branching ratios in ^{16}O [68, 87] demonstrated that the digitized focal plane, the eventbuilder logic, and the signal processing pipeline distributed across multiple channels had been implemented successfully.

The next section shall describe in detail the tests that were performed at LSU to set up digitizer coincidence logic, and how it was then incorporated into the SE-SPS+SABRE setup.

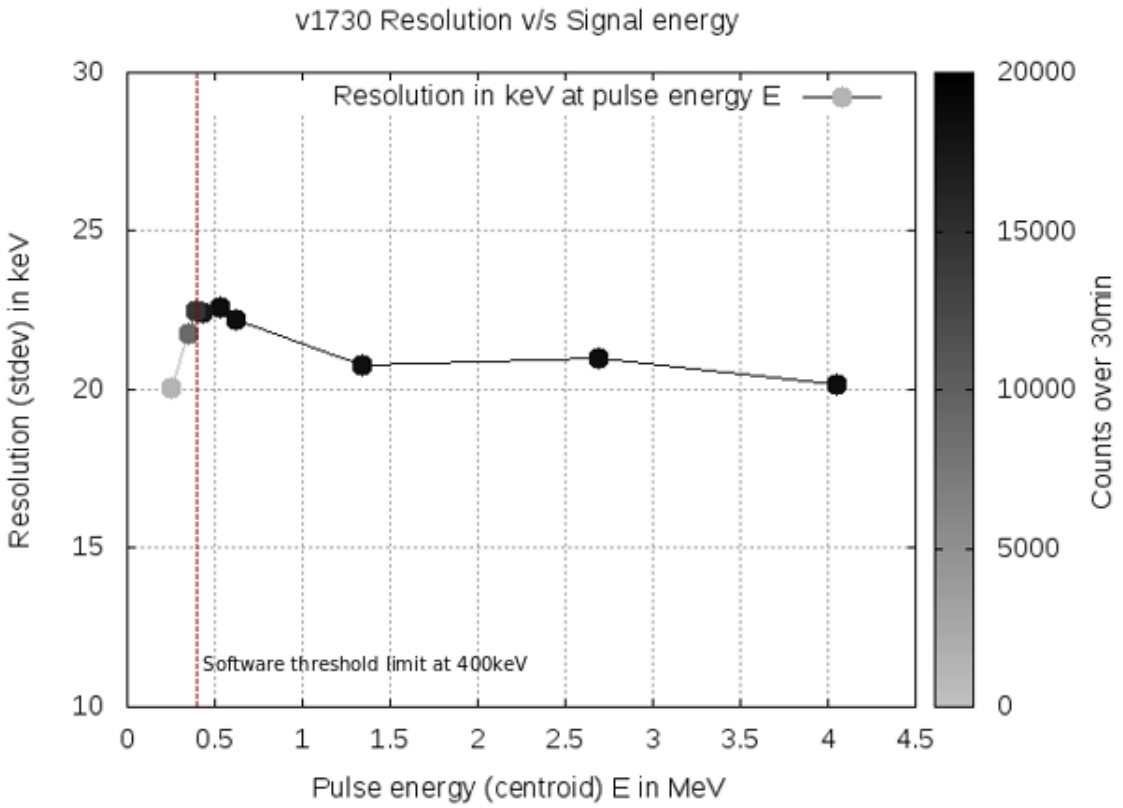

Figure 2.8. Digitizer resolution vs pulse height, as recorded with a CAEN v1730 digitizer running the PHA algorithm. As evidenced by the greyscale bar (right), events begin to be lost when the pulse-height is of the order of the FPGA discriminator threshold set for the RC-CR2 filter. The pulse heights on the X-axis have been calibrated to energy (E) units of MeV using an ^{241}Am radioactive source.

The first successful experiment that used this scheme was performed in February/March 2020 [87], followed by several successful measurements demonstrating its viability.

2.5.3. Trigger validation with CAEN digitizers: General principles

When considering the use of coincidence logic to cut down the throughput of recorded data from SABRE, there are several important design considerations to keep in mind:

- The fast-triggering scintillator signals emerge later in time than their coincident SABRE events. This means that implementing a simple GATE logic around SABRE signals, triggered by the arrival of a scintillator event is not straightforward.

- An in-principle solution to the above could be to delay all 120 channels from SABRE, to have them arrive later than the scintillator signals which could then be used to gate the SABRE signals. This step, though simple in principle, would be expensive to implement and fraught with risks of introducing new sources of electronic noise into SABRE's signal-processing chain. This was rendered doubly important by the additional goals involved in using SABRE to reliably detect low-energy charged particles.

- A good majority of software/hardware instability that was encountered during the commissioning run, were seen to be correlated with scenarios that involved the internal buffers of the digitizer being filled to capacity before they were read out by the computer interfaced with them. This indicated self-trigger rates filling up the digitizer's internal buffers at a faster rate than the rest of the system was capable of having them be read out. In addition to pointing to the need for some form of coincident triggering (that could lower input trigger rates seen by the digitizers), this also pointed to the potential utility in increasing readout rates of events from the digitizers.

The last bullet-point discussed above, was accomplished by a series of hardware upgrades and changes made to the computer system used to control the data acquisition:

- Firstly, valuable computing power was freed up by changing the format of data written to disk from ROOT trees, to binary data. The benefits to this step were readily apparent when examining system-load statistics. There was some cost incurred in overhauling the initial step in the eventbuilding pipeline to design it to parse binary data. However, there was also the added benefit of being able to sort events more efficiently in time, owing to CoMPASS storing events from every channel in separate binary files during data acquisition.

- Secondly, the Random Access Memory (RAM) in the Computer was upgraded to 64 GB, the maximum permissible value by the PC motherboard. While the effects of this step were less clear-cut, it had a significant impact in the overall workflow of an

experiment in permitting simultaneous analysis of previously recorded events while new data was being recorded.

- Lastly, and significantly, the data storage drive in the computer was upgraded from a standard hard-disk drive (HDD) offering read-write speeds capped at 80-200MB/s, to an NVMe M.2 solid-state drive that offered a dramatically larger sustained read/write speed at over 3 GB/s. This upgrade helped to temporarily push data-acquisition rates to as high as 10kHz per SABRE channel prior to the development of trigger validation schemes. The CONET2 optic-fiber link had a nominal data rate limited at 80MB per second [98], which was close to the lower end of the HDD read/write rate. This upgrade had the effect of smoothing out a large share of instabilities that were seen to occur surrounding disk access/write speeds in the lead-up to a software crash.

Despite the above fixes, there was still the important problem of implementing coincident triggering between the focal plane detector and SABRE, which was addressed by inspecting possible methods to exploit the inherent separation of control in CAEN digitizers, which is split between Mezzanine boards that digitize incoming data and identify self-triggering events, and the digitizer motherboard, which deals with the internal logic of the digitizer module, making decisions on what events are discarded and kept (see Fig. 2.10). A white paper released by CAEN [99] had already discussed several use cases of this nature, which eventually lead to a fruitful consultation with CAEN and the introduction of GUI features in CoMPASS that had hitherto required direct manipulation of digitizer registers. The core logic of the solution used, was identical to those described in Reference [68, 87] and several subsequent measurements.

Every digitizer channel configured to self-trigger continuously monitors voltage levels at its input - sampling them in intervals of the local clock units. The clock unit for CAEN 1730 is 2 ns (extendable to 2 ps via interpolation if digital CFD is used), and the clock unit for CAEN 1725 is 4 ns. This continuously monitored stream is processed in real time to generate two other streams, one of which serves to identify the time at which an event occurs (RC-

CR2, or digital CFD, as discussed in the caption to Fig. 2.6 - the timing-threshold filter), while the other is configured to make energy measurements from the original pulse. The clock tick corresponding to the trigger event is used to center the acquisition window that is sent to the energy measurement algorithm.

All of the above processing takes place at the Mezzanine level in every digitizer. Each time a trigger is registered in the Mezzanine on one of its channels via an RC-CR2/digital CFD zero crossing, or an over-threshold in leading-edge discrimination, it sends a synchronized logic pulse of user-configurable width (T_{ST}) called the 'Trigger Request' or the 'Shaped Trigger' in CAEN's documentation. The motherboard is in turn tasked with validating this trigger request with a logic signal of its own called the 'Trigger Validation (TRG_VAL)'. If the motherboard responds to a trigger request with a trigger validation signal in response, the recorded data is written to the local memory in each Mezzanine, and transferred out of the digitizer into the DAQ computer at the next polling interval. In the default mode of operation for a digitizer that had been under use during the commissioning run, the TRG_VAL is always held at 1 - which validates every self-trigger to be written to the digitizer's limited local memory, saturating it when the input trigger rate becomes unsustainably large. However, the TRG_VAL is also user-configurable to be sourced from a LEMO connection in the front panel of the digitizer labeled TRG_IN. (For other possible configurations, the curious reader is directed to the reference at [99]).

Figure 2.9 (adapted from [99]) describes the communication channels between digitizer mezzanines and the motherboard. Figure 2.10 is a timing diagram demonstrating how the trigger validation scheme works in practice.

As evident from the discussion above, the logic of trigger validation is perfectly tailored to the first concern raised in the beginning of this section, whereby fast-triggering scintillator signals are tasked with validating SABRE signals that arrive before them in time. If one configures every one of the SABRE digitizer channels to send to their motherboards trigger requests of suitably large width T_{ST}, one only needs to then configure each motherboard's

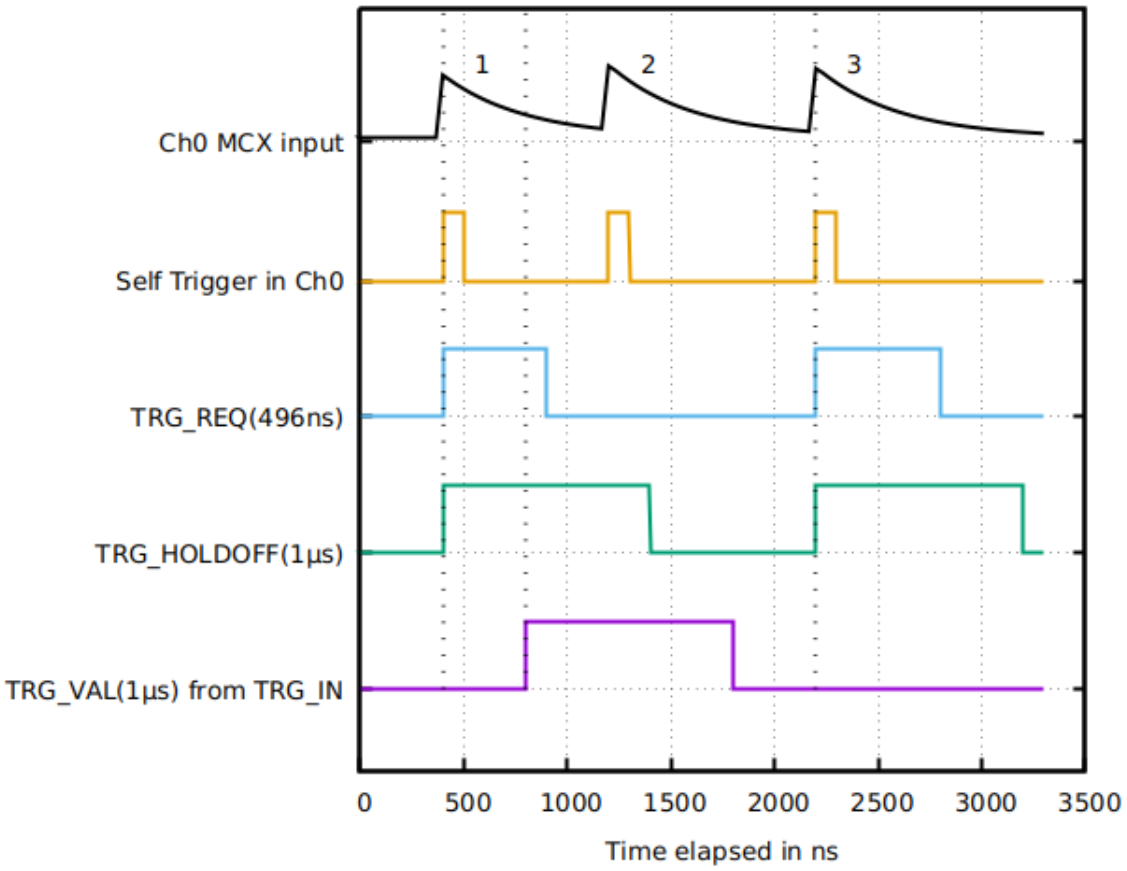

Figure 2.9. Timing diagram indicating the underlying logic involved in digitizer trigger validation. Three tail pulses (labeled 'Ch0 MCX input') from SABRE numbered 1, 2, and 3 reach MCX channel 0 of the digitizer, and register self-triggers in the Mezzanine labeled 'Self trigger in ch0'. Corresponding to events 1 and 3, a trigger request 'TRG_REQ' of width 496 ns is sent to the digitizer motherboard, and a trigger holdoff 'TRG_HOLDOFF' signal which is 1 μs wide is used to reject any new self-triggers that may arrive at channel 0 while events 1 and 3 are being processed. Tail pulse 2, hence, is discarded without a self-trigger since it arrives within the trigger holdoff duration of event 1. The trigger requests 'TRG_REQ' sent to the motherboard cause the tail pulses to be processed to calculate their energies, written to the local memory in the Mezzanines and readout by the DAQ Computer, if the motherboard receives a validation trigger in its external trigger input TRG_IN, labeled 'TRG_VAL'. As shown in Fig. 2.13, we source this external signal 'TRG_IN' from the fast scintillator triggers from the focal plane detector, to set up the coincidence condition with SABRE. Event 1 gets processed and written to disk since it receives a validation for its trigger request, while event 3 is discarded since no TRG_VAL arrived in time to validate its TRG_REQ.

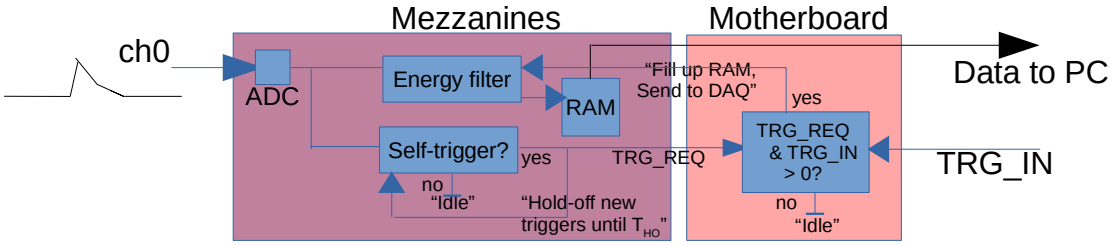

Figure 2.10. Sketch describing the flow of logic between CAEN Digitizer Mezzanines and the Motherboard during the trigger validation operation discussed in text. Figure adapted from the full logic diagram published in Reference [99], to only show the particular logic implemented as part of the experiment. Readers curious about other coincidence schemes are pointed to this reference for more details.

TRG_IN input to receive a validation logic signal synchronized with high precision to every scintillator pulse observed. This drastically cuts down the number of SABRE events that get stored into the digitizer internal memory buffers, and renders the data throughput significantly more manageable than in a configuration without a trigger-validation scheme present.

One expects the scintillator to fire at random at rates close to 500Hz when idle under bias without being subject to any beam - this rate arising from the room background. One expects this background rate to be uncorrelated with the background rate in SABRE - making any spurious events written due to their mutual validation a purely random event. This random background can be determined from the event rate seen at large time differences away from the time coincidence peak between SABRE and the scintillator signals. One final, yet important point to mention in this regard is about the digitizer parameter labeled 'Trigger Holdoff (TRG_HOLDOFF)'. This is a user configurable parameter that can be set to a fixed value T_{HO} in time in order for a channel to reject any new trigger that gets detected within an interval of $t = T_{HO}$ from the original trigger. In the event of large rates of data throughput or background, carefully setting the trigger holdoff can be a powerful method to limit the

maximum trigger rate seen by each digitizer channel, over and above the improvement offered by trigger validation.

The following subsection describes the first successful bench test that demonstrated the viability of the scheme described above.

2.5.4. Bench testing: Proof of concept

Immediately following the commissioning experiment, attention was focused on bench testing a trigger-validation scheme that demonstrates the capability of late-arriving scintillator triggers to validate SABRE triggers, thereby helping to cut down recorded data rates. In order to mock up a scenario similar to in-beam running conditions, the setup shown in Fig. 2.11 was wired at LSU. A large scintillator bar of NaI coupled to a photomultiplier tube was connected to an ORTEC PMT base capable of providing both tail shaped energy signals and fast timing signals corresponding to every particle-detection event. Linear fan-out NIM modules were used to split the energy signals in two, sending them to CAEN1725/30 digitizer inputs channels 1 and 2, programmed with DPP-PHA firmware in anticipation of the primary application with SABRE at FSU. When data acquisition is attempted with this configuration, the considerable size of the NaI bar succeeds in quickly building up a profile of the laboratory's ambient γ-ray spectrum. This is the red histogram in Fig. 2.12, which we take as the reference spectrum.

Our aim at this stage is to introduce a series of background events at a large event rate into one of the channels, and use trigger validation logic to retrieve the original spectrum. As shown in Fig. 2.11, Channel 1 was left undistubed to only see events from the NaI detector, while Channel 2 had fanned into it counts from a Berkeley Electronics PB-5 pulser the tail-pulse profile of which were configured to broadly match that of the NaI detector's energy output. Both Channels 0 and 1 were validated by a NIM pulse generated by delaying the fast timing output of the NaI detector by 2 μs.

The first point that was verified was the complete rejection of any coincident events

between channels 1 and 2 when the digitizer coincident window T_{ST} was set to a value smaller than 2 μs. When the coincident window was set to a value that was large enough to overlap with the delayed validation pulse sent to TRG_IN, say at 3 μs, the plots shown in black and green in Fig. 2.12 result for Channels 1 and 2, respectively. (The trigger holdoff was set to a value of 6 μs, as per the recommendation $T_{HO} = 2T_{TS}$ in reference [99] under the section 'double coincidences'.) As expected, Channel 1 without any background events fanned-in almost matches exactly with the reference room background gathered over the same duration. In spite of the highly intrusive 100 kHz trigger rate, it can be seen that Channel 2 traces well the broad features in the room background - with the only difference observed arising from a constant dead-time due in part to the excessively large background rates injected. (Both channels have some events at the lowest energy end missing, but this is likely explained by a drop in the amplitude of the timing output seen for low-energy events - which does not register the TRG_VAL as TRUE/1/HIGH in these cases.)

Trigger holdoffs are started by all events including backgrounds, which can then have the effect of having a randomly placed background pulse receiving a validation in lieu of an NaI signal. During an experiment, we expect the rate of such random coincidences to be lower, since the background rate is also expected to be a random Poisson process with a fixed mean rate. This effect, combined with other possibly unaccounted-for sources of deadtime in the system, makes a constant multiplicative correction factor necessary to extract branching ratios accurately during an experiment when background rates are high. As will be seen in subsequent chapters, this factor is determined by utilizing a reference state(s) with a well known branching ratio, which is analyzed using the same logic as those from states with unknown branching ratios. This bench test, hence, successfully established the viability of using digitizers for coincident detection using external digitizer trigger validation — the next subsection will discuss the full data-acquisition setup that was utilized during the experiment.

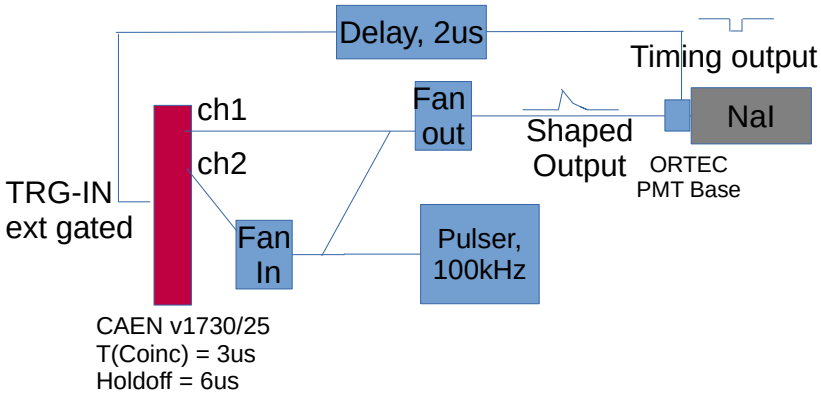

Figure 2.11. Bench-test setup at LSU that was used to study the elimination of a a simple high-frequency background using trigger validation in CAEN V1725/30 digitizers running DPP-PHA. The fast-timing output from the PMT attached to a NaI detector recording ambient γ-ray spectrum in the room, was used as the TRG_VAL signal for all digitizer channels, one of which had a high-background rate fanned in. As seen in Fig. 2.12, the validation was able to successfully retrieve salient features of the reference spectrum - losing a fixed fraction of the events to incurred deadtime effects.

2.5.5. Data-acquisiton setup

The final setup used in the experiment had the layout shown in Fig. 2.13. The gate-delay generator furthest to the left in this figure is used to start/stop the acquisition via a button press that triggers a NIM-level transition in this module's output. This transition is propagated through digitizers via LEMO cables that chain their TRG-OUT and S-IN connectors left to right, and serves to synchronously set to zero the internal timestamps in every digitizer at the start of every data-acquisition run.

The digitizer furthest to the right in Fig. 2.13 has a TRG-OUT connector unused in the start-stop propagation described above, and receives focal-plane signals. Hence, its TRG-OUT connector is instead used to propagate the logical-OR of self-triggers seen by its input channels connected to the focal-plane scintillator readout. This signal, which typically has two short pulses in rapid succession arising from the two scintillator readouts, is smoothed using a second gate-delay generator to a single pulse with a width of 2 μs, and a logic fan-out

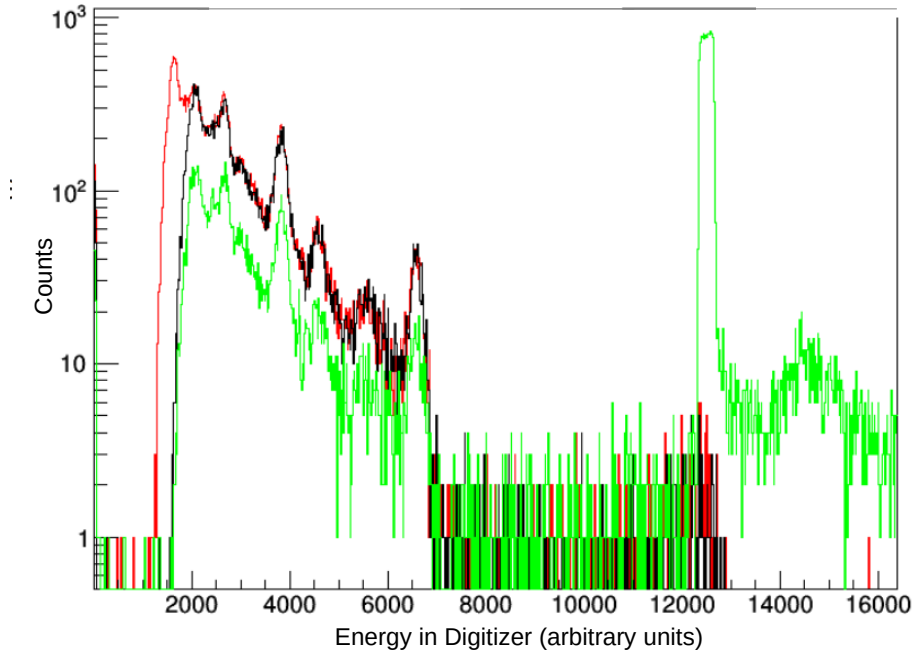

Figure 2.12. (Red) Ambient γ-ray spectrum recorded using the NaI detector in Fig. 2.11 and a single digitizer channel, with no additional logic. This spectrum is used as a reference to compare against those recorded with additional coincidence conditions imposed on the digitizer.
(Black) Ambient γ spectrum recorded by Channel 1 in Fig. 2.11 over the same run duration as the reference histogram - with added trigger validation from the NaI's timing output. Since there is no high-frequency background fanned in to this channel, it is almost identical in statistics to the reference histogram.
(Green) Ambient γ spectrum recorded by Channel 2 in the setup in Fig. 2.11, which uses a shaped-trigger window of $T_{ST} = 3$ μs to accept the trigger validation signal arriving with a delay of 2 μs. Features of the spectrum are retained, with a fraction of events (proportional to the injected background 'noise' rate) in Channel 2 being lost due to the trigger holdoffs T_{HO} arising from the high-frequency background. $T_{HO} = 6\mu$s is used in both Channel 1 and 2 in the Black and Green plots.

unit is used to send the resulting pulse to the TRG-IN LEMO connectors of all the other digitizers. This is the validation signal 'EXT_TRG_IN' in Fig. 2.12.

MCX connectors that connect the outputs from various detectors to the inputs of each digitizer are not shown for ease of depiction in Fig. 2.13, but are listed in the figure. Digitizers are interfaced to the data-acquisition computer via a CAEN A3818 bridge on a PCIe v3.0 slot. The green cables above, propagate the digitizer clock signals from the master board at the left end down the daisy-chain. For details of clock management and synchronization between digitizers, the interested reader is referred to the references at [93, 98].

This setup, coupled with all the other instruments described earlier in this chapter, was used to measure the two reactions that are the focus of this thesis, *viz.* ^{12}C(^{6}Li,α)^{14}N*(p)^{13}C and ^{28}Si(^{6}Li,t)^{31}S*(p)^{30}P. The following chapter discusses in detail the steps taken to set up and calibrate the combined system of detectors and DAQ towards making these measurements.

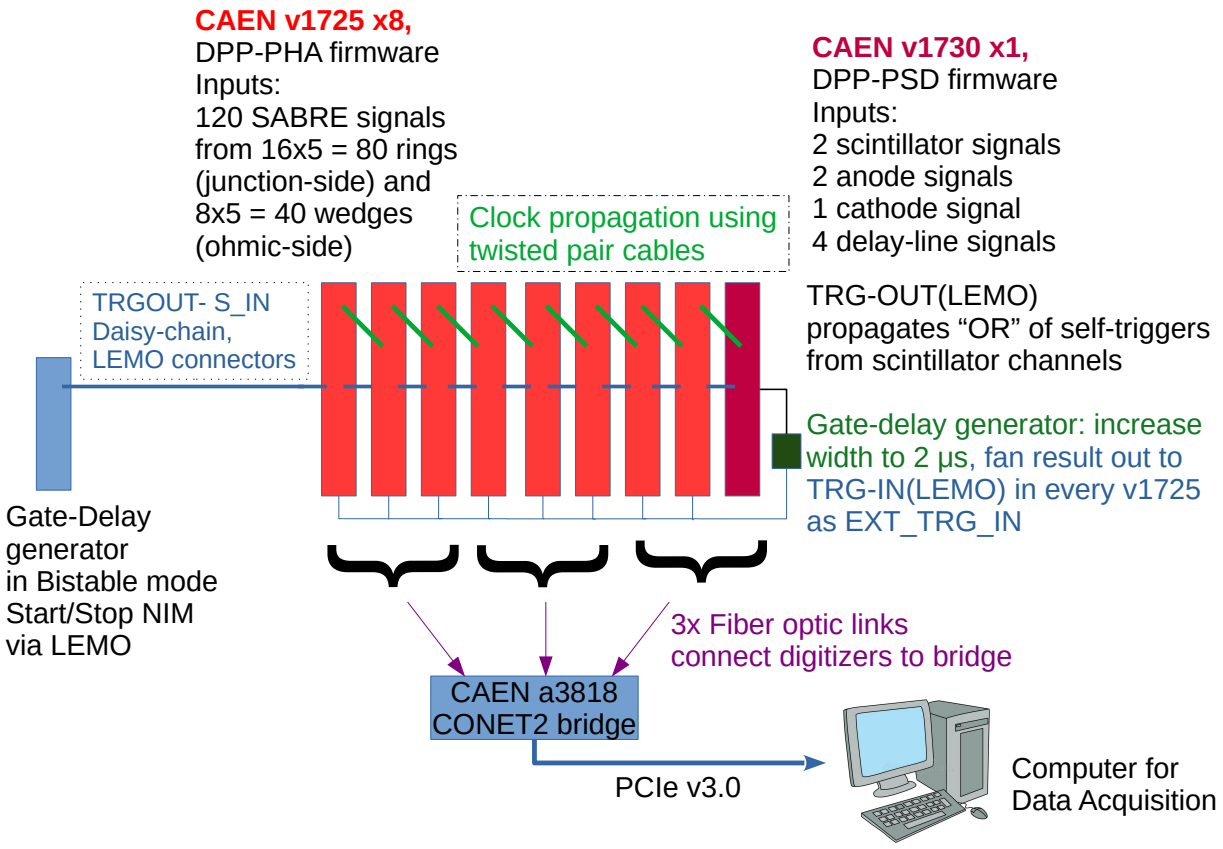

Figure 2.13. Sketch depicting the overall digitizer setup used in the experiment. See text for a detailed description.

Chapter 3. .Experiment and Data Analysis

The previous section described in detail the apparatus that was used to study proton-branching ratios in ^{31}S states in the astrophysically relevant region described in this work. The SE-SPS+SABRE system was set up to perform coincident measurements of two different transfer reactions, ^{12}C(^{6}Li,α)^{14}N*(p)^{13}C and ^{28}Si(^{6}Li,t)^{31}S*(p)^{30}P. For ease of reference, these two reactions shall be referred to as the ^{14}N measurement and the ^{31}S measurement, respectively.

Both measurements involved a $^{6}Li^{3+}$ beam generated by the SNICS negative-ion source, accelerated to a kinetic energy of 27 MeV using the FSU Tandem van de Graaff accelerator operated at a terminal potential of about 7.975 kV. In the ^{31}S measurement, the beam bombarded a natural SiO_2 target of thickness 87.6 μg/cm^2. This target (which will be referred to as the 'thick Si' target from here on) was self-supported, but showed a visible amount of carbon deposition on its surface from previous experiments - presumably arising from the various contaminants present in the target chamber vacuum such as sealant and pump oil vapor. The beam intensity of the ^{6}Li beam was observed to stay roughly constant throughout the course of the experiment at 100 enA on beam stop BS3, which was the closest beamstop to the target.

The ^{14}N measurement used the same beam impinging on a natural ^{12}C target of thickness 100 $\mu g/\mathrm{cm}^2$. Several resonances in ^{14}N just above the proton-separation energy have all been measured previously to have well-known proton-branching ratios close to 100%. Monte Carlo simulations of SABRE indicated that decay protons from the lowest proton-unbound state in ^{14}N at $E_x = 7.967$ MeV deposit an energy in the range of 180-240 keV in SABRE. In contrast, the lowermost ^{31}S resonance at $E_x = 6.636$ MeV that was aimed for was expected to deposit protons in SABRE with mean energies in the range 250-340 keV, which would lead to signals with larger amplitudes in SABRE's segments under identical conditions. One of the goals of the current measurement was to sufficiently minimize electronic noise as to perform an accurate measurement of the $E_x(^{14}N) = 7.967$ MeV resonance's proton-branching ratio. This

would allow us to obtain a sufficiently robust gauge on the noise floor in SABRE, and estimate the detection threshold for the ^{31}S measurement. In order to minimize corrections due to time-dependent sources of error, the ^{14}N measurement was performed in the middle of the ^{31}S measurement. Methods adopted towards signal validation and noise reduction permitted us to set digitizer detection thresholds as low as 60 LSB for each channel in SABRE, but not lower. After applying gain-matching corrections, this corresponds to a detection threshold in the range $100 - 130$ keV for the RC-CR2 filter in each SABRE channel, which ensured that no tail pulses recorded by SABRE at the lowest desired limit of 180 keV would have a missed digitizer self-trigger.

The SE-SPS was setup to have its opening aperture at 3° from the beam axis. The target-chamber aperture slits that opened into the spectrograph were opened horizontally to +/- 1.73° in order to allow for a sufficiently fine triton momentum resolution at the focal plane, without sacrificing too heavily on the triton flux that entered the SE-SPS. A wider horizontal entrance aperture into the SE-SPS would have led to more counts in the focal plane with poorer resolution between states, while a smaller entrance aperture than the one chosen ran the risk of not collecting sufficient statistics within the experiment runtime. This constraint was, however, not present when making the decision regarding the vertical entrance slits since the SE-SPS is oriented horizontally and with its momentum-selected tritons constrained to high precision to move along the horizontal plane. Hence, the vertical slits were opened to the maximum allowable value of +/- 2.19° i.e. 76.4 mrad. In sum, the entrance aperture to the SE-SPS from the target chamber spanned a solid angle of 4.62 msr. In order to bring to focus states in ^{31}S in the range $E_x = 6 - 8$ MeV, the magnetic field was set to a value of $B = 13.495$ kG. The ^{14}N data used a magnetic field setting of 9.68268 kG which placed the first proton unbound state with $E_x(^{14}N)$=7.967 MeV close to the center of the focal plane detector.

The focal plane detector was filled with isobutane gas to a pressure of 170 Torr using the adjacent gas-handling system. Both pairs of anode wires in the focal plane detector were

Table 3.1. Leakage currents observed in each MMM segment of SABRE during the experiment. Care was taken to keep a close eye on these numbers during the course of the run, so as to avoid recording data in the event of sudden fluctuations.

SABRE Detector ID	Leakage current (μA)	
	at experiment start	at experiment end
1	1.53	2.29
2	1.52	2.84
3	1.36	1.90
4	1.45	2.10
5	1.28	1.80

positively biased to +1600 V, and the cathode plate at the bottom was biased negatively to -700 V. The scintillator PMTs were biased at -1800 V.

All 5 MMM detectors in SABRE were biased to a voltage of -60 V during the experiment, and the reverse leakage currents in each of the detectors were monitored closely during the course of the experiment, so as to avoid any large changes to the physical properties of the depeletion region arising from the beam scattering due to the beam moving out of focus, or hitting a neighbouring component such as the target frame. When the leakage current showed large increases, the beam was stopped and fine-tuned - and SABRE leakage currents were allowed to return to the nominal values before resuming data acquisition. Table 3.1 lists the leakage currents seen by each of the SABRE detectors before and after the experiment.

The ^{31}S measurement originally planned on utilizing a thinner (20 μg/cm^2) $^{28}SiO_2$ target that had been enriched to more than 99% in ^{28}Si (this target shall heretofore be referred to as the 'thin Si' target). However, during the course of the experiment this target proved too fragile to withstand the vacuum cycling performed to insert SABRE into the target chamber. Nevertheless, roughly 30 hours of data was gathered on the thin Si target that only recorded focalplane tritons at a slightly different magnetic field (B = 13.770 kG) compared to the thick Si target data, which shifted the visible peaks to the left by a few channels. This offset

was corrected during data analysis so as to align the two spectra prior to comparing their structures. This proved very useful in both gauging the degree of carbon contamination present in the thick Si target, as well as in cross-checking the structure of peaks that were observed in the ^{28}Si(^{6}Li,t)^{31}S reaction during studies with either target. Data using the thick Si target were collected for a total 105.7 hours of ^{6}Li beam on target along with the detection of decay protons in SABRE. Beam on target for the ^{14}N measurement was undertaken for a period of 2.12 hours which, though considerably shorter than the extent of data acquisition in ^{31}S, ensured sufficient statistics were gathered. This was because of the much larger cross section observed in the ^{12}C(^{6}Li,α)^{14}N reaction in comparison to the ^{28}Si(^{6}Li,t)^{31}S transfer. Lastly, some data was also gathered on the ^{12}C target under the same field settings as the ^{31}S (B = 13.495 kG), in order to better identify contamination effects due to the built up carbon in the thick Si target and record positions of known states populated in ^{12}C(^{6}Li,d)^{16}O for calibration.

3.1. Data Acquisition with CoMPASS, and Event Building

All 8 of the CAEN 1725 digitizers running DPP-PHA firmware connected to SABRE, and the CAEN 1730 digitizer running the DPP-PSD firmware connected to the focal plane detector were interlinked via daisy chains to record data using CAEN's proprietary software CoMPASS. The data-acquisition computer connected to the digitizers via CAEN's fiber-optic PCIe bridge A3818. The four parallel fiber-optic links were distributed to different sections of the digitizer daisy-chain in order to evenly distribute the data throughput seen by each link.

CoMPASS allows the user to have a single GUI interface to manipulate all the FPGA parameters on the digitizer chain, and receives recorded hits by digitizers in the form of event structures that contain the following information: the board index (referred to as 'Board'), the channel index within the board ('Channel'), the timestamp of event detection in units of picoseconds ('Timestamp'), the energy recorded by the ADC ('Energy'), and a 32-bit flag

register ('Flag') that identifies any internal errors/warnings that might be associated with the recorded event, such as a pile-up. The DPP-PSD firmware also records the integral of the signal across the short gate as 'EnergyShort'.

The Timestamp parameter in DPP-PHA increments in units of 4 ns, in keeping with the design of the CAEN 1725 digitizers running this firmware. The timestamp parameter in the v1730 digitizer running DPP-PSD uses the digital Constant-Fraction Discriminator(CFD) to determine the event self-trigger, which extracts additional precision (down to 2 ps) in the reported timestamp by interpolating between the samples nearest to the CFD signals' zero-crossing. This capability of the 1730 digitizer plays a significant role in making the digitized focal-plane system viable. Data from CoMPASS can be saved to the hard-disk in either binary format, comma-separated variables, or as ROOT trees. In the interest of maximizing processing power spent on data-acquisition, this experiment saved all data in binary format, which allowed us to circumvent system overheads from additional computation required by the other formats. In addition, all data were recorded during the experiment to an NVMe Solid-state Hard Drive (Model: Seagate FireCuda 510 PCIe Gen3) that had been benchmarked to achieve large sequential read/write speeds. These precautions were taken over and above the use of FPGA coincidence logic to bring down the data-throughput rate seen by the part of the digitizer array recording signals from SABRE. Data acqusition was performed in intervals of 1 hour, each followed by a quick diagnostic evaluation of the recorded data to ascertain the quality of the focal-plane spectra, and the presence of a sensible number of coincidences in SABRE.

An important step involved in post-processing the recorded data to identify coincidences is to query it, and identify signals that are in time coincidence to each other, which correspond to different components of the same beam-on-target event recorded simultaneously across detectors. This process is commonly referred to as event building, and is performed in this case via the following steps:

- First, the scintillator signals and SABRE signals are time-shifted forward by about

1000 and 500 nanoseconds respectively, compared to signals from all the other detectors. This offset was arrived at empirically by comparing observations in many experiments that preceded the current one, and is required to appropriately 'center' the fast scintillator/SABRE signals with respect to all the other recorded signals that are expected in coincidence with them. The physical reason behind this offset is the extremely fast time response of plastic scintillators and semiconductor detectors to the charged particle causing the self-trigger, in comparison to the slower time-scales in other detectors caused by gas ionization, drifts, avalanches, and delay-lines.

- Next, the time-shifted signals are analyzed in software, and data structures are formed for events that are within a trial time window τ_{eb} of the others. τ_{eb} is commonly referred to as the eventbuilding time window, and is characterized by the slowest timescale in the apparatus that cannot be corrected for by offsets - typically, this is set by the delay-line signals from either end. A suitably ubiquitous signal such as the anode readout from one of the back wires ('anodeBack'), is used as a mandatory readout to consider an group of coincident signals an 'event'. Detecting the back anode means that the only other potential region for the particle to be stopped is in the exit mylar window of the focalplane, which is very unlikely. (A time window of $\tau_{eb} = 8\mu s$ or above was found to be sufficient as a starting estimate, which was then lowered in steps subsequently to obtain a sharp selection of time-correlated events along with a background region just wide enough to provide an estimate of random coincidences in the system).

- At the end of each of the iterations above, histograms are plotted of time differences between various signal groups and relative time offsets between channels and the width τ_{eb} of the eventbuilding window are varied until there are no features present in the histograms that are cut off by the edges of the eventbuilding window. At this stage, the data are grouped into new data structures that possess names better suited for plotting, and saved into ROOT files called the 'analyzed' ROOT Trees.

- The last, and final stage of eventbuilding, involves reading the shifted, analyzed, ROOT files, forming particle-identification gates in suitably selected channels, and where relevant, improving the time-coincidence precision by setting up tighter timing gates to reduce background counts. In our case, these fine-time coincidences are set up in all SABRE channels as will be described in detail in subsequent sections.

- The coincidence window used in eventbuilding all data was fixed at $\tau_{eb} = 2.0\mu$s, with any further reduction of background accomplished by setting up additional gates during further analysis.

The next subsection will describe the steps undertaken to perform particle identification and generate the focal-plane triton and alpha spectra of relevance to the ^{31}S and ^{14}N measurements, respectively.

3.2. Focal-plane Analysis, Calibration and Particle Identification

As discussed before, the two sets of delay lines at the front and back of the focal plane detector detect the position of the particle along two parallel planes at the exit of the spectrograph, both lines lying near the focal plane of the SE-SPS. In either delay line, the position of the detected particle is calculated by subtracting the timestamps of the signals detected on the low-rigidity side of the focal plane detector from that detected on the high-rigidity side, and dividing the result by two. This value is converted to the position in millimeters by utilizing the measured average delay per chip on either side, which yields a conversion factor of 0.476 mm/ns on the back plane, and 0.505 mm/ns on the front plane.

To identify events that have a correlated position between the two planes, we plot a histogram between the front-plane position and the back-plane position. This histogram was used to identify and eliminate all the events that have one or the other side firing on noise in the detector. Figure 3.1 shows this cut applied to both the ^{14}N and the ^{31}S data.

Following this selection of good events that have correlated signals between both the

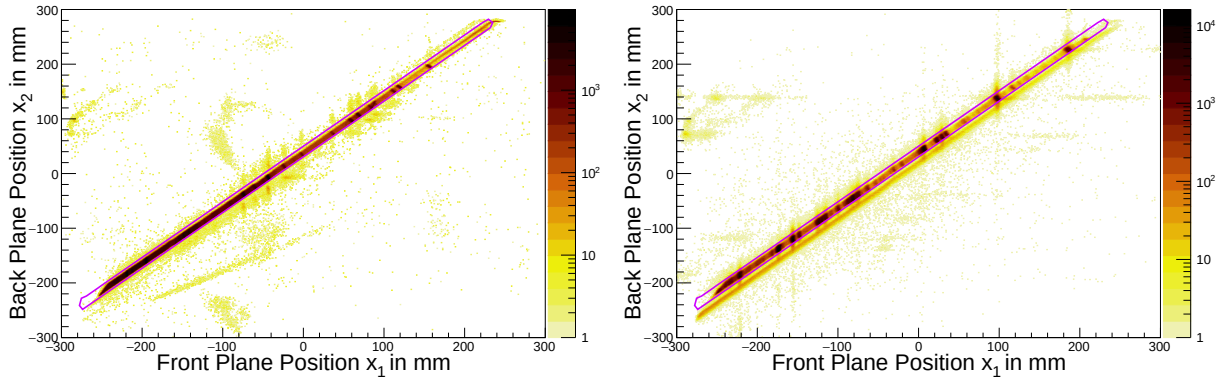

Figure 3.1. Two dimensional histograms plotting the front and back positions recorded in all the analyzed, eventbuilt events from the ^{14}N dataset (left) and the ^{31}S dataset (right). The pink enclosed curve represents the graphical cut — all the events that are inside the cut are selected for further analysis. The ^{31}S dataset shows more prominent detector artifacts, likely arising from the much longer duration of data gathered in this dataset.

front and back planes in the focal plane detector, we use coordinates x_1 and x_2 along both of these loci to generate the position of the detected particle along the real focal plane, which is the locus with the best focus of detected particles for a chosen reaction of interest. Details of this operation are discussed in Appendix A. This also requires us to identify events arising from only the particles of interest in a given reaction — specifically, α particles arising from ^{12}C(^{6}Li,α), and tritons arising from ^{28}Si(^{6}Li,t). In order to do this particle identification, we plot histograms between a suitably selected Energy-loss (ΔE) signal from one of the components of the gas-ionization chamber in the focal plane detector, and the residual energy signal (E) recorded by the scintillator. It has been observed empirically during several previous measurements [68, 76] that plotting the focal-plane position against energy-loss ΔE signals is also very useful towards grouping detected particles by their mass and charge, as discussed in Eq 2.3. We select the anode energy signal detected in the back-plane as the reference ΔE signal, and plot it against the left scintillator signal and the focal-plane position x_{avg} calculated from x_1 and x_2 to obtain the plots shown in Fig. 3.2. We choose the left scintillator in particular since the focal plane detector is oriented closer to the left of the scintillator bar, which increases the likelihood of light output on the left

side to be from signals arising from particles that exit the ionization chamber.

Having plotted ΔE versus E signals, as well as ΔE versus focal-plane position signals, we first draw a particle-identification gate in the ΔE vs E histogram guided by both histograms. This is our initial particle-identification cut - we identify particle groups from their expected positions in ΔE vs E as well as the structure of the position spectrum seen in ΔE vs x_{avg} histograms. By plotting the ΔE vs x_{avg} histogram after the ΔE vs E gate has been applied, we perform finer particle selection by gating out features from other particle groups that leak into the position-independent ΔE vs E graphical cut. Combining both of these gates, we obtain the full position spectrum of observed α particles in the ^{14}N reaction, and tritons arising from the ^{31}S reaction as shown in Figs. 3.3c and 3.3d. Every peak in these spectra corresponds to a populated excited state in the heavy nucleus (^{14}N, ^{31}S or a contaminant) that is created in the reaction. The next subsection discusses the calibration process of the focal plane detector that relates the focal-plane position x_{avg} detected to the ρ parameter of the SE-SPS and the excitation-energy E_x of the populated nucleus.

3.2.1. Focal-plane Position Calibration

Having identified particles and their positions along the focal plane, we calibrate the focal-plane position against the particle-trajectory radius ρ described in Section 2.2. The calibration is performed using the analysis code Split Pole ANalysis Code (SPANC) [100] that takes as its input observed position centroids and excitation energies for peaks corresponding to well known states in reactions to identify a polynomial relationship between the measured position x_{avg} and the radius parameter ρ. As long as the type and energy of the detected particles in the focal plane detector can be well identified, the radius parameter ρ can be calculated for focal plane peaks populated by any reaction, including ones that are not directly under study.

To perform calibrations for our present experiments, known states in the reactions ^{12}C(^{6}Li,d)^{16}O (E$_x$ = 0.0, 6.049 and 8.872 MeV), ^{16}O(^{6}Li,d)^{20}Ne (E$_x$ = 0.0, 1.634, 5.621,

5.788 and 6.725 MeV) and ^{28}Si(^{6}Li,d)^{32}S (E_x = 2.231, 3.778 and 5.006, 5.796 MeV) that were selected via the deuteron particle groups shown in Fig. 3.2 were used. A third-order calibration polynomial was able to fit the ρ values calculated by SPANC to a p-value of 0.954 at a position resolution of 0.4 mm for each peak included. This calibration process provided us with a direct one-to-one relation between the observed focal-plane position x_{avg} and the excitation-energy of the populated nucleus in each reaction. Figures 3.4 and 3.5 show the result of applying the calibration to the focal-plane position, and label several known resonances in ^{14}N and ^{31}S. The presence of non-linear corrections arising from detector artifacts was noted during the calibration, and have been accounted for in subsequent analysis as a systematic error in the reported excitation energies.

3.3. SABRE: Calibration and Analysis

After satisfactorily calibrating the focal-plane position against the excitation-energy spectra of the nuclei of interest as described in the previous subsection, we now include coincident proton-decay information captured in SABRE from all the states populated in the heavy reaction product with excitation energies E_x lying above their proton thresholds S_p. The first step to incorporate the data from SABRE into the analysis, is to individually gain-match each channel in SABRE so as to obtain a clear relationship between the energy deposited by particles in SABRE and the ADC readout from each digitizer channel. To accomplish this, we use the approach described in detail by Reese *et al.* [101] by utilizing internal correlations between all coincident energy signals detected on the junction- and ohmic-sides of a silicon detector. The central logic to this mode of analysis is the recognition that semiconductor detectors work by the release of free electron-hole pairs in the depeletion region of a PN-junction in reverse-bias, the number of pairs being proportional to the energy lost by the charged particle detected within the region. In addition, energy signals detected in the majority of coincident events in SABRE have the most charge collection observed between a single segment on either side of the MMM detector, localizing the particle's coordinates to

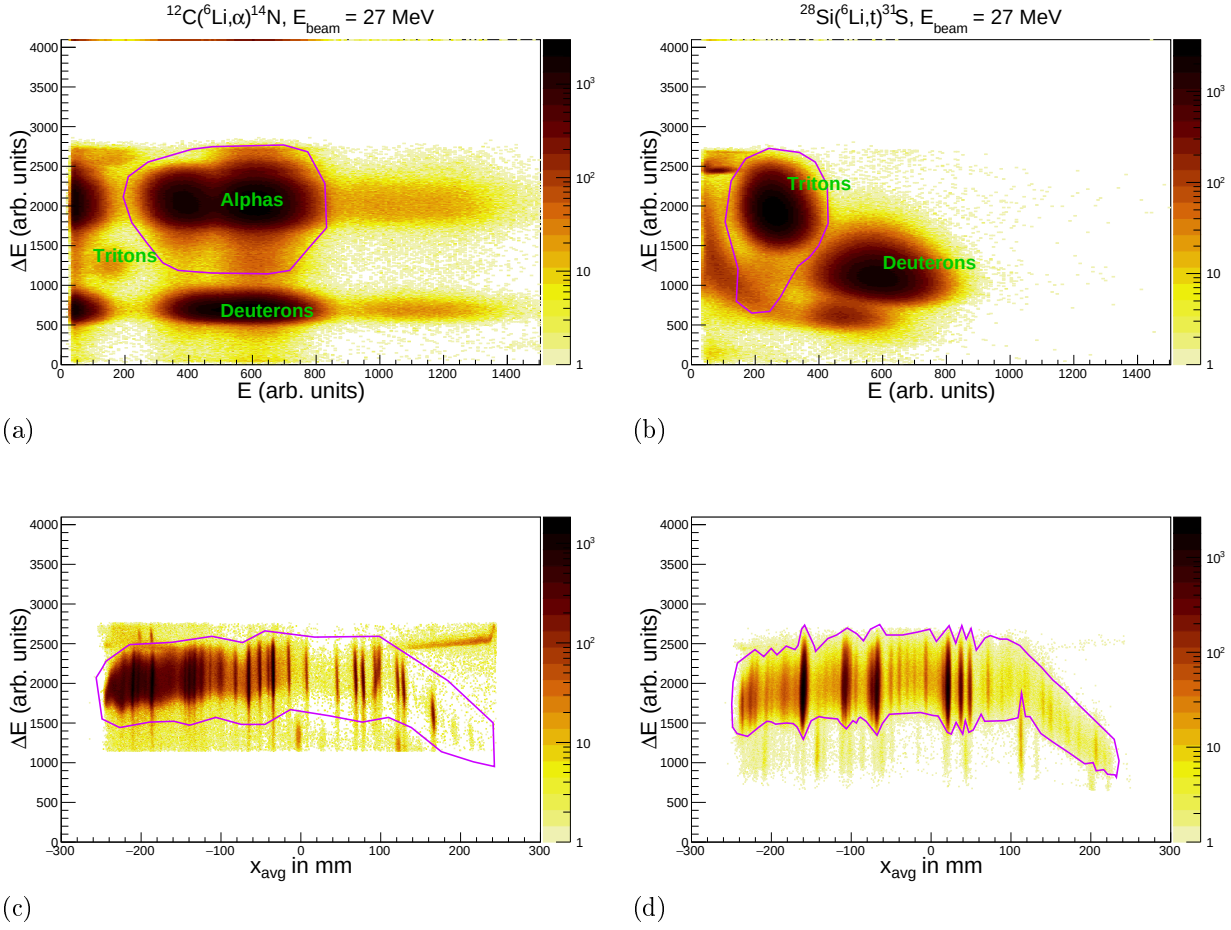

Figure 3.2. Histograms showing the use of energy-loss (ΔE), residual energy (E) and focal-plane position x_{avg} signals to perform particle identification in the focal plane detector. All the plots in the left column are from the ^{12}C(^{6}Li,α)^{14}N reaction dataset, while those in the right column are from the ^{28}Si(^{6}Li,t)^{31}S reaction dataset. Graphical cuts used are shown in magenta. Histograms (a) and (b) show the ΔE and E signals arising from the ionization chamber back anode, and the left scintillator, respectively, broadly identifying different particle groups. Histograms (c) and (d) plot the ΔE signal against the focal-plane position after broad particle-identification gates are placed in (a) and (b). The graphical cuts in (c) and (d) eliminate leaked events from other reaction channels.

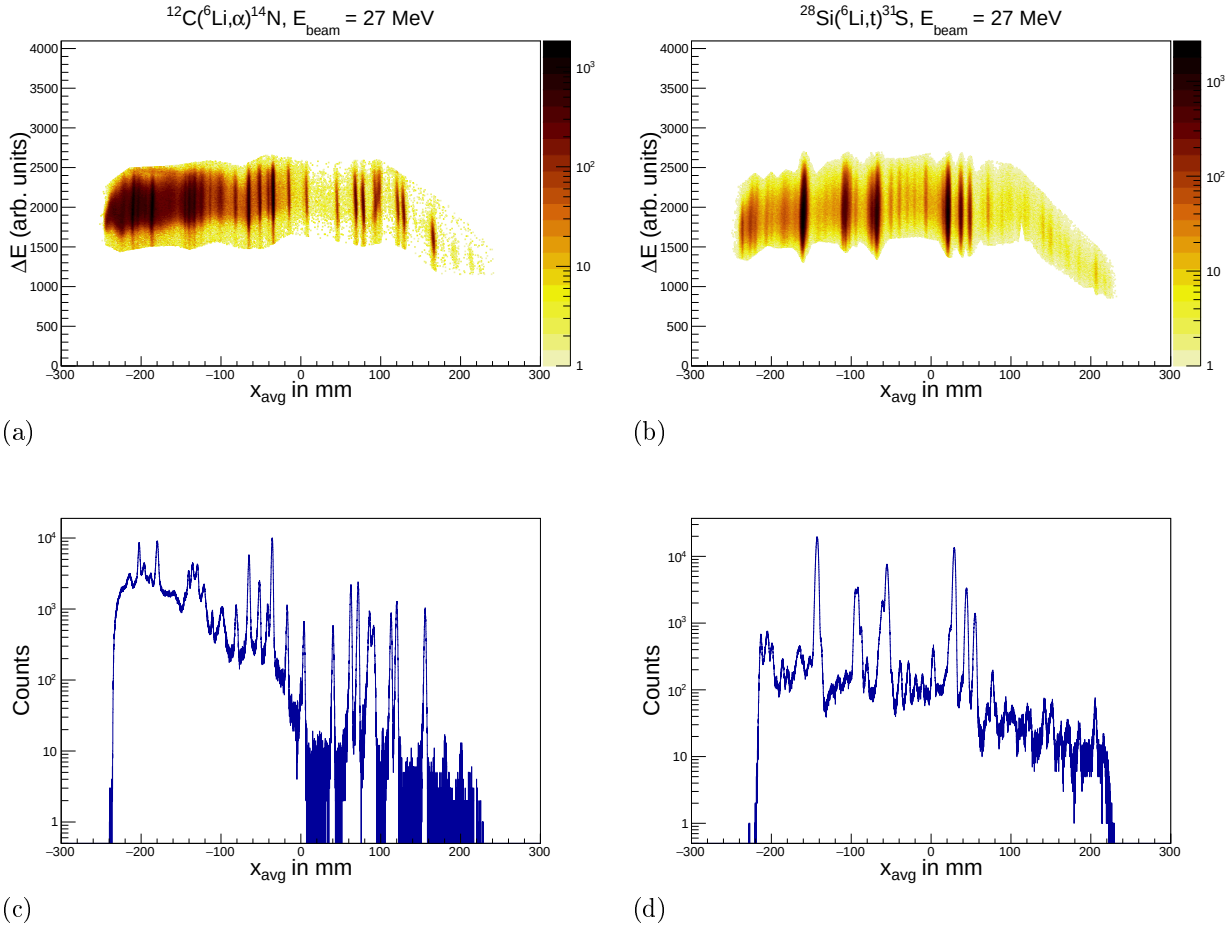

Figure 3.3. Histograms (a) and (b) plot the ΔE signal against the focal-plane position after all the particle identification gates from Fig. 3.2 have been applied. Histograms (c) and (d) represent the projection of (a) and (b), respectively, onto their x-axis, plotting the 1D focal-plane position histograms for all α particles detected in the ^{12}C(^{6}Li,α)^{14}N reaction (left) and all tritons detected in the ^{28}Si(^{6}Li,t)^{31}S reaction (right).

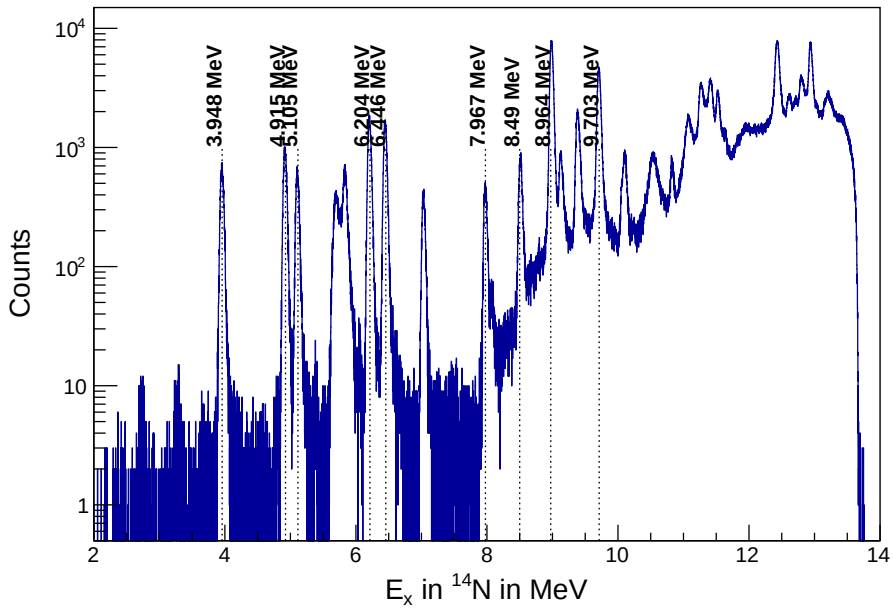

Figure 3.4. Calibrated focal-plane position histogram for the ^{12}C(^{6}Li,α)^{14}N reaction, labeling a few known states in ^{14}N.

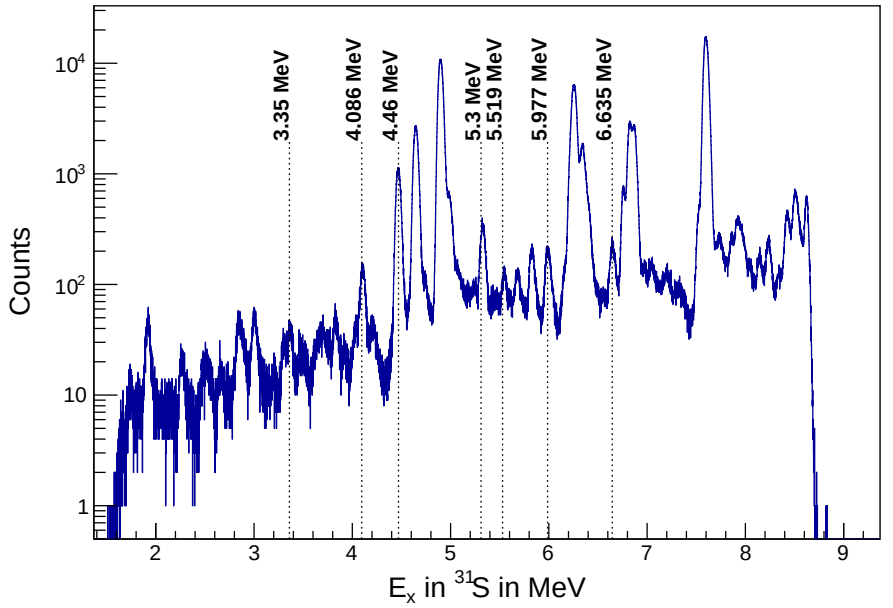

Figure 3.5. Calibrated focal-plane position histogram for the ^{28}Si(^{6}Li,t)^{31}S reaction, labeling a few known states in ^{31}S.

the angular element corresponding to their intersection.

The number of new electron-hole pairs generated by the incoming charged-particle's interaction with the depeletion layer will be equal, and will create a correlation between the charge-collection observed by the preamplifiers wired to channels on each side, and the signal size sent to the corresponding digitizer channels. If one now looks through a large dataset of the detector subjected to a measurement and identifies all correlated events that have only one channel firing on either side - one could generate experimentally, the unknown correlations S_{ij} between energy signals detected by every pair *(i,j)* of detector segments on the two sides. Reese *et al.* [101] demonstrate how this correlation matrix S_{ij} could then be unwrapped to calculate the scale factors s_i corresponding to every channel that satisfies

$$E = s_i A_i \tag{3.1}$$

where $i = 0$ to 15 for the 16 MMM segments on the junction side ('rings'), and $i = 0$ to 7 for the 8 MMM segments on the ohmic side ('wedges'). E is the true value of the detected energy in keV, A_i is the raw uncalibrated energy value output by the digitizer channel processing signals from the element. Correlations S_{ij} satisfy

$$S_{ij} = s_i / s_j \tag{3.2}$$

If correlations S_{ij} are found with uncertainties ΔS_{ij} for every ring-wedge pair i, j in a detector, the individual factors s_i and s_j could be now found by arbitrarily fixing one of the 24 per the MMM (say $s_{i=0}$ for the 0th ring), and minimizing χ^2 expressed as

$$\chi^2 = \sum_{i,j} \left(\frac{S_{ij} - \frac{s_i}{s_j}}{\Delta S_{ij}} \right) \tag{3.3}$$

This leads to a calibration for all channels in a single MMM detector segment of SABRE that depends on the fixed value chosen for the selected segment. To convert these calibration constants s_i to those that convert the detected ADC readouts A_i to a physical unit like keV,

we utilize a radioactive source with known properties for its decay byproducts. In our case, we use an ^{241}Am source to scale all the calculated constants to the correct energy by detecting the α-particle decay line with $E = 5.486$ MeV. Specifically, the innermost rings in SABRE were fixed to 1.0 when minimizing the χ^2 function, and then scaled by a constant value κ so as to have the calibrated energy value to be 5486 keV. The innermost rings are expected to have detected α particles with the least energy loss from their passage through the source, since the radioactive source is placed at the same point as the beamspot during an experiment run. Figure 3.6 illustrates the progression of signals measured by SABRE ring channels at each progressive step of the internal gain-matching algorithm. The interested reader is referred to the original reference for more details [101]. The calibration factors s_i were observed to not show large changes over time. Figures 3.6c, 3.6d calibrate ^{241}Am α-decay data using factors s_i calculated using SABRE data gathered over 48 hours later. Small fluctuations caused by the use of time-shifted factors s_i this way are visible in these plots, over and above the systematic shift in energy resolution over channels seen due to the polar-angle dependent energy loss in the target experienced by the α particles.

The other important step after gainmatching energy signals, is to select events in SABRE that have the closest time correlation with light particles detected at the focal plane — α particles for the ^{14}N measurement, tritons for the ^{31}S measurement. This is accomplished in two steps: First, we repeat the eventbuilding process over many iterations, while adding variable offsets in each iteration to the detection timestamp of every SABRE channel with respect to the scintillator validation trigger, until the relative time offsets are most aligned and close to zero. This leads to a very prominent $\Delta t = 0$ correlation pattern, as shown in Fig. 3.7. Second, we use a graphical cut to select only those events within the central correlation pattern as coincident particle-decay events that arise from the transfer reaction of interest. Eventbuilding is typically performed over a slightly larger time window than the width of the correlation gate used, because the region of the time-difference spectrum between SABRE and the scintillator signals that is far removed from the central coincidence

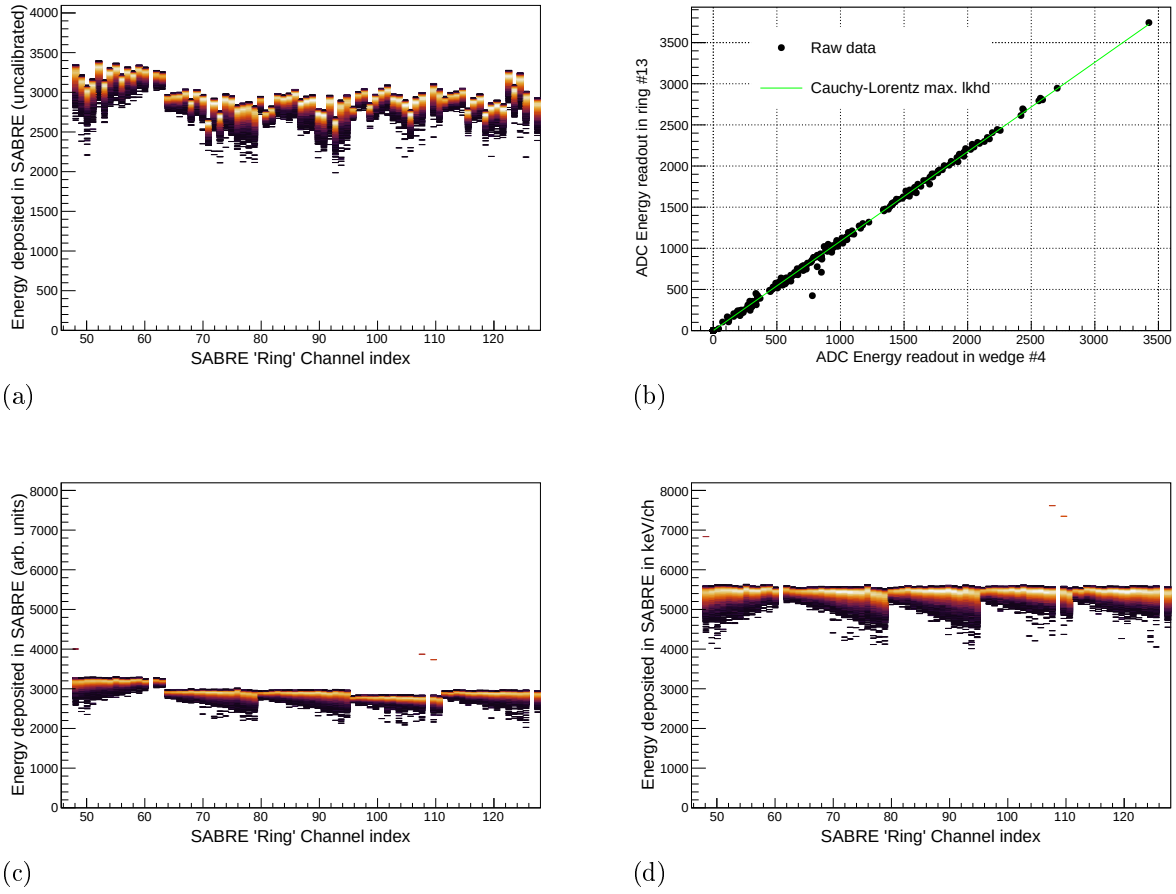

Figure 3.6. Stages in SABRE channels' internal energy calibration. All histograms only show the 80 junction-side 'ring' channels used in the present experiment (a) ^{241}Am data prior to calibration (b) Sample correlation between 'ring' i=13 and 'wedge' j=4 in MMM detector number 2, showing the extraction of S_{ij} using a Cauchy-Lorentz maximum-likelihood fit (c) ^{241}Am data shown in (a) but with only internal calibrations within each MMM detector applied (d) ^{241}Am data with both internal calibration and scaling to keV/ch applied using the knowledge that the ^{241}Am alpha decay spectrum peaks at an energy of 5486 keV. This results in the calibration applied to all subsequent data analysis that uses SABRE.

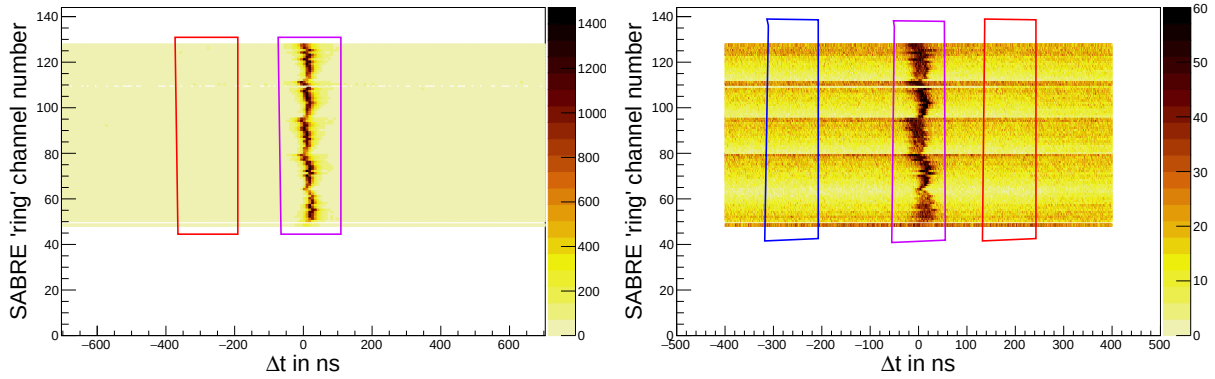

Figure 3.7. Two dimensional histograms plotting the arrival time difference (x-axis) between signals on 80 SABRE 'ring' channels and the focal-plane scintillator for the ^{14}N dataset (left) and the ^{31}S dataset (right). The y-axis in each histogram represents the index of a 'ring' channel in each bin. The pink graphical cut in the middle encloses all the coincident events detected. The red and blue gates are used to determine the random background coincidences.

pattern provides a very robust measure of the background counting rate in SABRE due to accidental/random overlaps encountered between the various logic signals that perform trigger validation. During the course of data analysis for our measurements, the random background encountered by SABRE signals for the ^{31}S measurement is calculated by averaging signals detected on both sides of the central coincidence pattern, using graphical cuts of the same size as the central cut but offset in position in either direction (see Fig. 3.7.) The backgrounds arising in the ^{14}N measurement were estimated using only one side of the central coincidence pattern, since the large trigger rates recorded in the scintillator caused some correlated events to leak in the other direction.

After both the above steps, it is now of interest to plot the excitation energy of the heavy nucleus that undergoes decay (i.e. the calibrated focal-plane position spectrum), against the calibrated energy deposited due to the coincident charged-particle events in SABRE. There is a strong correlation observed in these 2D histograms, with states above the charged-particle emission thresholds showing coincident peaks that increase in energy deposited in SABRE as they go towards higher excitation energies — as one would expect due to energy conservation (see Fig. 3.8). Another feature of interest that is visible in the ^{31}S dataset, is a second set of

correlated counts parallel to the gated feature, at lower SABRE energies. These correspond to protons detected in SABRE from decays to excited states in ^{30}P - the first two of which are not resolved because decays from a given excited state in ^{31}S state to either of these ^{30}P excited states are expected to be only 30 keV apart in energy. (Note: A measurement capable of detecting the γ-ray decays from these states in coincidence with the protons could in principle differentiate them, but this was not performed in this experiment.) Decays to the third excited state in ^{30}P were clearly resolved from those to both the ground state and the first two excited states.

Gating around these diagonal features in the E_x versus SABRE energy histograms finally gives us all the focal-plane events that were detected with a coincident charged-particle (proton) decay. These gates will also include some contribution from random background events, but it is possible to account for their presence by using the gates away from the central coincidence pattern shown in Fig. 3.7. The resulting background has the structure shown in Fig. 3.8 (c) and (d) with a large contribution of background events caused by high cross-section (^{6}Li,t) transfer reactions on ^{12}C and ^{16}O. These populate states that are particle bound, but since they cause so many scintillator validation triggers to emerge correlated with them, also cause a more significant number of random correlations with SABRE events — the randomness of their correlation being borne out in there being no SABRE energy dependence seen for these states, which show up as nearly uniform vertical lines in the 2D histograms (Fig. 3.8(b) and (d)). During the analysis to calculate branching ratios, we subtract this random background from the observed coincident events, as will be discussed in the subsequent section.

3.4. Angular Distributions: Spin Assignments and Branching Ratio Measurements

Now we have constructed two sets of events, as depicted in the one-dimensional histograms in Figs. 3.9 and 3.10. These are focal-plane events detected from all tritons and α particles

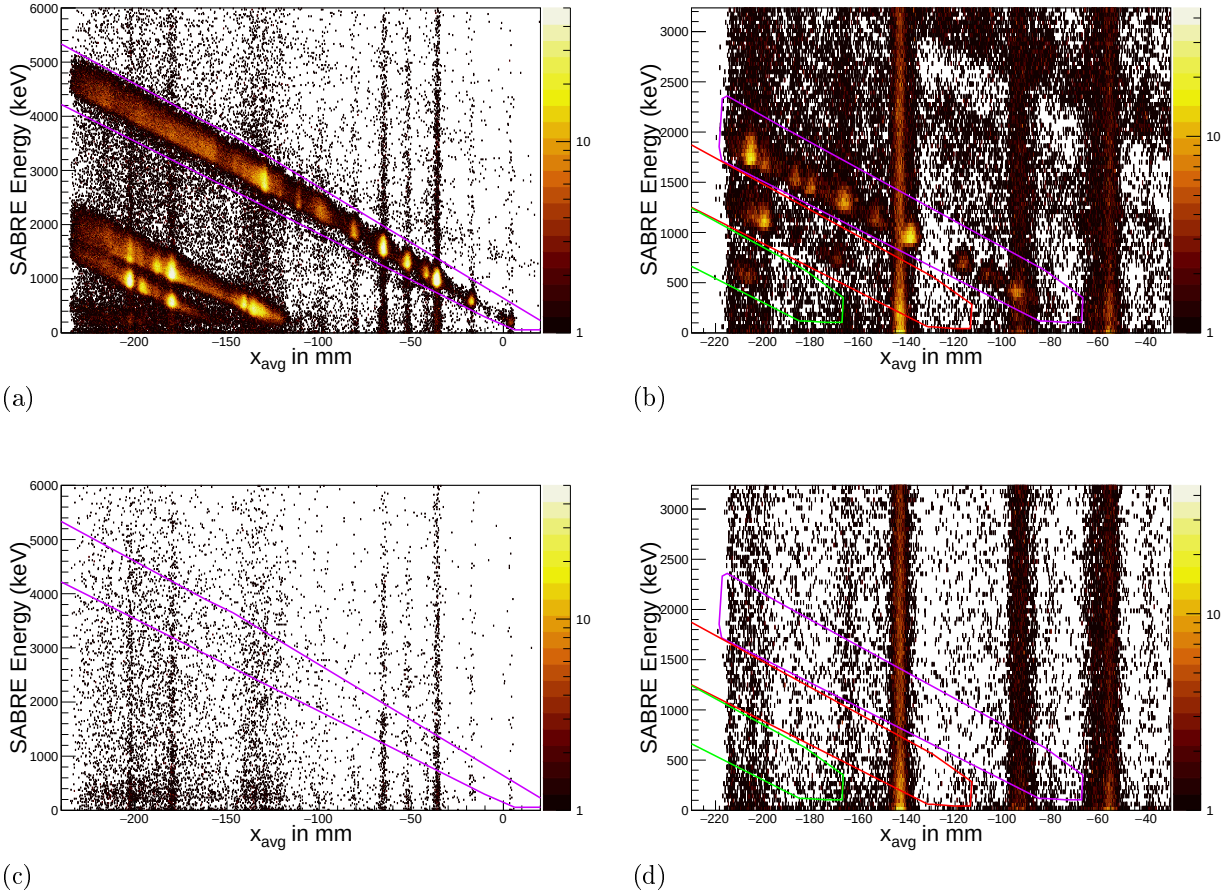

Figure 3.8. Plots showing energy deposited in SABRE by coincident decay protons against their focal-plane position. The gated events in (a) and (b) correspond to the decay $^{14}\mathrm{N}^{*} \rightarrow {}^{13}\mathrm{C} + \mathrm{p}$ and $^{31}\mathrm{S}^{*} \rightarrow {}^{30}\mathrm{P}^{g,1+2,3} + \mathrm{p}$, respectively. For (b) the violet, red, and green gates represent decays to the ground state, the pair of the first two excited states, and the third excited state in $^{30}\mathrm{P}$, respectively. Histograms (c) and (d) show the same information as in (a) and (b), respectively, but with the timing correlation gates in Fig. 3.7 moved away from the central coincidence pattern, representing the background count rate arising due to correlations between random backgrounds seen by the scintillator and SABRE.

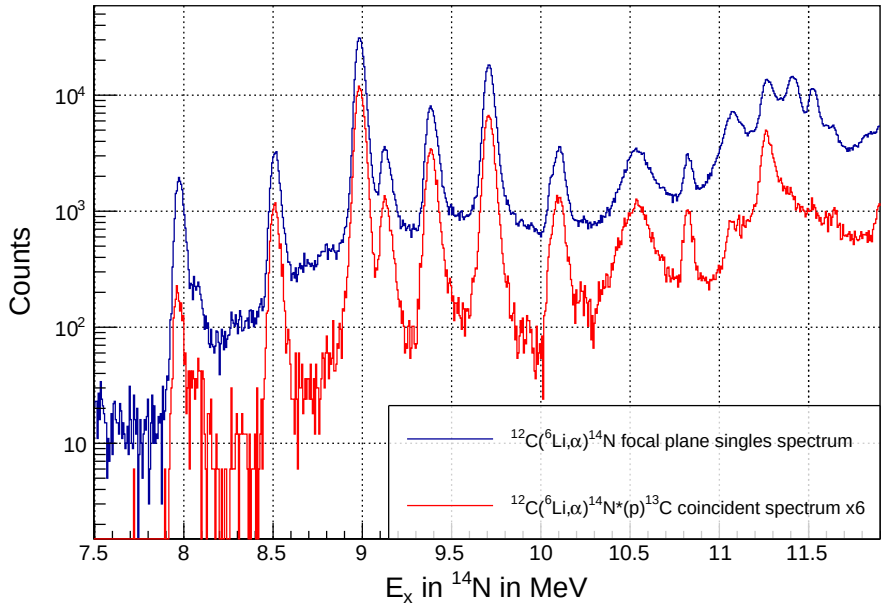

Figure 3.9. Calibrated focal-plane singles spectrum for the ^{12}C(^{6}Li,α)^{14}N^{*13}(p)C^g reaction (blue) zoomed in on the region of interest, along with the background-subtracted coincident spectrum (red), scaled up by a factor of 6. Several of the peaks correspond to states in ^{14}N with known proton-branching ratios, many of them having $\Gamma_p/\Gamma \approx 100\%$.

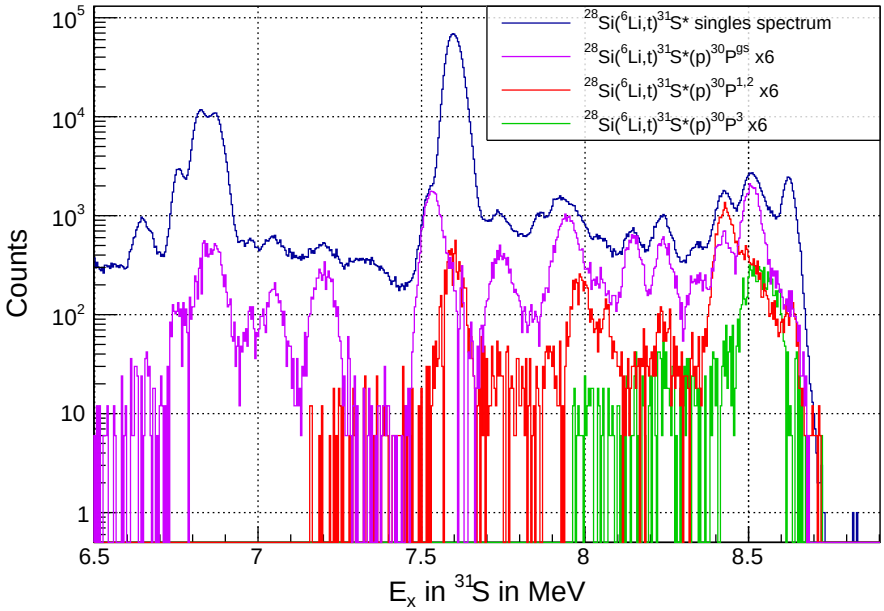

Figure 3.10. Calibrated focal-plane singles spectrum for the ^{28}Si(^{6}Li,t)^{31}S^{*30}P$^{g,1+2,3}$ reaction (blue) zoomed in on the region of interest. Also shown is the background-subtracted coincident spectrum representing decays to the ground state (violet), first- and second-excited states (red), and the third-excited state (green) of ^{30}P — all scaled up by a factor of 6.

arising from states in ^{31}S and ^{14}N in the respective datasets plotted in blue, which shall be referred to as the 'singles' histograms. A subset of these events also have coincident proton emissions detected in SABRE that can be differentiated from random backgrounds in aggregate, which are shown by the other histograms. Every peak in these histograms corresponds to events from a particular excited state in ^{31}S and ^{14}N as indicated by the focal-plane calibration. These shall be referred to as 'coincident histograms' for decay to the ground/n$^{\text{th}}$ excited states in ^{13}C and ^{30}P from here on.

The first step in investigating these states to determine their properties, is to fit these peaks with suitably chosen profiles that can allow us to differentiate between peaks that are not resolved by the focal plane detector where necessary. In the case of the ^{14}N dataset, a modified form of the Crystal Ball function [102] suggested in reference [103] was found to fit several of the higher statistics singles peaks well. In the case of the ^{31}S data, simple Gaussian profiles were chosen for each state studied in order to keep the parameter space more tractable. The resolution observed in the singles spectrum ($\approx$ 50keV FWHM) was not fine enough to permit its use as the primary identifier of resonances observed - the 'coincident' spectrum was hence used to separate and identify features in the singles spectrum. The present analysis has a persistent source of uncertainty in potentially missing unresolved states in the singles spectra that lead to no statistically significant number of proton decays detectable by SABRE.

For the singles histograms, we also must account for effects that arise due to the presence of background counts, determined by modeling the background as a linear, quadratic or broad peak. In order to keep the size of the parameter space low, the focal plane was divided into domains to analyze a single group of peaks at a time, taking care to match their boundaries for continuity by suitably adding peaks outside the domain with parameters fixed from their best-fit results in the neighboring domain. In any given domain, the fit function $f(x)$ could be modeled as

$$f(x) = \sum_{i=1}^{N} F_i(\vec{\sigma}; x) + F_b(x) \tag{3.4}$$

where $F_i(\vec{\sigma}; x)$ is a Gaussian, or a modified Crystal ball function, and the sum is over the number of peaks in the fitted region. The vector of parameters is $\vec{\sigma} = (A, \mu, \sigma)$ for a Gaussian with mean μ, standard-deviation σ, and integral A. For a modified Crystal ball profile, there is $\vec{\sigma} = (A, \mu, \sigma, k)$ with the additional shape parameter k in each profile [103]. F_b(x) models the profile of the background, which is assumed to have a constant value in the case of analyzing singles data in the ^{31}S dataset. The value of the constant background was estimated from the number of counts recorded per position bin within the region $E_x(^{31}\mathrm{S}) = 7.35 - 7.45$ MeV where the reported level density is low. This estimated background was cross-checked between data recorded from both SiO_2 targets having different thicknesses, and was found to be in agreement. For the ^{14}N dataset, the background of the singles spectrum was assumed to have linear, quadratic, or broad Gaussian profiles as discussed before.

No background function was found necessary to fit the ^{31}S coincident histograms to achieve satisfactory fit qualities, while resonances with higher E_x values in ^{14}N were found to have background counts with well-identified profiles — similar to the singles spectrum. The entire range of SABRE's polar angle θ coverage, spread across 16 junction side strips, was subdivided into 8 (or 4) angular bins consisting of counts combined from 2 (4) successive strips each, and 8 (4) different coincident histograms were created that plotted focal-plane spectra having coincident SABRE counts detected within the particular angular bin.

The contribution $P(i)$ arising from the i-th peak to the total counts observed in each position domain, was calculated as

$$P(i) = \frac{A_i}{A_w} N_c \tag{3.5}$$

where A_w is the integral of $f(x)$ in the whole domain, A_i the integral of the i-th peak, and

N_c is the total histogram counts within the domain. (Appendix B evaluates the integral of the modified Crystal Ball function in terms of all the other parameters.) This procedure is undertaken to systematically estimate the contribution from each state and from the background feature within a multi-peak structure composed of several unresolved resonances. Calculating the contribution in all 9 cases — P_S for the singles histogram, and $P(i)$ for the eight coincident histograms corresponding to each SABRE angular bin — allows us to now determine the angular correlation parameter $W(\theta)$ for the n^{th} angular bin [67, 76, 87, 104] as

$$W(\theta)_n = \frac{P_n(i)}{P_S d\Omega} \tag{3.6}$$

where $d\Omega$ is the solid angle subtended by the n^{th} angular bin in the center-of-mass frame of the reaction. This quantity $d\Omega$ is calculated from a Monte Carlo simulation that accounts for the reaction kinematics and energy losses in the target for all the interacting particles. This simulation also allows us to identify the mean angular position of the various detector components in the reaction center-of-mass frame, which is used in plotting measured $W(\theta)$ as a function of θ. Uncertainty propagation is performed by assuming no correlations:

$$\sigma W(\theta)_n = W(\theta)_n \sqrt{\left(\frac{\sigma P_n(i)}{P_n(i)}\right)^2 + \left(\frac{\sigma P_S}{P_S}\right)^2 + \left(\frac{\sigma \Omega}{\Omega}\right)^2} \tag{3.7}$$

where the uncertainty in each peak contribution (using the notation P to represent either P_n or P_S) is found as

$$\sigma P = P \sqrt{\left(\frac{\sigma A_i}{A_i}\right)^2 + \left(\frac{\sigma A_w}{A_w}\right)^2 + \left(\frac{\sigma N_c}{N_c}\right)^2} \tag{3.8}$$

where errors σA_i and σA_w are found from the fit results varying them as parameters, σN_c is estimated as the square root of the total number of counts in the histogram within the position domain chosen, and $\sigma\Omega$ is estimated from the uncertainty observed in the Monte

Carlo simulation.

For unbound states in ^{14}N and ^{31}S that have well-defined spins, it is possible to directly relate the angular distribution of $W(\theta)$ to the orbital angular momentum L of the charged-particle (proton) decay as given below, the derivation of which is described in detail in [67]:

$$W(\theta) \approx |P_L(cos\theta)|^2 \tag{3.9}$$

Since the spins of both the byproducts of the decay are well known, obtaining constraints on the decay orbital angular momentum allows us to constrain the spin/parity information of the parent nucleus' excited state. An important assumption that must be true for the validity of this method, is that the light reaction product detected in the focal plane detector must be constrained to very forward polar angles θ. This assumption being met preserves the azimuthal symmetry of the problem, making $W(\theta)$ independent of the azimuthal angle ϕ (or equivalently, the magnetic spin substates M), and allows for the simple description of Eq 3.9 to be sufficiently accurate. This assumption is true in our case, as we have configured the SE-SPS to have its entrance window at $\theta = 3(2)^\circ$ in the lab frame.

The above relation can be used to calculate the charged-particle (proton) branching ratio of the state, by integrating the best-fit $W(\theta)$ over all space. Following the procedure adopted in similar previous studies, we expand equation 3.9 in the Legendre-polynomial basis, as

$$W(\theta) = \sum_{j=0,2,4,..2K} A_j P_j(cos\theta) \tag{3.10}$$

where only even terms are allowed for index j because of the symmetry of Eq. 3.9 under the transformation $\cos(\theta) \rightarrow -\cos(\theta)$ forcing odd orders of Legendre polynomials to have zero for their coefficient A_j. Fits are performed to the angular distribution of $W(\theta)$ using the general parametrization above in increasing values of K until a good fit is found for $K = K_{min}$. When choosing the best-fit $W(\theta)$ curve, care is also exercised to ensure its value stays positive in the entire angular range, within uncertainty. Matching terms of the same

order between Eqs. 3.9 and 3.10 then gives us $L = K_{min}/2$, while the relation

$$\int_{\text{all space}, L\neq 0} P_L(\theta) d\Omega = 0 \tag{3.11}$$

gives us the experimentally-measured value of the branching ratio ($\mathrm{B}_{x,m}$) for charged-particle 'x' decays as

$$\mathrm{B}_{x,m} = \int_{\text{all space}} W(\theta) d\Omega = 4\pi A_0 \tag{3.12}$$

which is equal to the true branching ratio (B_x) in the absence of dead-time effects and other experimental corrections. As discussed before, the existence of dead-times arising from various factors during the experiment may add a correction factor to the expression above, which is determined by measuring several well-known branching ratios to good precision under the same experimental conditions.

The scale factor calculated for measured states in ^{14}N was found to be in good agreement with the scale factor in the ^{31}S measurement, when three precisely determined ^{31}S branching ratios in the current measurement were cross-checked with two different prior measurements that used different transfer reactions to synthesize the excited states [29, 49]. The final measured proton-branching ratios B_p will have the form:

$$\mathrm{B}_p = \frac{\Gamma_p}{\Gamma} = C \times \mathrm{B}_{p,\mathrm{m}} \tag{3.13}$$

where the normalization factor C will be determined by comparison against previously measured states having well-constrained branching-ratios. Figure 3.11 shows the results of the above analysis performed on the $E_x = 9.388$ MeV state in ^{14}N. Details pertaining to this calculation and those done for other observed states in ^{14}N, as well as their utility in measuring the factor C and influence in measuring unknown branching ratios of ^{31}S will be discussed in the next chapter. The next chapter will also tabulate the spin-assignments and proton-branching ratios measured for all the observed excited states of ^{31}S, by studying their decays

to the ground state of ^{30}P in all cases, and and to excited states of ^{30}P where applicable.

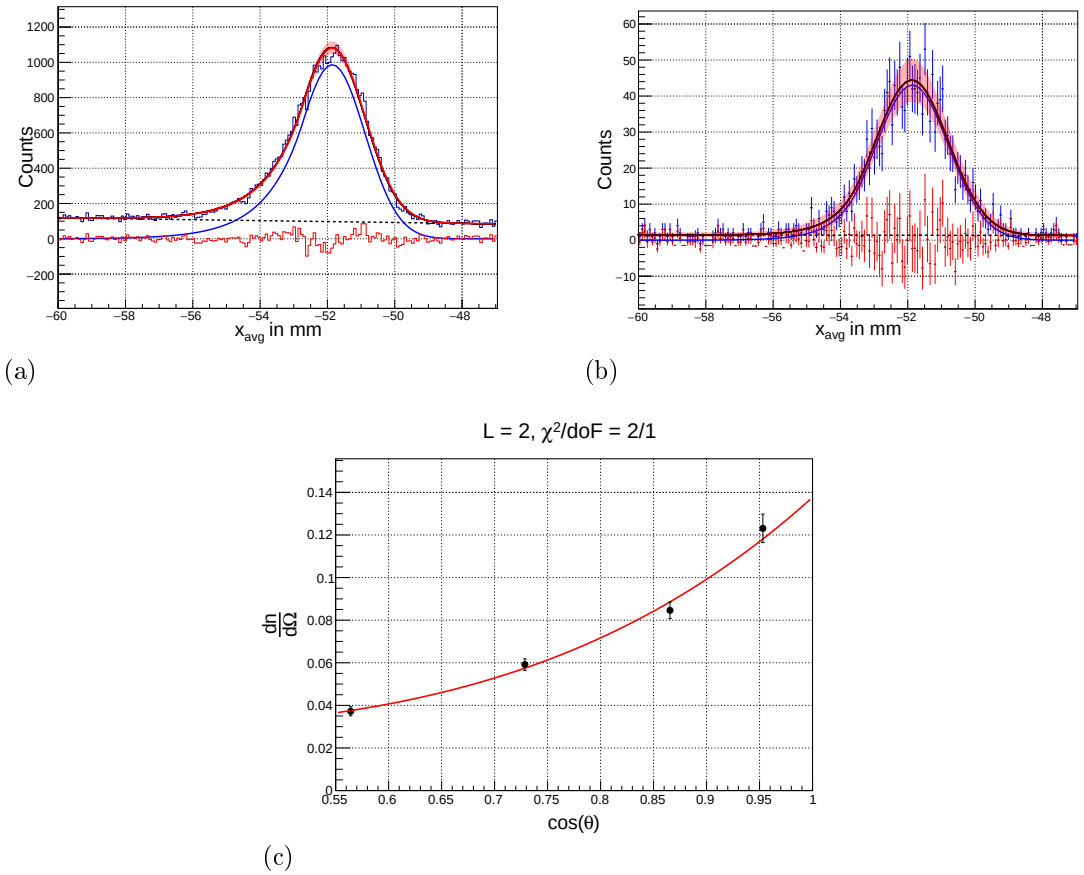

Figure 3.11. (a) Fits extracting peak contribution from the $E_x = 9.388$ MeV state in the ^{14}N singles histogram. The red histogram represents the fit residuals, and the dotted line represents the linear background function. The solid red shaded region represents the 95% confidence interval for the final fit curve. (b) Represents the same plot as (a) but made for focal-plane events coincident with a single angular bin in SABRE. (c) Shows the best-fit estimate of $W(\theta)$ using $\mathrm{K}_{min} = 4$ and $\mathrm{L} = 2$ over four angular bins, which yields the value $A_0 = 0.048(5)$ for the leading coefficient in Equation 3.10. The abbreviation '*doF*' is used to denote the number of degrees of freedom entering the fit. The subsequent chapter will discuss these results in greater detail.

Chapter 4. .Results

4.1. States Populated in ^{12}C(^{6}Li,α)^{14}N*(p)^{13}C

The preceding chapter discussed details of the framework adapted to extract spin-parity assignments and proton-branching ratios of resonances populated by transfer reactions and identified along with their coincident proton decays by the SE-SPS+SABRE system. This section describes the application of this method to the ^{12}C(^{6}Li,α)^{14}N*(p)^{13}C reaction measuring nuclear excited states in ^{14}N, the properties of which are well known in literature. We can identify the following resonances from Fig. 3.9, listed by their E_x values: 7.967 MeV, 8.065 MeV, 8.490 MeV, 8.960/8.980 MeV, 9.129 MeV, 9.388 MeV, 9.70 MeV, 10.101 MeV and 10.534 MeV. All of these states are proton unbound, since the proton theshold in ^{14}N is at $S_p = 7551$ keV [105]. In the interest of simplicity, we focus our attention on only the 9 resonances above, since at higher E_x values, other decay channels begin to participate - in particular, decays to the first-excited state in ^{13}C above $E_x(^{14}N) = 7.551 + 3.0894 \approx 10.640$ MeV.

When studying these resonances, the same procedure was adopted as described in the previous chapter. Spin-parity assignments and proton-branching ratio measurements were made under two different sets of assumptions to compare results. The first set assumed that the coincident histograms had no structured background that needed an explicit F_b function as part of its fit function, meaning that any background is determined from the coincident spectrum produced with the off-correlation gates applied (Fig. 3.7). Under the second set of assumptions, the same background functional form was used to fit the coincident histogram, as had been used to fit the singles histogram. The full set of 16 angular bins available in SABRE were combined to yield angular distributions with 4 and 8 bins as described previously. Unless the data warranted fits that used a term in the correlation value $W(\theta)$ larger than $L = 2$, all fits were performed by subdividing coincident histograms into 4 angular bins, so as to have larger statistics available within each bin. The correction factor C was

Table 4.1. Properties of ^{14}N states above the proton threshold, measured with the reaction ^{12}C(^{6}Li,α)^{14}N*(p)^{13}C. The evaluated uncertainties in the excitation energy include a uniform systematic uncertainty of 10 keV arising from non-linearities observed during detector calibration. The error-bars quoted in the branching-ratio measurements represent 1σ about the mean, and are quoted assuming a scale factor $C = 1.65(7)$ applied uniformly to all states as discussed in Section 3.4.

Index	$E_x(^{14}N)$ in keV		L^a	J^π		Branching ratio(Γ_p/Γ)	
	Lit [105]	This work		Lit [105]	This work	Lit [105]	This work
0	7966.9(5)	7976(10)	2	2^-	1^-,2^-,3^-	0.993(2)	0.74(0.19)
1	8062(10)	8052(15)	2	1^-	1^-,2^-,3^-	0.99947(12)	1.22(0.33)
2	8490(2)	8511(10)	1	4^-	0^+,1^+,2^+	0.79(8)	0.84(0.08)
3	8980(3)	8986(10)	2	$2^+/5^+$	1^-,2^-,3^-	unknown	0.97(0.08)
4	9129(5)	9128(11)	2	3^+	1^-,2^-,3^-	0.80(9)	0.66(0.12)
			3		2^+,3^+,4^+		0.70(0.31)
5	9388(3)	9379(12)	2	2^-	1^-,2^-,3^-	1.0	1.0(0.1)
6	9703(4)	9708(11)	2	1^+	1^-,2^-,3^-	0.9999959(10)	0.95(0.07)
7	10101(15)	10100(10)	1	2^+,1^+	0^+,1^+,2^+	0.999983(5)	0.97(0.09)
8	10534(20)	10540(11)	2	(1^-)	1^-,2^-,3^-	1.0	1.3(0.3)

[a] Assigned in this work

calculated separately for each state chosen, by dividing the expected B_p value reported in the literature with the observed $B_{p,m}$ values. The observed values of C were broadly consistent between different ^{14}N states, with a weighted average value of 1.65(0.07). This average was adopted as the overall correction factor for this reaction. Figure 4.4 (b) shows a comparison of measured B_p values with this average correction applied, against those previously measured in literature. The results assuming this average correction factor are also given in Table 4.1, and details for individual states are discussed below.

4.1.1. States at E_x = 7.967/8.062 MeV

The two resonances with E_x = 7.967/8.062 MeV are resolved within the resolution of the present experiment, and are important towards constraining the lower-energy threshold for proton detections in SABRE. In the center-of-mass frame, these states are 416 and 511 keV above the proton-emission threshold [$S_p(^{14}N)$ = 7.551 MeV], respectively. When accounting for energy-loss effects due to target thickness, the kinematics, and the angular spread in SABRE's segments using our Monte-Carlo simulation [87], decay protons from the E_x = 7.967 MeV state were expected to deposit lab-frame energies in the range 160-250 keV in SABRE, which made their detection challenging. This was also lower than the detection threshold for the lowermost resonance expected to be seen from the ^{31}S nucleus, as shown in Fig. 4.4(a).

As seen in Fig. 4.1, both these states strongly favor an L = 2 distribution, and a spin assignment of $J^\pi = 1^-$ to 3^-, which agrees with both their reported spin assignments [$J^\pi(E_x = 7.967 \text{ MeV}) = 2^-,\ J^\pi(E_x = 8.062 \text{ MeV}) = 1^-$] in the literature [105]. In addition, the observed proton-branching ratios also agree to within 1.5 standard deviations with the reported values of $B_p(E_x = 7.967 \text{ MeV}) = 99.3(2)\%$ and $B_p(E_x = 8.062 \text{ MeV}) = 99.947(12)\%$ [105], which allows us to constrain SABRE detection thresholds for protons at $E_{p,dep}$ down to 160 keV.

4.1.2. State at E_x = 8.490 MeV

The state at 8.490 MeV has a best-fit χ^2/doF = 2.9 when using an L = 1 distribution, which leads to a measured B_p =0.84(8) that is in agreement with the reported proton-branching ratio of B_p =79(8)% to 1 standard deviation. This state has been assigned a spin of $J^\pi(E_x = 8.490\text{MeV}) = 4^-$ in the literature, which is in agreement with an L = 4 assignment. Using 8 angular bins to fit the decay distribution in SABRE leads to a fit with χ^2/doF = 3.9 for the L = 4 distribution, but it suggests unphysically large values for the measured B_p and therefore the L = 1 assignment is used for this state. It is remarked that

this state coincides with a region in the focal plane detector with non-linearities observed in its position/energy readouts, which is also reflected in its measured excitation energy showing substantial deviation from reported values. This is also a potential source of uncertainty in the assignment made to its J^π value.

4.1.3. Doublet at E_x = 8.96/8.98 MeV

The 9.129 MeV state described below forms a shoulder to a larger resonance that has the excitation energy E_x = 8.96 MeV, which could be either (or both) of the ^{14}N states reported with E_x = 8.964(2) MeV, or E_x = 8.980(3) MeV, separated by an energy gap less than the resolution observed in this experiment. Proton decays from this state strongly favor an $L = 2$ assignment as seen in Fig. 4.2, when using 4 angular bins, but the resultant spin assignment $J = 1^-$ to 3^-does not agree with that assigned to either state (2^+ and 5^+, respectively). When we repeat our analysis with 8 angular bins as shown in Fig. 4.3, no higher L assignment leads to a better fit without $W(\theta)$ values being negative. Further, while $B_p(E_x = 8.964\text{MeV})$ =81(5)%, the B_p of the 8.980 MeV state is unknown. Therefore, we did not use this state's properties in arriving at the normalization constant C.

4.1.4. State at E_x = 9.129 MeV

The fit using the $L = 1$ assignment for the 9.129 MeV state leads to both the central value of the fit $W(\theta)$ and its 95% confidence intervals (CI) being entirely negative when $\cos(\theta) >$ -0.2, and is hence not used for spin assignment. The state supports $L = 2$ and $L = 3$ assignments when requiring the constraint $W(\theta) > 0$ to be true within the CI bounds. Both $L = 2$ and $L = 3$ assignments lead to B_p values in agreement with the reported B_p of 80(9)% [105] within 1 standard deviation. The fit using $L = 2$ leads to a spin assignment of $J^\pi = 1 - 3^-$ which agrees with with the spin of the reported $J^\pi = 3^+$ for this state, but disagrees with its parity. We hence choose the $L = 3$ assignment for this state which leads to a $J^\pi = 2 - 4^+$ assignment in agreement with literature and report a measured B_p = 70(30) %.

4.1.5. State at $E_x = 9.388$ MeV

The 9.388 MeV resonance fits an assignment of $L = 2$, in agreement with the reported B_p of 100% [105] within 1 standard deviation, and identifies a parity assignment of $J^\pi = 1 - 3^-$ in agreement with the reported values at $J^\pi = 2^-$.

4.1.6. State at $E_x = 9.703$ MeV

For this resonance, the best fit L when using 4 angular bins is $L = 2$, which leads to a measured $B_p = 95(7)\%$ that agrees with the reported B_p of 99.999959(10)% [105] within 1 standard deviation. This assignment matches the spin assignment of $J^\pi = 1^+$, but identifies it as a negative-parity state. When fit using 8 angular bins, no higher-L distribution provides an improved χ^2 without having fit $W(\theta)$ values be negative, while also simultaneously leading to agreement on the assigned J^π values to literature. Since the selection of $L = 2$ provides a good fit with the smallest number of parameters in $W(\theta)$, and partial agreement on J^π to the literature, we use $L = 2$ as the assignment for this state, indicating $J^\pi = 1 - 3^-$.

4.1.7. State at $E_x = 10.101$ MeV

The best-fit scenario for this resonance is indicated in Fig. 4.2. While an $L = 2$ assignment offers a much better quality of fit than $L = 1$, both calculations are consistent with the assignment of $B_p = 99.9983(5)\%$ from the literature, up to 1.5 and 1 standard deviations, respectively. We choose the $L = 1$ assignment since it agrees with the $J^\pi = 1^+, 2^+$ assignment in the literature [105]. In this evaluation [105], there is a state reported with $E_x = 10.079(10)$ MeV that has an unspecified proton-branching ratio, and a tentative spin-assignment of 3^+. Even though this resonance has not been reported in prior ^{12}C(^{6}Li, α)^{14}N measurements, the observed shoulder in the singles histogram in our measurement has $E_x = 10.081(1)$ MeV, in agreement with its anticipated position. The contribution seen due to this state in the coincident histograms was found to be small, and we do not report estimates to its B_p and J^π.

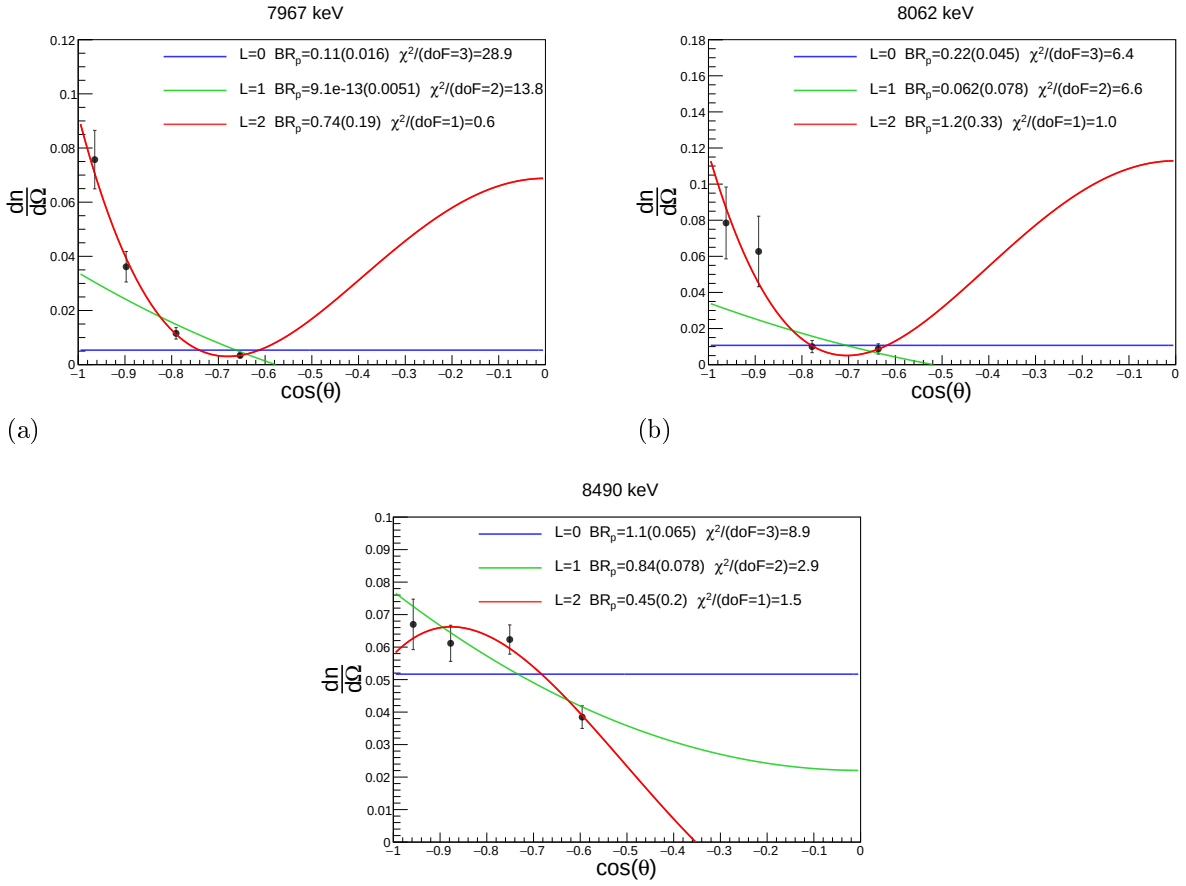

Figure 4.1. Angular distributions in SABRE of proton decays from excited states in ^{14}N with E_x =7.967-8.490 MeV. The legend includes the L-assignment to each decay, and the branching-ratio (B_p) calculated by multiplying the best-fit A_0 value by a constant factor $4\pi C$, where $C = 1.65(7)$ is arrived at empirically by using all states that have a B_p known in literature. The same normalization factor C is applied to the plots in Figs. 4.2 and 4.3.

4.1.8. State at E_x = 10.534 MeV

The best-fit scenario for this resonance is indicated in Fig. 4.2. There is a clear indication of preference towards $L = 2$ assignment, which agrees with the tentative $J^\pi = (1^-)$ assignment reported in literature [105]. The measured branching ratio is consistent with the reported 100% in literature within one standard deviation.

Figure 4.4(b) shows the comparison between the branching ratios observed in this experiment for a few states with those evaluated by the reference at [105].

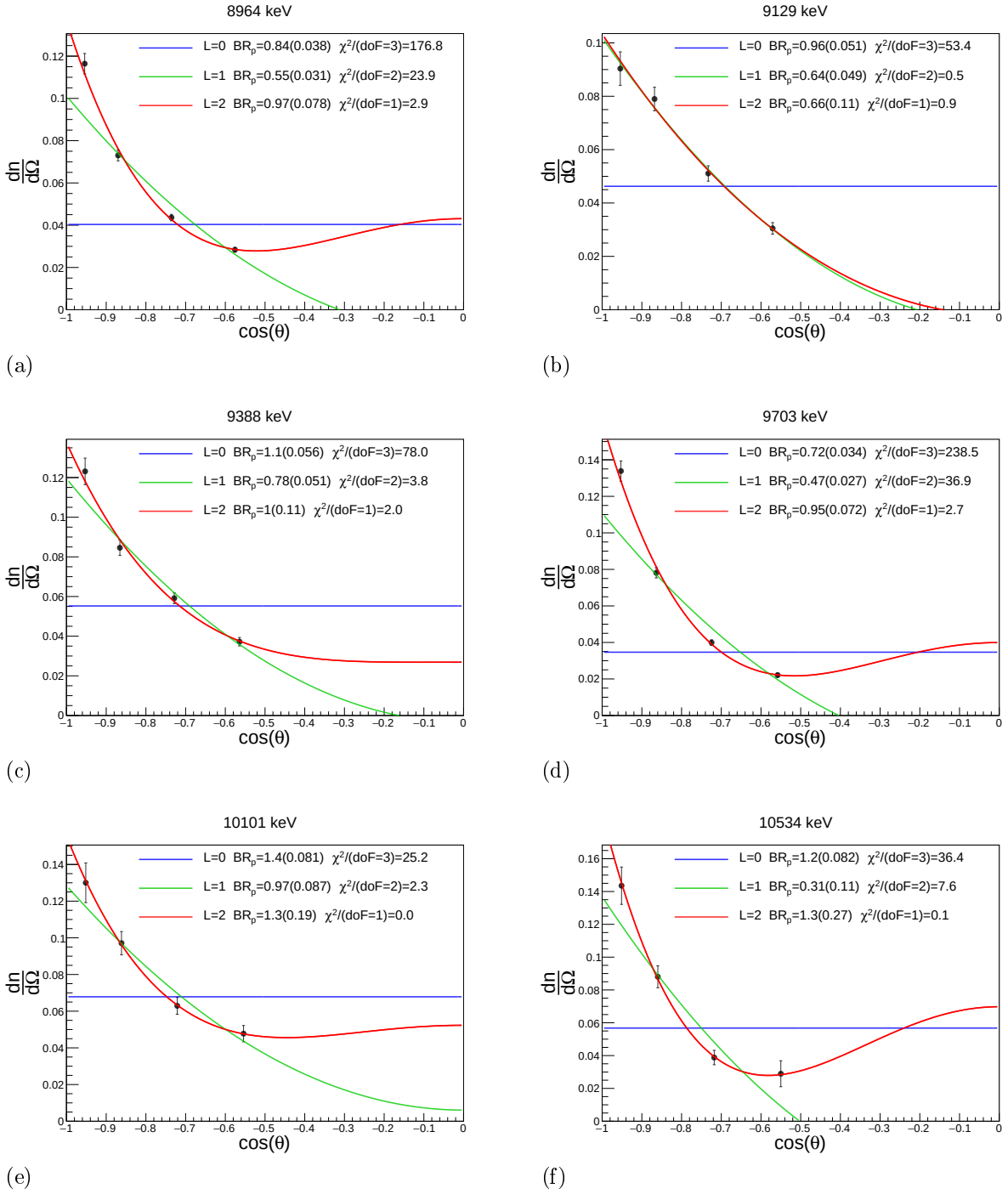

Figure 4.2. Angular distributions in SABRE of proton decays from excited states in ^{14}N with E_x =8.964-10.534 MeV(right). The same normalization factor C applied to the plots in Fig. 4.1 is used here to arrive at B_p values.

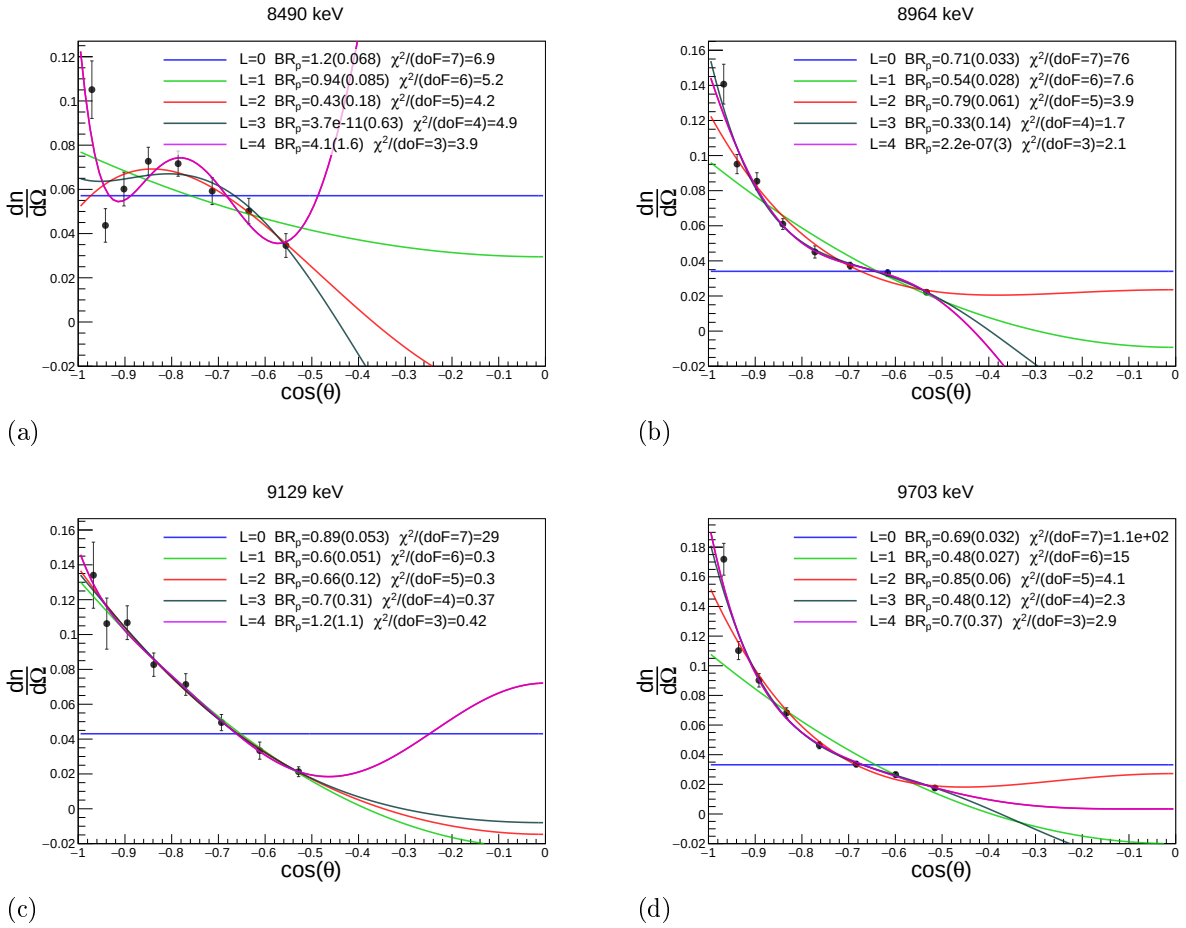

Figure 4.3. Angular distributions in SABRE of proton decays from excited states in ^{14}N with E_x =8.490, 8.96/8.98 MeV, 9.129 MeV and 9.703 MeV using 8 angular bins. The same normalization factor C applied to the plots in Fig. 4.1 is used here to arrive at B_p values.

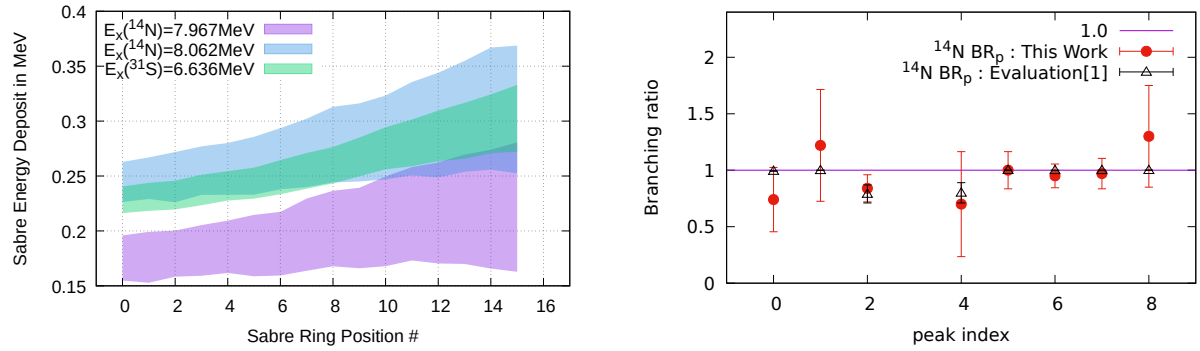

(a) (b)

Figure 4.4. (Left) Plot showing the simulated range of energies deposited in SABRE arising from proton decays of near-threshold states in ^{14}N and ^{31}S nuclei. The bands show the range between one sample standard deviation of all simulated events. (Right) Plot comparing measured proton-branching ratios in ^{14}N with those reported by the evaluation by Ajzenberg-Selove (1991) [105]. The X-axis represents the peak index as listed in the first column of Table 4.1. The error-bars used for the measured B_p values (red) are 1.5σ about the mean.

4.2. States Populated in ^{28}Si(^{6}Li,t)^{31}S*(p)^{30}P$^{g,1+2,3}$

We observed proton decays from excited states in ^{31}S populated via the ^{28}Si(^{6}Li,t)^{31}S reaction, to the ground state, as well as the first three excited states in ^{30}P. The proton decays from unbound states in ^{31}S to the first and second excited states in ^{30}P were not resolved from each other, since they are separated by only 30 keV in excitation energy [$E_x(^{30}\mathrm{P}) = 677$ and 708.7 keV, respectively]. Decays to the third excited state in ^{30}P were resolved at large excitation energies in ^{31}S [$E_x(^{31}\mathrm{S}) > 8.3$ MeV]. Tables 4.2, 4.3, 4.4, and 4.5 and Figs. 4.6, 4.7, 4.8 and 4.9 summarize the results for proton decays to the ground state. Table 4.6 and Figs. 4.10, 4.11 and 4.12 summarize the results for decays to the first three excited states in ^{30}P.

The correction factor C applied to the dataset was calculated by comparison against precisely measured B_p values in two prior experiments from three states with $E_x(^{31}\mathrm{S}) = 7.199$, 7.744 and 8.071 MeV [49, 29]. In addition, these states were well separated across the $E_x(^{31}\mathrm{S})$ spectrum, and had tightly constrained $B_{p,m}$ values in the present study, which

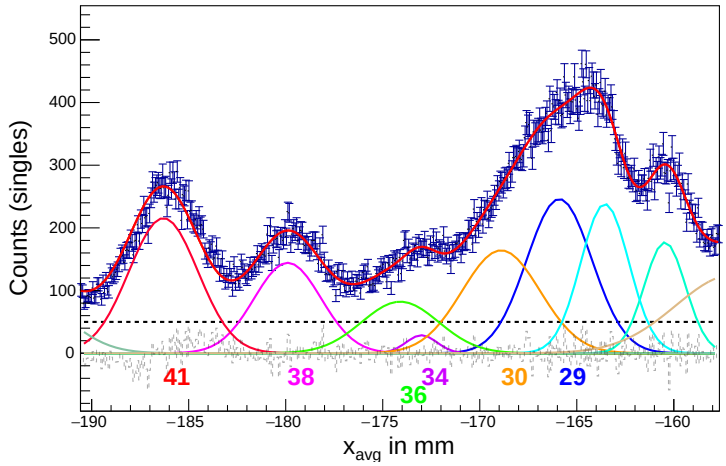

(a)

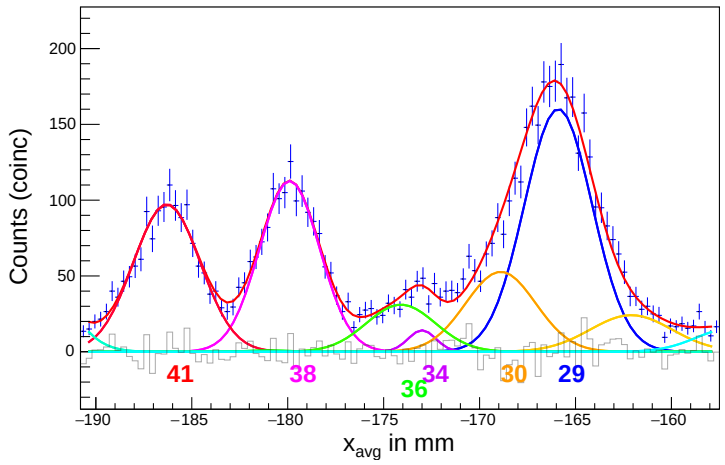

(b)

Figure 4.5. Plots showing a sample Multi-Gaussian fit performed during calculations, using the $E_x(^{31}\mathrm{S})$ = 7.8-8.3 MeV region populated in the $^{28}\mathrm{Si}(^{6}\mathrm{Li,t})^{31}\mathrm{S}^{*}(\mathrm{p})^{30}\mathrm{P}^{g,1+2,3}$ reaction.
(a) Singles histogram (blue), with the fit function (red), assumed background (dotted, black), fit residuals (grey), individual peaks and their indices as listed in Tables 4.4, 4.5 (assorted colours) are shown.
(b) Background subtracted coincident histogram for decays to $^{30}\mathrm{P}^{g}$ with the same conventions as the singles histogram. There are no coincident fit peaks corresponding to the two cyan peaks in the singles histogram with centroids at x=-164 and x=-160, and thus these states are not reported in this study. The latter corresponds to a contaminant from $^{12}\mathrm{C}$ present in the target.

Table 4.2. Properties of ^{31}S states above the proton threshold at $E_x(^{31}S) = 6.6 - 6.92$ MeV, measured using the reaction $^{28}Si(^{6}Li,t)^{31}S^{*}(p)^{30}P^{g}$. The evaluated uncertainties in the excitation energy have included in them a uniform systematic uncertainty of 10 keV arising from non-linearities observed during detector calibration. The error-bars quoted in the branching-ratio measurements represent 1σ about the mean, and are quoted assuming a scale factor $C = 1.80(0.35)$ applied uniformly to all states as discussed in Section 3.4.

Index	^{31}S Excitation Energy(keV)			L	J^{π}			$B_{p_g}(\Gamma_{p_g}/\Gamma)$		
	[40]	[29]	This work		[40]	[29]	This work	[29]	[49]	This work
1	6634.64(23)	6636.8(13)	6646(11)	3	$9/2(^{-})$	$9/2^{-}$	$3/2^{-}$ - $9/2^{-}$			0.10(0.25)
2	6720(1)	6719.8(20)			5/2	$(1/2^{-}$ - $9/2^{-})$		$0.25^{+0.07}_{-0.20}$		
3	6749(2)	6749(2)	6746(12)	0	$3/2^{+}$	$7/2^{-}$ - $9/2^{-}$	$1/2^{+}$ - $3/2^{+}$	$0.57^{+0.07}_{-0.32}$		0.05(0.01)[a]
4	6796(25)	6796(25)				$11/2^{-}$				
5	6832.7(3)	6833.4(3)			11/2(-)	$11/2^{-}$				
6	6836(2)	6836.5(18)	6837(11)	0		$(1/2^{+}$ - $9/2^{-})$	$1/2^{+}$ - $3/2^{+}$	$0.48^{+0.07}_{-0.34}$		0.04(0.01)[a]
7	6869(2)	6872(2)	6869(10)	1	11/2	$\geq 1/2^{-}$	$1/2^{-}$ - $5/2^{-}$	$0.37^{+0.09}_{-0.13}$		0.08(0.02)[a]

[a] Uncertainties do not include large systematic uncertainties due to background subtraction in singles spectrum

Table 4.3. Properties of ^{31}S states above the proton threshold at $E_x(^{31}S) = 6.92 - 7.5$ MeV, measured using the reaction $^{28}Si(^{6}Li,t)^{31}S^{*}(p)^{30}P^{g}$. The same uncertainties and normalization apply to this table as described in the caption to Table 4.2.

Index	^{31}S Excitation Energy(keV)			L	J^π			$B_{p_g}(\Gamma_{p_g}/\Gamma)$		
	[40]	[29]	This work		[40]	[29]	This work	[29]	[49]	This work
8	6936(2)	6938.1(29)			$1/2^+$ - $5/2^+$	[a]		$1.25^{+0.40}_{-1.03}$		
9	6959(2)	6961(3)	6952(10)	0	$(1/2^+)$	$1/2^+$	$1/2^+$ - $3/2^+$	$0.46^{+0.11}_{-0.40}$		<0.33
10	6972(2)	[6975(3)]	6975(10)	0	$1/2^+$		$1/2^+$ - $3/2^+$	<0.38		1.1(0.3)
11	7010(10)		7016(10)	1			$1/2^-$ - $5/2^-$			$0.30^{+0.17}_{-0.17}$
12	7036(2)	7035.4(20)			$(3/2^+$ - $5/2^+)$	$(1/2^+);3/2$		$1.05^{+0.05}_{-0.05}$		
13	7037(2)	7038(4)			$(3/2^+$ - $5/2^+)$	$5/2^+$			$0.93^{+0.14}_{-0.10}$	
14	7050.1(8)	[7053(2)]	7050(10)	0	$(1/2^+$ - $5/2^+)$	$5/2^+$	$1/2^+$ - $3/2^+$	$0.36^{+0.15}_{-0.33}$		1.30(0.27)
15			7074(10)	0			$1/2^+$ - $3/2^+$			0.21(0.04)
16	7150.0(8)		7143(10)	0	$1/2^+$ - $5/2^+$		$1/2^+$ - $3/2^+$			<0.09
17	7157.5(11)	7156.5(17)			$3/2^+$ - $5/2^+$	[b]		$1.04^{+0.11}_{-0.63}$	$0.30^{+0.09}_{-0.06}$	
18	7196(2)	7196.1(2)	7205(12)	1		$\geq 1/2^-$	$1/2^-$ - $5/2^-$	$0.67^{+0.08}_{-0.12}$		0.68(0.15)
19	7302.4(5)	7302.7(7)				$11/2^+$		<0.13		

[a] $J^\pi = (1/2^+$ - $5/2^+)$
[b] $J^\pi = (3/2^+$ - $5/2^+)$

Table 4.4. Properties of ^{31}S states above the proton threshold at $E_x(^{31}S) = 7.5 - 8.05$ MeV, measured using the reaction $^{28}Si(^{6}Li,t)^{31}S^{*}(p)^{30}P^{g}$. The same uncertainties and normalization apply to this table as described in the caption to Table 4.2.

Index	^{31}S Excitation Energy(keV)			L	J^π			$B_{p_g}(\Gamma_{p_g}/\Gamma)$		
	[40]	[29]	This work		[40]	[29]	This work	[29]	[49]	This work
20	7501(3)	7501(3)				[a]		$0.58^{+0.44}_{-0.09}$		
21	7517(3)	7519(3)	7532(11)	1		[a]	$1/2^-$ - $5/2^-$	$1.57^{+0.25}_{-0.97}$		1.0(0.2)
22	7584(2)	7585(3)				[a]		$0.55^{+0.70}_{-0.13}$		
23	7699(3)	7699.1(28)			$(1/2^+$ - $5/2^+)$	$(5/2^+)$		$0.57^{+0.11}_{-0.13}$		
24	7725(3)	7725.0(21)			$(1/2-3/2,5/2^+)$	$1/2^-$		<0.47		
25	7744(3)	7744(3)	7740(10)	1		$\geq 5/2^+$	$1/2^-$ - $5/2^-$	$1.00^{+0.06}_{-0.06}$	$0.88^{+0.08}_{-0.04}$	0.67(0.22)
				2			$1/2^+$ - $7/2^+$			1.1(0.5)
26	7774(3)	7774(3)			$(1/2^+$ - $5/2^+)$	[a]		$0.92^{+0.18}_{-0.64}$		
27	7907(3)	7905(3)			$1/2^+$	[a]		$0.34^{+0.12}_{-0.29}$	$0.2^{+0.03}_{-0.03}$	
28	7932(3)	7932(3)				[a]		$1.22^{+0.18}_{-0.69}$		
29	7945(3)	7945(3)	7942(10)	1		[a]	$1/2^-$ - $5/2^-$	$1.29^{+0.30}_{-0.95}$		0.78(0.16)
30	7973(3)	7973(3)	7987(10)	2		[a];3/2	$1/2^+$ - $7/2^+$	$0.62^{+0.11}_{-0.42}$		0.70(0.18)
31	8015(3)	8015.2(29)				[b]		$0.67^{+0.19}_{-0.52}$		
32	8022(3)									
33	8030(3)	8030(3)				[a]		$1.18^{+0.16}_{-0.75}$		
34	8044.5(12)	8045(27)	8046(10)	0	$1/2^+$ - $5/2^+$	[b]	$1/2^+$, $3/2^+$	$0.66^{+0.11}_{-0.44}$		0.88(0.29)

[a] $J^\pi = (1/2^+$ - $13/2^-)$
[b] $J^\pi = (1/2^+$ - $5/2^+)$

Table 4.5. Properties of ^{31}S states above the proton threshold at $E_x(^{31}S) = 8.05 - 8.6$ MeV, measured using the reaction $^{28}Si(^{6}Li,t)^{31}S^{*}(p)^{30}P^{g}$. The same uncertainties and normalization apply to this table as described in the caption to Table 4.2.

Index	^{31}S Excitation Energy(keV)			L	J^π			$B_{p_g}(\Gamma_{p_g}/\Gamma)$		
	[40]	[29]	This work		[40]	[29]	This work	[29]	[49]	This work
35	8060(3)	8060(3)						<0.36		
36	8071(3)	8071(3)	8063(10)	2		[a]	$1/2^+$ - $7/2^+$	$1.07^{+0.22}_{-0.75}$	$0.42^{+0.08}_{-0.06}$	0.5(0.2)
37	8122(2)	8106(10)			$1/2^+$ - $5/2^+$	[a]		$1.08^{+0.39}_{-0.93}$		
38	8130(2)	8131(3)	8147(10)	1		$\geq 1/2^-$	$1/2^-$ - $5/2^-$	$0.71^{+0.13}_{-0.13}$		1.1(0.23)
39	8178(3)	8177.7(29)				[b]		$1.00^{+0.15}_{-0.15}$		
40	8210(2)	[8209(3)]				[a]		<0.33		
41	8229(3)	8229(3)	8240(10)	1		[a]	$1/2^-$ - $5/2^-$	$0.86^{+0.33}_{-0.55}$		0.69(0.14)
42	8268(10)	8268(10)			$1/2^+$ - $5/2^+$	[c]				
43	8330(8)	8330(8)	8341(12)	2		[a]	$1/2^+$ - $7/2^+$	$1.16^{+0.2}_{-0.78}$		0.61(0.18)
44	8386(3)	8379(9)				[a]		$0.90^{+0.14}_{-0.58}$		
45	8424(3)	8418(5)	8424(11)	1	$1/2^+$ - $5/2^+$	[c]	$1/2^-$ - $5/2^-$			0.41(0.08)
46	8460.8(4)	8461			$(13/2^-)$	$13/2^-$				
47	8498(4)	8501(5)	8490(12)	2	$1/2^+$	$1/2^+$	$1/2^+$ - $7/2^+$			0.53(0.24)
48			8515(14)	1			$1/2^-$ - $5/2^-$			0.81(0.20)
49	8563(2)	8562(8)								

[a] J^π =($1/2^+$ - $13/2^-$)
[b] J^π =($5/2^+$ - $13/2^-$)
[c] J^π =($1/2^+$ - $5/2^+$)

Table 4.6. Properties of ^{31}S states with $E_x(^{31}S) > 7.5$ MeV, measured using the reaction ^{28}Si(^{6}Li,t)^{31}S*(p)^{30}P$^{1+2,3}$. The same uncertainties and normalization apply to this table as described in the caption to Table 4.2.

Index	^{31}S Excitation Energy(keV)			$B_{p_{1+2}}(\Gamma_{p_{1+2}}/\Gamma)$		$B_{p_3}(\Gamma_{p_3}/\Gamma)$
	[40]	[29]	This work	[29]	This work	This work
20	7501(3)	7501(3)		<0.02		
21	7517(3)	7519(3)	7532(11)	<0.08	<0.02	
22	7584(2)	7585(3)		<0.05		
23	7699(3)	7699.1(28)		<0.02		
24	7725(3)	7725.0(21)		$0.48^{+0.10}_{-0.34}$		
25	7744(3)	7744(3)	7740(10)	<0.03	0.12(0.03)	
29	7945(3)	7945(3)	7942(10)	<0.03	<0.02	
30	7973(3)	7973(3)	7987(10)	$0.70^{+0.09}_{-0.44}$	$0.36^{+0.08}_{-0.08}$	
36	8071(3)	8071(3)	8063(10)	<0.62	$0.28^{+0.08}_{-0.08}$	
38	8130(2)	8131(3)	8147(10)	$0.05^{+0.02}_{-0.04}$	$0.08^{+0.02}_{-0.02}$	
41	8229(3)	8229(3)	8240(10)	$0.40^{+0.08}_{-0.28}$	0.13(0.03)	
43	8330(8)	8330(8)	8341(12)	$0.13^{+0.06}_{-0.12}$	0.06(0.04)	0.04(0.01)
45	8424(3)	8418(5)	8424(11)		0.71(0.14)	0.04(0.03)
47	8498(4)	8501(5)	8490(12)		$0.43^{+0.10}_{-0.10}$	<0.1
48			8515(14)		$0.10^{+0.03}_{-0.03}$	$0.22^{+0.05}_{-0.05}$

made it meaningful to use them to characterize the detection efficiency. The inverse-variance weighted average value of C over these three states was 1.80(0.35), which was applied to all the measured ^{31}S branching-ratios, the results from which are discussed below.

4.2.1. E_x = 6.64 MeV

The resonance with $E_x(^{31}\mathrm{S})$ = 6.64 MeV had only 67(5) counts in its coincidence spectrum that were recorded above background. For this reason, the coincident spectra from this state were not fit with Gaussians, but decay events above background were counted for each individual angular bin and used to determine the angular correlation factor $W(\theta)$ and the L assignment. The additional assumption that the proton decays in this region arise from only the well-characterized 9/2(-) resonance in the region is made. There has been a recent publication describing a measurement of the ^{32}S(d,t)^{31}S transfer reaction using a Q3D spectrograph that reports an additional state detected with unknown properties at $E_x(^{31}\mathrm{S})$ = 6.648 MeV [106]. The newly observed state was seen to be a shoulder to the previously known state very close to the limit of detection under the experimental conditions. We do not include this tentative state in our analysis.

In the present measurement, the observed angular distribution showed comparable fit quality for the $L = 2$ and $L = 3$ distributions. If we choose the $L = 3$ distribution since it agrees with the reported $J = 9/2(-)$ assignment under the latest evaluation [40], it provides us with a measured value of 0.10(0.25) for this resonance's proton-branching ratio at $\chi^2/\mathrm{doF} = 2.3$. With the $L = 2$ distribution, we obtain $\chi^2/\mathrm{doF} = 1.9$ and $B_p = 0.24(0.09)$ which is only marginally better in fit quality than the $L = 3$, while providing a spin estimate that disagrees with J=9/2(-). The fit using $L = 4$ distribution strongly appears to overfit the data, and leads to an unphysically large estimation of B_p under the scaling constant C used.

We remark here that the possibility of the angular distribution possessing contributions from more than one state, or a state that is not the one previously identified J=9/2(-),

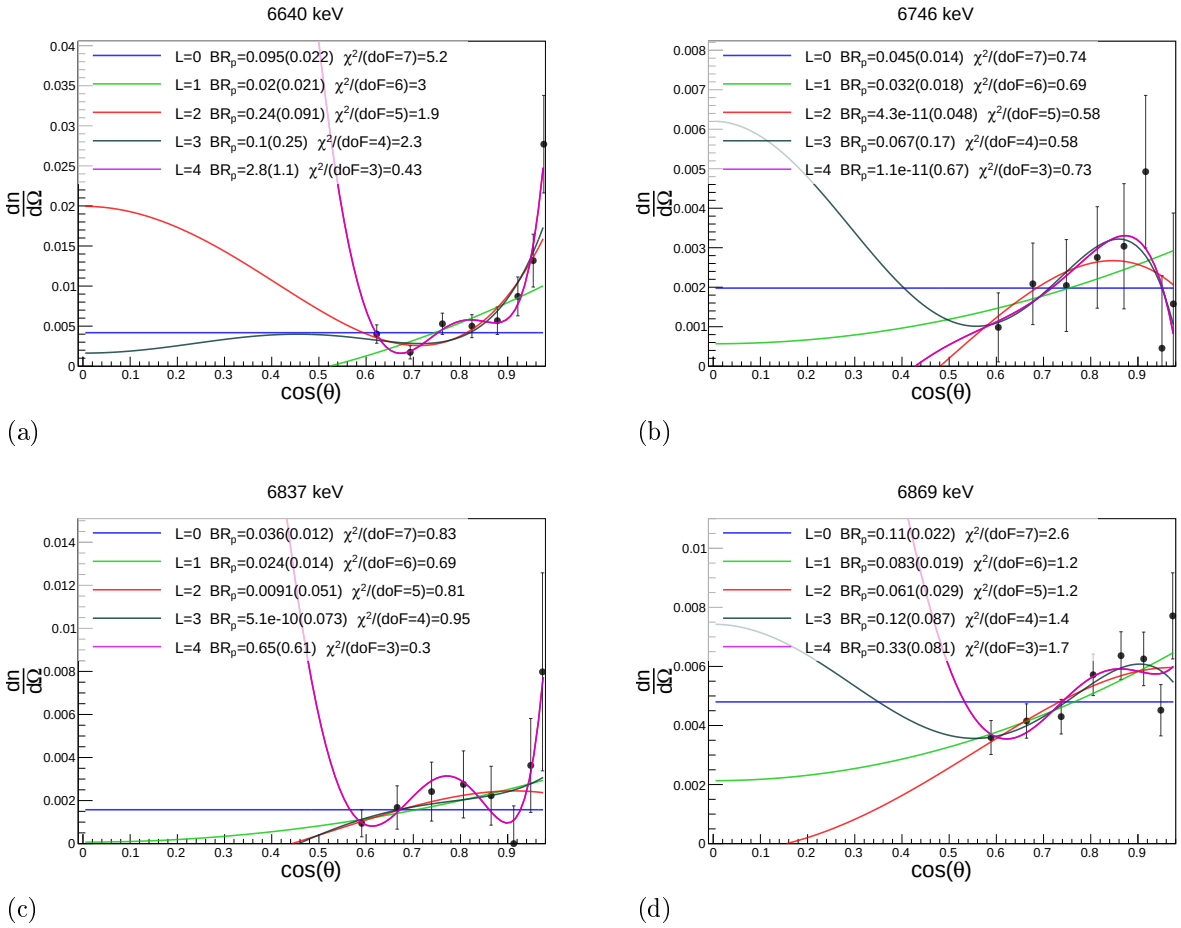

Figure 4.6. Angular distributions in SABRE of proton decays from excited states in ^{31}S with $E_x = 6.6 - 6.9$ MeV to the ground state in ^{30}P. Eight angular bins were used for the 6640 MeV resonance in anticipation of its $L = 3$ or $L = 4$ assignment.

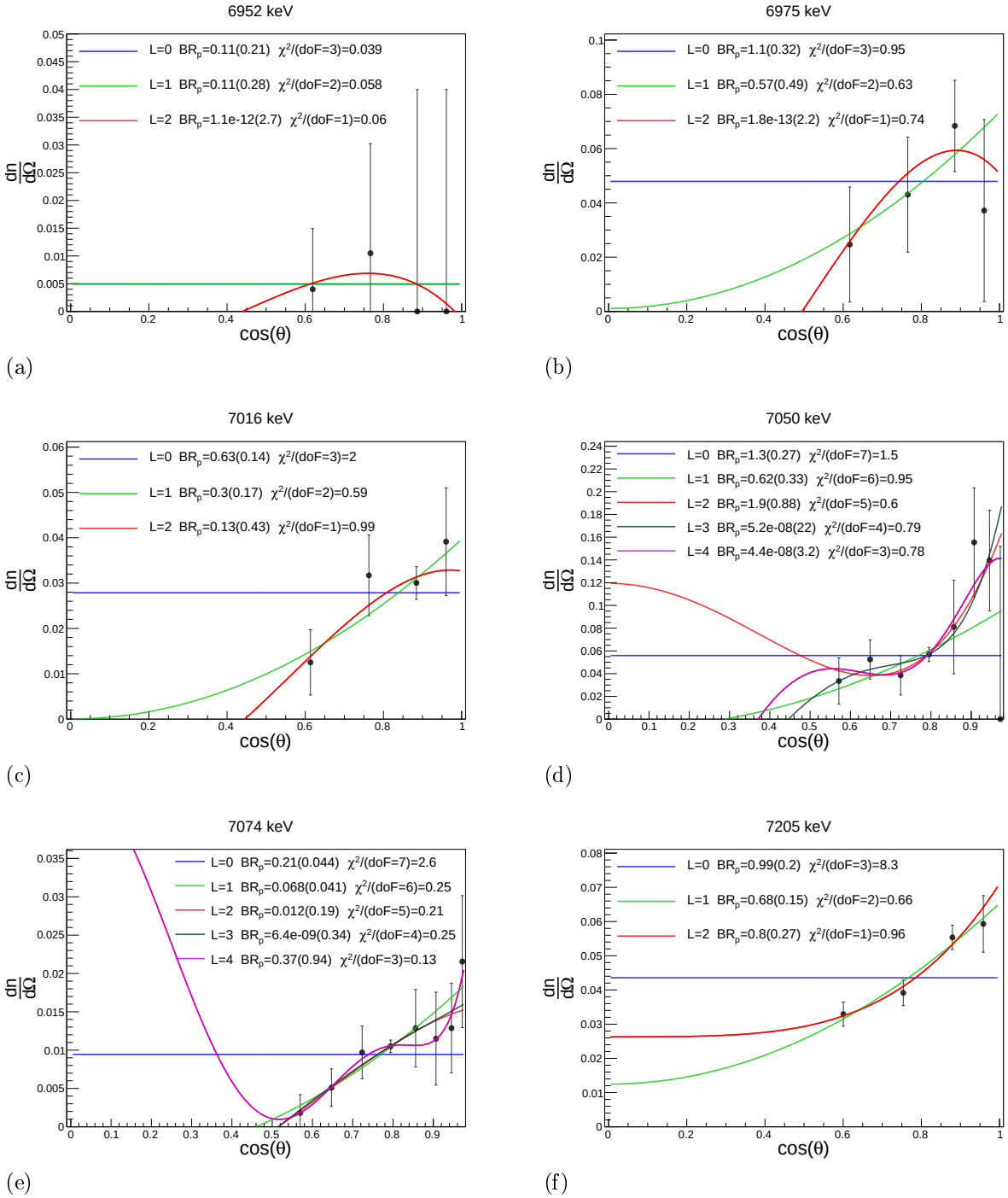

Figure 4.7. Angular distributions in SABRE of proton decays from excited states in ^{31}S with $E_x = 6.9 - 7.2$ MeV to the ground state in ^{30}P.

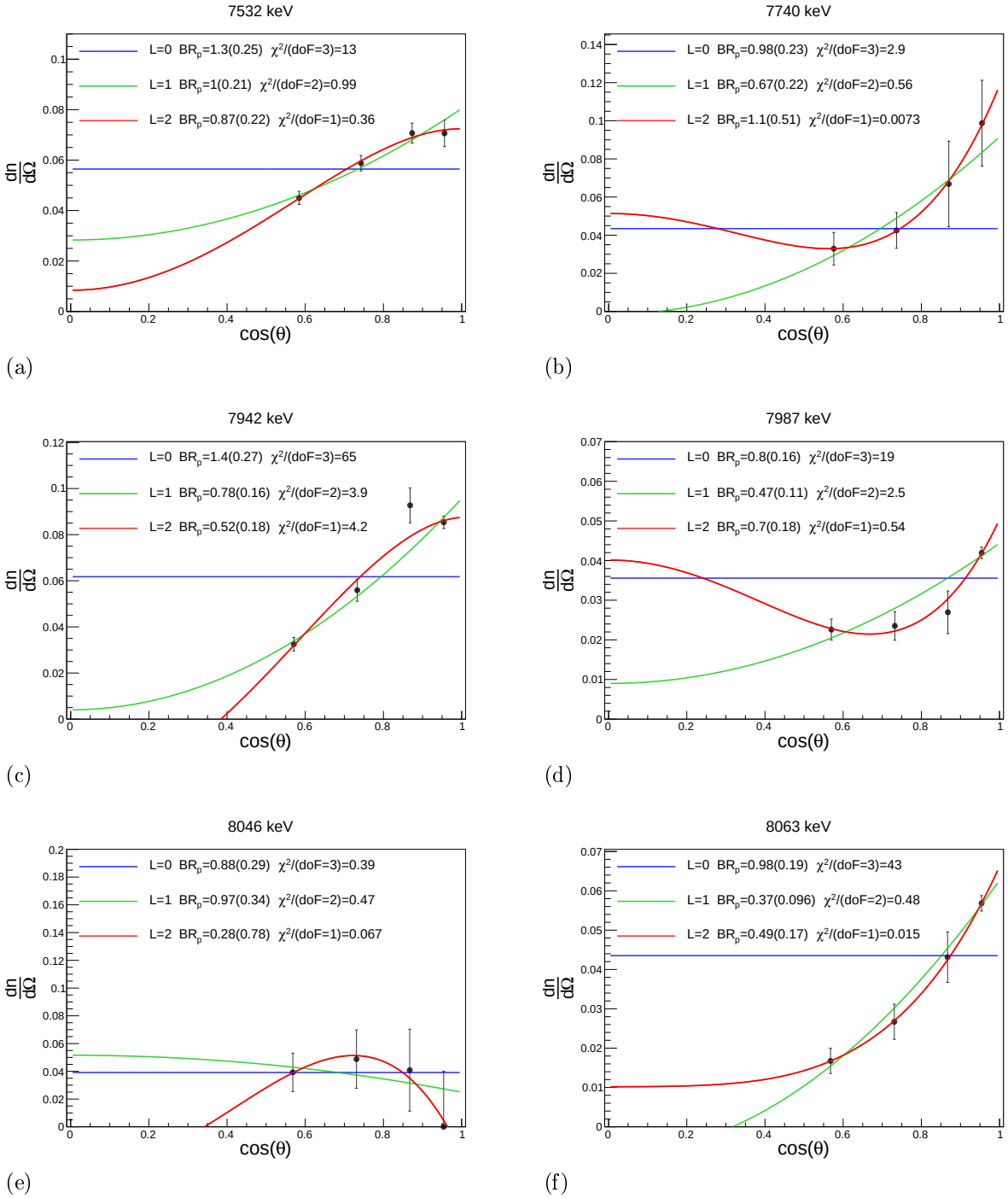

Figure 4.8. Angular distributions in SABRE of proton decays from excited states in ^{31}S with $E_x = 7.5 - 8.1$ MeV to the ground state in ^{30}P.

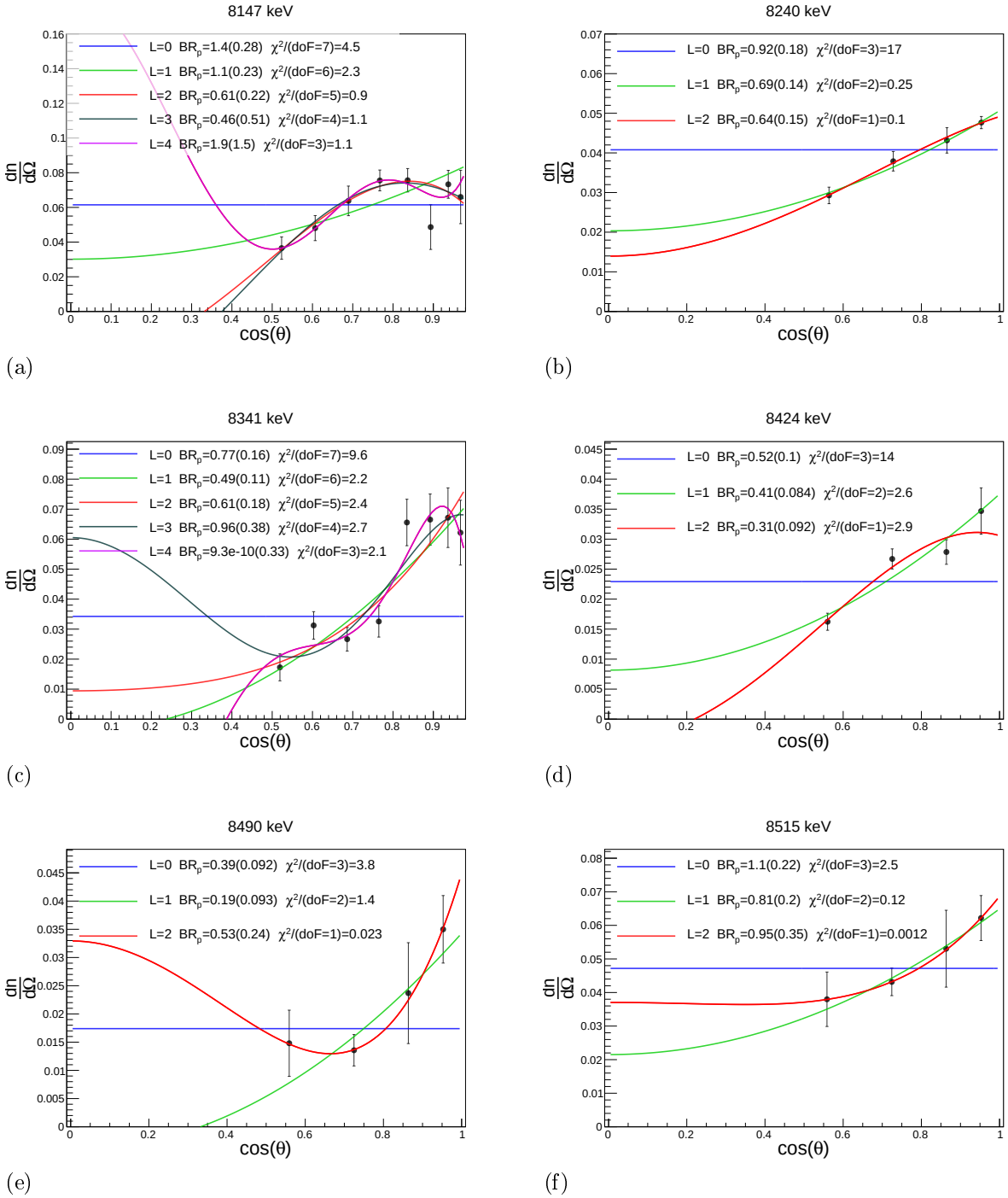

Figure 4.9. Angular distributions in SABRE of proton decays from excited states in ^{31}S with $E_x = 8.1 - 8.6$ MeV to the ground state in ^{30}P.

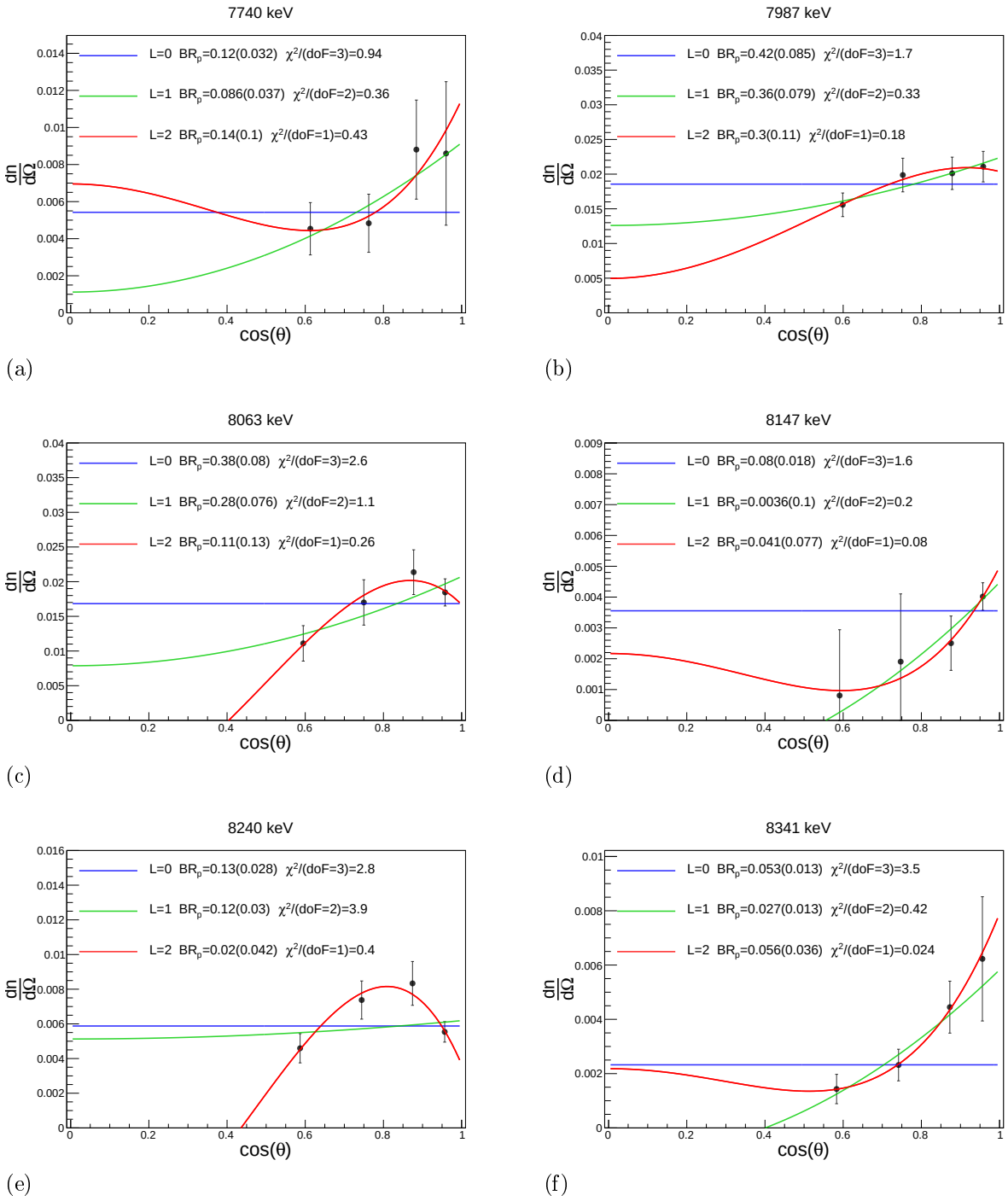

Figure 4.10. Angular distributions in SABRE of proton decays from excited states in ^{31}S with $E_x = 7.7 - 8.4$ MeV to the first and second excited states (taken together) in ^{30}P. Only cases with a sufficiently large number of counts are shown.

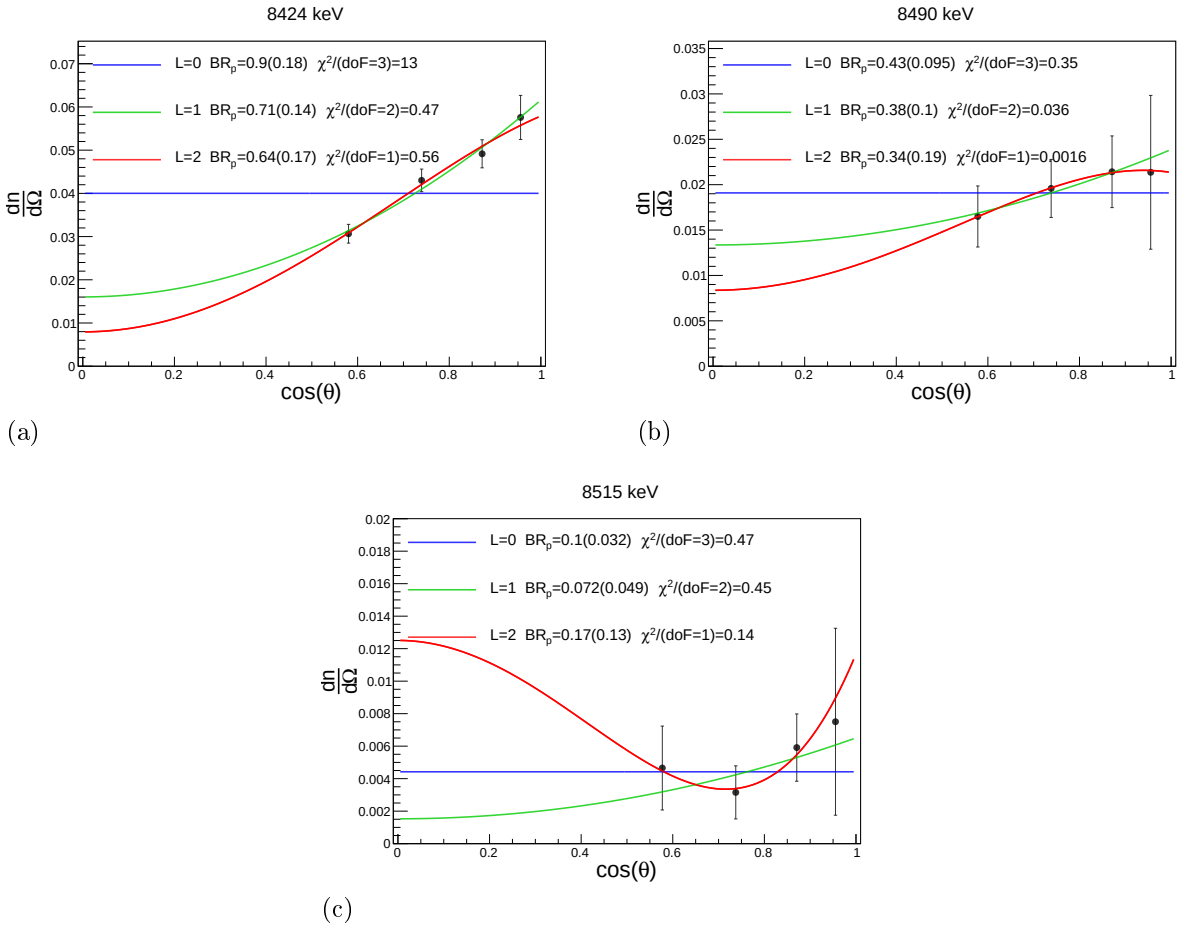

Figure 4.11. Angular distributions in SABRE of proton decays from excited states in ^{31}S with $E_x = 8.4 - 8.6$ MeV to the first and second excited states (taken together) in ^{30}P. Only cases with a sufficiently large number of counts are shown.

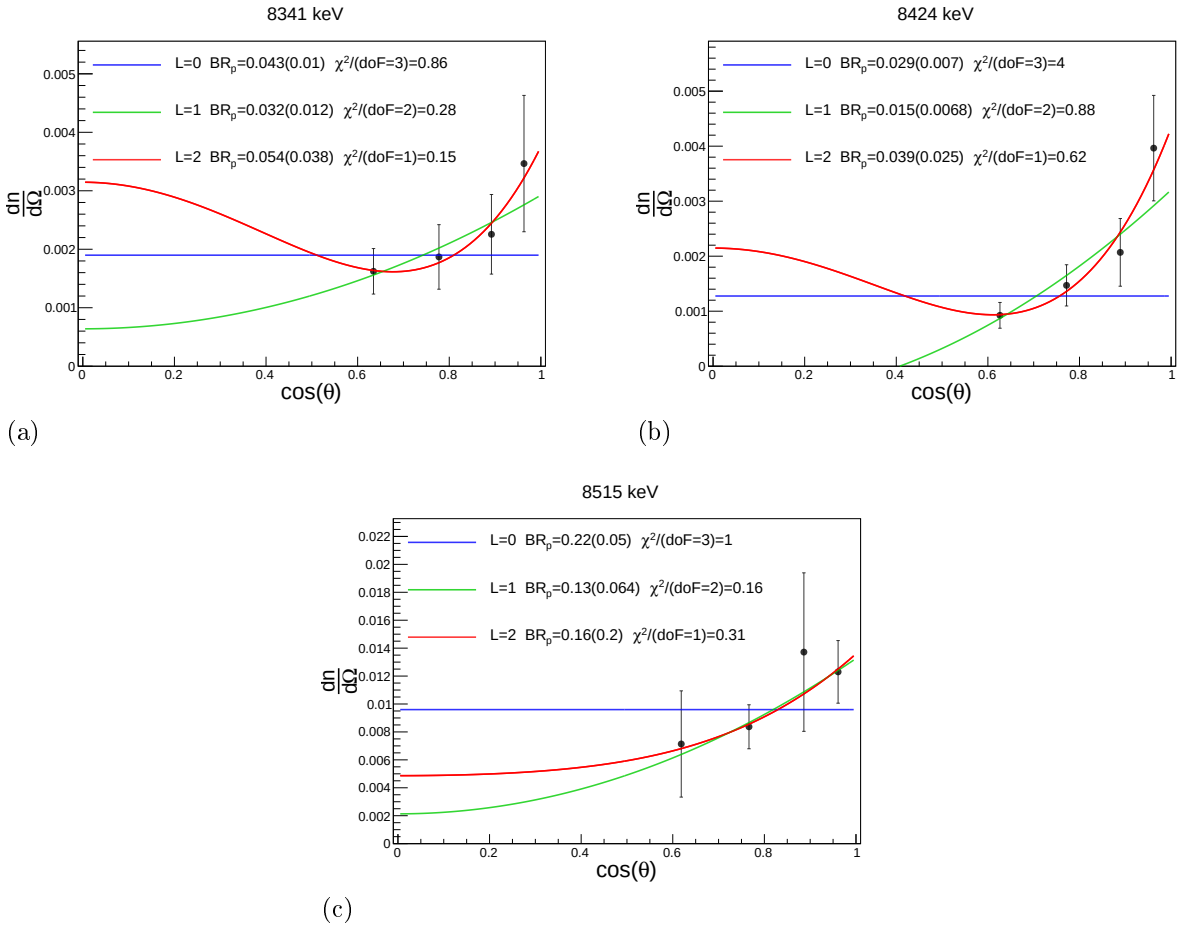

Figure 4.12. Angular distributions in SABRE of proton decays from excited states in ^{31}S with $E_x = 8.4 - 8.6$ MeV to the third excited state in ^{30}P. Only cases with a sufficiently large number of counts are shown.

is not ruled out by the current measurement. The measured branching ratio is reported assuming the other states do not contribute significantly. Nevertheless, the counts observed in the present experiment represent reliable detection of decay protons from this region in excitation energy, since the detection threshold of the setup has already been quantified to be lower than their expected energy.

4.2.2. E_x = 6.7-6.9 MeV

The presence of two strong contaminant peaks arising from ^{12}C(^{6}Li,t)^{15}O at $E_x(^{15}\mathrm{O})$ = 5.183 and 5.240 MeV render it difficult to resolve the singles spectrum in this energy region. Nevertheless, fitting the coincident spectrum clearly resolves states at $E_x(^{31}\mathrm{S})$ = 6.837(11) MeV, 6.869(10) MeV and 6.746(12) MeV whose angular distributions either match with the spins reported in the latest evaluation or with the measurement in [29]. The branching ratios assigned to all three of these states are identified as tentative due to the strong background from the ^{15}O states that were poorly resolved in the singles spectrum.

4.2.3. E_x = 6.95-7.5 MeV

Seven ^{31}S states were resolved in this region, whose measured properties show broad agreement with prior measurements. Fits to the 8 angular bin distribution are reported for two states in this region, due to the difficulty involved in consistently fitting them when using four angular bins. The relatively structureless region in the singles spectrum around $\mathrm{E}_x(^{31}S)$ = 7.35-7.45 MeV observed in this measurement showed agreement with the singles spectrum from a prior $^{31}P(^{3}\mathrm{He,t})^{31}\mathrm{S}$ study [29], and was used to estimate the background counting rate when fitting the singles spectrum. The weakly-populated broad peak in the singles spectrum around $\mathrm{E}_x(^{31}S)$ = 7.27-7.35 MeV showed a strong correlation with coincident spectra arising from events outside of the $^{28}\mathrm{Si}(^{6}\mathrm{Li,t})^{31}\mathrm{S}^{*}(\mathrm{p})^{30}\mathrm{P}^{g,1+2,3}$ gates — in particular, from other isotopes of Si present in the target. The proton-branching ratios from resonances in this region are not reported here because of the dominant background.

The normalized $B_{p,g}$ value of 0.68(0.15) measured for the strongly-populated resonance at $E_x(^{31}S) = 7.20$ MeV showed good agreement with its previous measurement by Wrede *et al.* [29] of $0.67^{0.08}_{-0.12}$. Under the current calibration and resolution, it is not clear whether the resonance observed at $E_x(^{31}\mathrm{S}) = 7.050(10)$ MeV in the present measurement corresponds to the state at $E_x(^{31}\mathrm{S}) = 7.037(2)$ MeV or the one at 7.050(1) MeV. Under the assumption that the observed state corresponds to the one measured at $E_x(^{31}\mathrm{S}) = 7.036(7)$ MeV, the measured $B_{p,g}$ of 1.3(0.3) when renormalized to unity agrees within one standard deviation with both measurements made on it before [49, 29]. The measured value being larger than 1.0 is attributed to the level density in this region, and the uncertainty arising from poor resolution of peak features when performing multi-Gaussian fits. Due to the same sources of error, this state was not used to cross-validate the choice of scale-factor C adopted in this measurement.

4.2.4. E_x = 7.5-7.8 MeV

In agreement with the two previous measurements reporting proton decays from this state, the state at $E_x(^{31}S) = 7.740$ MeV reported a measured proton-branching ratio of $B_{p,g} = 1.1(0.5)$ when the $L = 2$ distribution was used to fit its features. This also leads to a spin assignment in agreement with reported spin values. The angular distribution from this state also had a good quality fit with an $L = 1$ distribution, which leads to a measured $B_{p,g} = 0.67(0.22)$. Both of these values agree within uncertainty with the measurement made by Burcher *et al.* [49], and are within 1 and 1.5 standard deviations, respectively, of the previous measurement made by Wrede *et al.* [29], which reported $B_{p,g} = 1.00(0.06)$. This provides an additional cross-check of the correction-factor used when reporting the branching ratios.

In addition to this resonance, a significant proton decay branch to $^{30}\mathrm{P}^{1+2}$ from the state at $E_x(^{31}S) = 7.58$ MeV was observed. At first glance, this strongly suggests the identification of proton decays from a previously unmeasured state in the region - since there was not a similar observation by Wrede *et al.* [29]. However, the presence of a strong contaminant

peak [E(^{19}Ne) = 2.795 MeV from ^{16}O(^{6}Li,t)^{19}Ne] in the singles spectrum prevented us from further analysis of this state. It is remarked that a measurement identical to the present measurement that uses a self-supporting ^{28}Si target would minimize the distortion due to this background state and potentially permit the measurement of proton branching around E$_x$(^{31}S) = 7.58 MeV.

Lastly, strong proton decay branching to ^{30}P^g was observed from the highly-populated state at E$_x$(^{31}S) = 7.532(11) MeV. Both $L = 1$ and $L = 2$ assignments provided a good fit to the decay angular distribution in SABRE, and indicate $B_{p,g}$ values consistent with prior measurements [29], with improved precision.

4.2.5. E_x = 7.8-8.3 MeV

As many as six excited states were resolved in this energy region. As the presence of a contamination peak from the background reacton ^{12}C(^{6}Li,t)^{15}O populating the E_x(^{15}O) = 6.176 MeV resonance obscured the features in the singles spectrum, we do not report on states around E$_x$(^{31}S) = 7.75-7.85 MeV. In agreement with previous observations [49, 29], the decay branches to the first- and second-excited states in ^{30}P showed large strength in the region E_x(^{31}S) = 7.8-8.1 MeV. Finally, the proton-branching ratio observed to ^{30}P^g from the resonance at E$_x$(^{31}S) = 8.07 MeV was used to calculate the scaling-factor C. The currently observed value of $B_{p,g} = 0.5(0.2)$ showed good agreement with the measurement in [49] that reported $B_{p,g} = 0.42^{+0.08}_{-0.06}$.

4.2.6. E_x = 8.3-8.6 MeV

This region was the furthest from the proton emission threshold among all the states observed. There were predominantly three peaks in the singles spectrum that were fit using four states based on the coincident spectra. While it is likely that the level density in this region is even higher, the results reported here correspond to only what was resolved with the energy resolution available in the experiment. The coincident spectra corresponding to de-

cays to different excited states in ^{30}P showed identifiable differences in their structure, which allowed for resolution of two states around $E_x(^{31}S)$ = 8.48-8.51 MeV. Strong proton decay branches were observed to the first- and second-excited states of ^{30}P from the resonances at $E_x(^{31}S)$ = 8.424 and 8.490 MeV. A large decay branch to the third excited state in ^{30}P was observed for the resonance at $E_x(^{31}S)$ = 8.515 MeV. Many of these measurements are reported for the first time, and could prove useful as reference states with well-constrained B_p values for subsequent measurements that study the same nucleus.

The next section will briefly discuss the impact of the current measurement on the estimate of the ^{30}P(p,γ)^{31}S reaction rate.

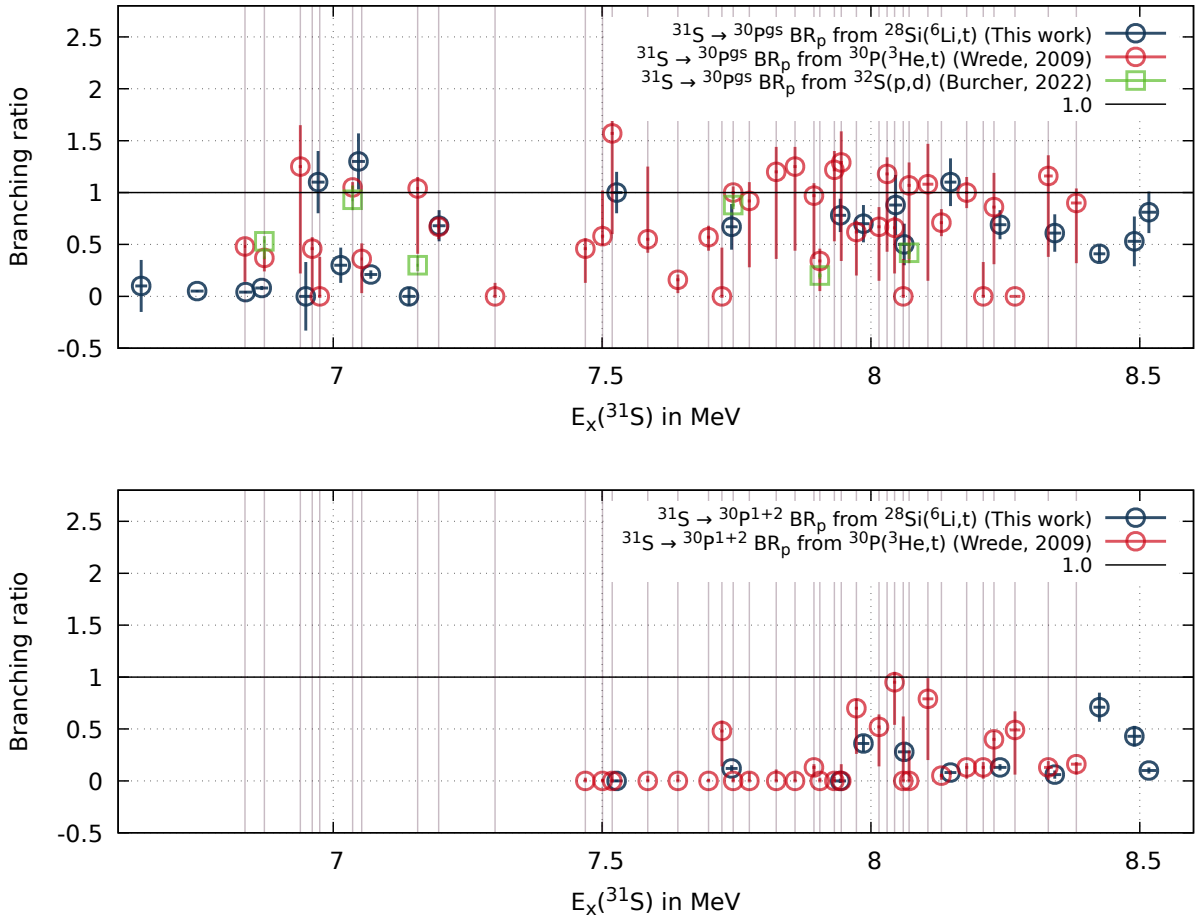

Figure 4.13. (Top) Comparison of measured proton-branching ratios from excited states in ^{31}S to the ground state of ^{30}P seen in this measurement (blue) against previous measurements by Wrede *et al.* [29] (red) and Burcher *et al.* [49] (green). Thin grey lines are drawn corresponding to the mean $E_x(^{31}\mathrm{S})$ values reported in [29] to guide the eye. (Bottom) The same plot as above, but for proton-branching ratios from excited states in ^{31}S to the first two excited states of ^{30}P.

Chapter 5. .Influence on Reaction Rate, Future Prospects

In order to examine the impact of the measurement discussed in the previous chapters on the ^{30}P(p,γ)^{31}S reaction rate, a careful literature survey was performed to obtain the most up-to-date information regarding the proton and γ-ray partial widths, and spin assignments estimated for all narrow resonances in the Gamow window $E_x(^{31}\mathrm{S})$ = 6.1-6.8 MeV. The findings are summarized in Table 5.1. Evidence of strong isospin mixing of the $E_x(^{31}\mathrm{S})$ = 6390 keV state with the $T = 3/2$ IAS had been determined experimentally by Bennett *et al.* in 2016 [60], which provided an unambiguous constraint on this state's parity as $J^\pi = 3/2+$. This s-wave resonance is presently understood to be the dominant contributor to the reaction rate, located in the middle of the Gamow window at ONe nova burning temperatures ($T = 0.1 - 0.4$ GK). For this level, we adopt the resonance strength assigned to it in the latest peer-reviewed measurement [63].

In the year following the measurement by Bennett *et al.*, Kankainen *et al.* [51] used the GRETINA array to experimentally constrain several resonance strengths in the ^{30}P(p,γ)^{31}S reaction. This measurement detected the angle-integrated cross-section of the ^{30}P(d,n)^{31}S proton-transfer reaction, and compared the results against predictions from a finite-range adiabatic approximation model that used a USDA Hamiltonian for positive parity states, and the WBP Hamiltonian for negative parity states to determine the spectroscopic factors, C^{2}S, corresponding to each resonance in the Gamow window. They observed about an order of magnitude lower single-particle strength than those predicted by the shell model for the three dominant negative-parity states participating in the reaction, and provided an updated list of resonance strengths over many states in the Gamow window guided by the experiment. For the other important resonances that were not observed experimentally, they reported theoretical estimates calculated in a previous publication [107]. We adopt the values listed in this publication [51] for our reaction rate calculations with the exception of the recently updated 6390 keV state.

For the $E_x(^{31}\mathrm{S})$ = 6.636 MeV resonance, we assume that its properties are identical to

the previously measured J^{π} =9/2- state. (There has been a recent Q3D measurement [106] that indicated a neighboring state at $E_x(^{31}\mathrm{S}) = 6.648$ MeV with as-yet unknown properties). The spin of this state has been identified in several measurements including coupled-channel angular distribution measurements using ^{30}P(^{3}He,t)^{31}S [46], and ^{28}Si(α,nγ) using Gamma-sphere [58], which identified this resonance as the mirror to the E_x = 6796-keV state in ^{31}P. To estimate its resonance strength, we use the γ width quoted in references [47, 54] of 3.3(7) meV, which is derived from the mirror state's lifetime, reported in the 1998 Evaluation [38]. Finally, for the states with $E_x = 6700 - 6800$ keV, their properties reported in refs. [29, 107] are adopted, and spins are matched where known to those reported in the latest evaluation [40]. Since the present measurement reported B_p values with large uncertainties arising from subtracted contaminant peaks in the singles spectrum at this E_x range, the B_p values reported by Wrede *et al.* [29] were adopted.

Figure 5.1 shows the ^{30}P(p,γ)^{31}S resonant rate arising from states with the properties listed in Table 5.1, and Table 5.2 lists the contribution from the updated B_p measured for the E_x = 6.636-MeV resonance in this work alongside the total resonant reaction rate. The E_x = 6.636-MeV resonance is observed to not contribute significantly to the total resonant reaction rate even when its measured B_p value is varied within the full range of its uncertainty. This behavior is consistent with this resonance's larger L value (which causes a higher centrifugal barrier to proton capture) and location in the tail of the Gamow peak at temperatures relevant to nova nucleosynthesis. We remark here, in passing, that sensitivity studies on single-zone Type-I X-ray burst models such as [108] have indicated a well-constrained ^{30}P(p,γ)^{31}S reaction rate at temperatures up to 2 GK to be important towards predicting the isotopic composition of the burst ashes. In particular, changing this reaction rate by a factor of 100 was found to change the isotopic composition of A = 31 elements in the burst ashes by a factor as high as 3. Even though the present reaction rate uncertainty has not been identified as the most significant source of uncertainty in the simulated burst ash composition, the updated reaction rate could have a significant impact

in future work on results from these models, if the contributions from states with $E_x > 6.7$ MeV are accounted for. To estimate the reaction rate at higher temperatures than shown in Figure 5.1, measured properties of states with larger E_x values than those included in Table 5.1 would be necessary. B_p measurements such as those performed in this work and in other recent efforts [49, 29], as well as better constraints on the spins and γ-ray widths of these states would be important towards achieving this end.

To summarize, the present measurement shows broad agreement with several previous proton-branching ratio measurements using transfer reactions. In many cases, the comparatively high amount of statistics gathered here permit us to improve upon the precision of B_p of several states. The independently determined normalization factor for the branching-ratios was in agreement between the two reactions studied. Decay protons from the E_x = 6.636-MeV state were detected for the first time using SABRE, as were decay protons from states on the highest end of the excitation energy range in ^{31}S. The key scope for improvement in the current measurement is the minimization of contaminants in the target that can be accomplished by using an enriched self-supporting Si-28 target, which minimizes the presence of both ^{12}C and ^{16}O, which were observed to interfere with the recorded ^{31}S spectrum at several positions. Such a study will be beneficial towards systematically exploring proton branching from states even closer to the proton threshold assuming sufficiently low electronic noise in the setup, since this would help limit the contaminant peaks from ^{16}O(^{6}Li,t)^{19}Ne populating states at $E_x(^{19}\text{Ne})$ = 1.51, 1.54 and 1.62 MeV immediately next to the E_x = 6.636-MeV resonance.

Experimental determination of the proton-branching ratios of many of these states in the Gamow window, especially for those with low L values, would serve to improve the precision of the estimated reaction rate. In addition, systematic uncertainties associated with the focal plane detector's position detection, and the loss of resolution arising from the use of a comparatively thick target and larger entrance aperture to the spectrograph can also be addressed by a longer experimental campaign. Another important consideration for future

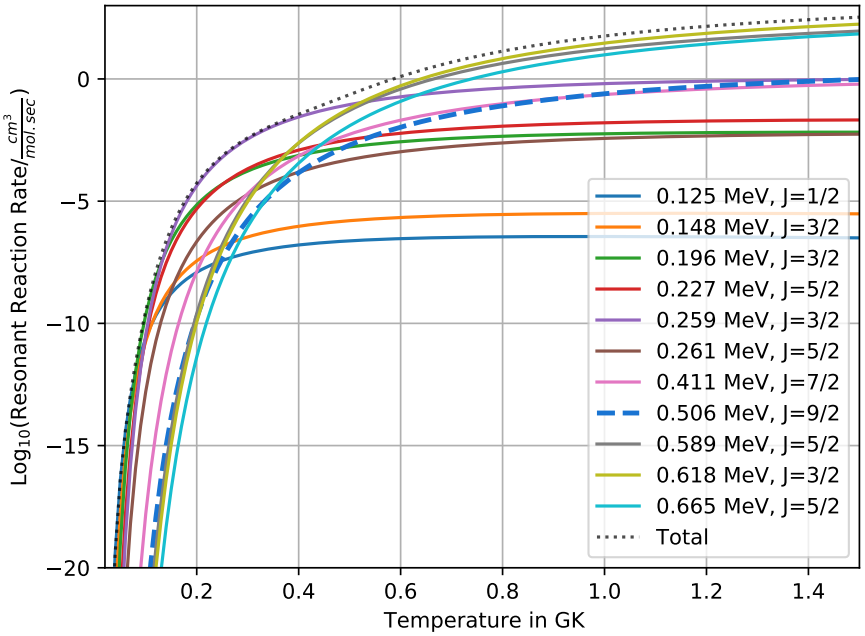

Figure 5.1. Resonant contribution to the ^{30}P(p,γ)^{31}S reaction rate due to all states in Table 5.1. Contribution from the resonance at $E_x(^{31}\mathrm{S}) = 6.636$ MeV measured in this work is highlighted as a blue dashed curve.

work could be a better constraint on the Γ_γ for states with $E_x = 6.636$ MeV and above, that improve from the current estimates using lifetime measurements only in a few cases. More generally, the cross-section observed for the (^{6}Li,t) reaction on the order of several μb/sr is comparable to that observed in more commonly used charge-exchange reactions like (^{3}He,t), which makes it another arrow in the quiver that could prove useful towards studying resonances in proton-rich nuclei away from stability.

Table 5.1. Properties of states in ^{31}S adopted to calculate the resonant reaction rates in Fig. 5.1, and Table 5.2.

E_x[40] keV	E_{res} keV	L	J	(Γ_p/Γ)	Γ_γ eV	$\omega\gamma$ keV
6255.3	125	0	1/2			9.5×10^{-15} [107]
6279	148	0	3/2			1.387×10^{-13} [107]
6327	196	1	3/2			3.607×10^{-10} [51]
6357.3	227	1	5/2			$\leq 1.4 \times 10^{-9}$ [51]
6390	259	0	3/2	0.00025 [63]	4.90×10^{-4} [63]	8.161×10^{-8} [63]
6392	261	2	5/2			4.8×10^{-10} [51]
6541.9	411	2	7/2			1.7×10^{-7} [51]
6636.8	506	3	9/2	0.10[1]	3.30×10^{-6} [47]	6.05×10^{-7}
6720	589	2	5/2 [40]	0.25 [29]	4.00×10^{-4} [107]	1.0×10^{-4}
6749	618	0	3/2 [40]	0.57 [29]	6.30×10^{-4} [107]	2.39×10^{-4}
6796	665	2	5/2 [29]	0.6875 [29]	2.00×10^{-4} [29]	1.38×10^{-4}

[1] This work

Table 5.2. Resonant contribution to the ^{30}P(p,γ)^{31}S reaction rate from the $E_x = 6.636$-MeV state observed in the current measurement, and the total evaluated reaction rate assuming states with properties listed in Table 5.1.

Temperature GK	Contribution from $E_x = 6.636$ MeV cm^3/(mol.sec)	Total Resonant Rate cm^3/(mol.sec)
0.1	8.67E-23	3.30E-10
0.15	1.50E-14	7.77E-07
0.2	1.74E-10	5.47E-05
0.25	4.42E-08	7.19E-04
0.3	1.68E-06	3.94E-03
0.35	2.19E-05	1.34E-02
0.4	1.46E-04	3.60E-02
0.45	6.26E-04	9.12E-02
0.5	1.97E-03	0.23
0.55	4.97E-03	0.56
0.6	1.06E-02	1.26
0.65	0.02	2.59
0.7	0.03	4.88
0.75	0.05	8.47
0.80	0.08	13.73
0.85	0.11	20.99
0.90	0.15	30.54
0.95	0.20	42.59
1	0.25	57.29
1.1	0.37	94.84
1.2	0.50	142.95
1.3	0.65	200.53
1.4	0.80	266.00

Appendix A. .Kinematic and Tilt Correction in the SE-SPS Focal Plane Detector

As discussed in Chapters 2 and 3, the focal plane detector in the SE-SPS is designed to perform charged-particle position detection over two parallel planes, with values x_1 and x_2. Knowledge of particle position over these two planes can be used to identify the particle's trajectory in every event, which can in turn be used to identify the plane of maximum focus, or the true focal plane of the reaction. The position along this true focal plane is labeled in the text as x_{avg}. Figure A.1 sketches the geometry of the focal plane detector, and indicates the locus of the true focal plane as a blue dotted line. In performing this analysis, we borrow the same convention followed by Shapira *et al.* [109]. By using the known geometric separation S between the two planes and modeling the true focal plane as a line in the same plane as x_1 and x_2, one can determine the parameters (H,α) of the line's equation

$$\frac{1}{1+ctg^2\alpha}x + \frac{1}{1+tg^2\alpha}y - H = 0 \tag{A.1}$$

The point of intersection between the focal plane with the above parametrization and a particle detected at x_1 and x_2 in the front and back planes respectively, is derived by Shapira *et al.* as

$$x_F = \frac{Sx_2cos(\alpha') - H(x_2 - x_1)}{Scos(\alpha') - (x_2 - x_1)sin(\alpha')}, S > 0, 0 < \alpha' < 90^\circ \tag{A.2}$$

Once the position spectrum of the reaction of interest has been identified in the focal plane, one can plot particle trajectories in a family of planes parallel to the front and back planes by calculating Eq A.2 using trial values for H and α such as $0 <$ H $<$ S and $\alpha = 0$. The resulting 2D histogram that plots trial x_F values for different H' values and $\alpha = 0$ is shown for the ^{12}C(^{6}Li,α)^{14}N reaction in Fig. A.2(a). Here $H' = H/S$ is the normalized position of the trial plane between the two planes, with $H' = 0(1)$ corresponding to the back (front) plane. Corresponding to each state in this histogram is a diagonal pattern that

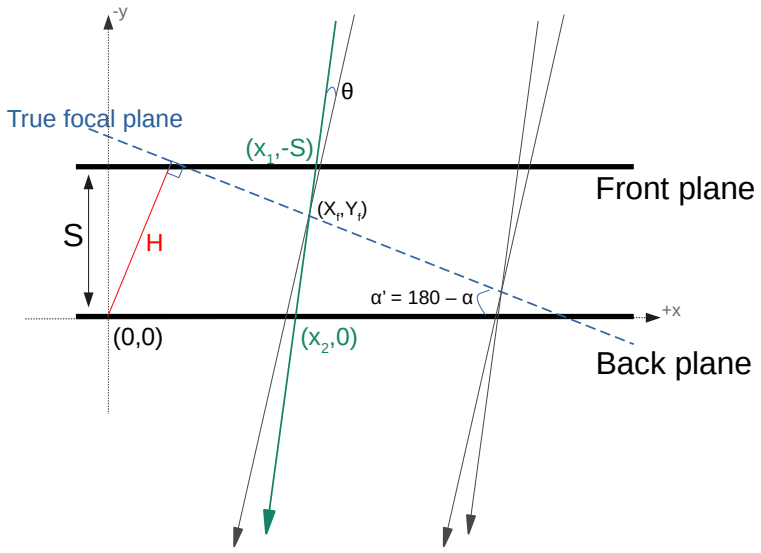

Figure A.1. Schematic diagram showing the position of the true focal plane (blue) with respect to the detection planes. The four arrows represent particle trajectories from the SE-SPS exit, with one of them highlighted in cyan to label its points of intersection with the two detection planes. Figure adapted from [109]. See text for details.

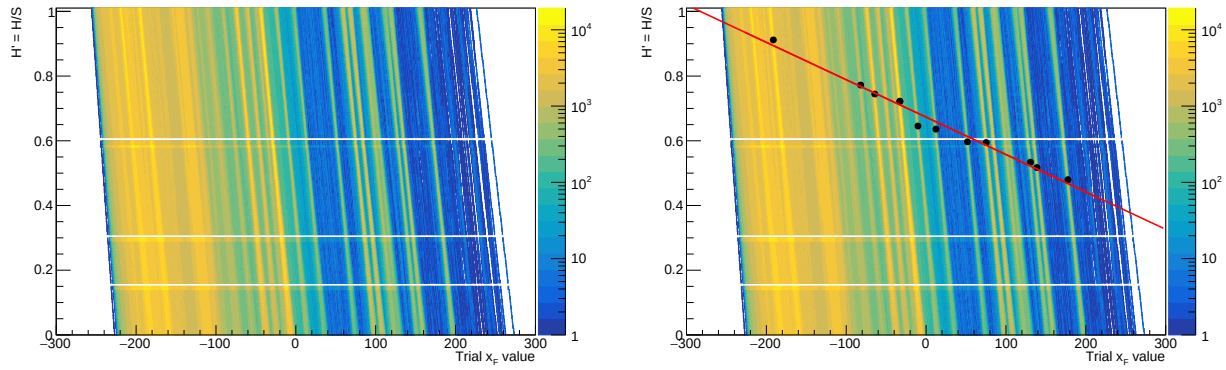

(a) (b)

Figure A.2. (Left) 2D Histogram plotting particle position x_F along different trial planes satisfying $\alpha = 0$ and $H = H'S$. Each diagonal pattern corresponds to a state populated in ^{12}C(^{6}Li,α)^{14}N, showing changes in focus as the particle traverses the focal plane. (Right) The same histogram on the left, overlaid with numerically evaluated positions of best focus (black circles) and the best-fit line passing through them (red) representing the estimated true focal plane.

changes its width over different H' values, coming to a minimum in each case between the two planes. This is the position of maximum focus for this state i.e. its position in the true focal plane. The focal plane equation in Eq A.1 is calculated by finding the equation to the line connecting the points of maximum focus across several isolated states through the length of the focal plane detector. The position x_F along this plane of maximum focus is labeled as x_{avg}, and is subsequently calibrated against the radius parameter ρ of the SE-SPS as discussed further in Chapter 3. Figure A.2(b) shows the positions of maximum focus identified for a few chosen states, and the best-fit line through them that is an estimate of the true focal plane. Typical parameters found in this experiment are $H = 28.8154$ mm, $\alpha' = 0.04951$ rad for the case indicated in A.2(b). We use $S = 42.8625$ mm as known from the detector's geometry.

Appendix B. .Integral of the Modified Crystal Ball Function

We have the modified Crystal Ball function suggested by S Das [103].

$$f(x;\mu,\sigma,k) = \begin{cases} \frac{A}{\sqrt{2\pi\sigma^2}} e^{-\frac{(x-\mu)^2}{2\sigma^2}}, x > \mu - k\sigma \\ \frac{A}{\sqrt{2\pi\sigma^2}} e^{\frac{k^2}{2}+\frac{k(x-\mu)}{\sigma}}, x \leq \mu - k\sigma \end{cases}$$

It has a simple exponential falloff after k standard deviations to the left of mean, and the remaining functional form is that of a gaussian. At the junction, the function takes the value $\sim\exp(-k^2/2)$.

When we integrate this over $-\infty$ to $+\infty$, we have:

$$\begin{aligned} \int_{-\infty}^{+\infty} f(t)dt = \int_{-\infty}^{\mu-k\sigma} \frac{A}{\sqrt{2\pi\sigma^2}} e^{\frac{k^2}{2}+\frac{k(t-\mu)}{\sigma}} dt + \int_{\mu-k\sigma}^{\infty} \frac{A}{\sqrt{2\pi\sigma^2}} e^{-\frac{(t-\mu)^2}{2\sigma^2}} dt \\ = (I) + (II) \end{aligned} \tag{B.1}$$

Let's evaluate these simple integrals..

$$\begin{aligned} (I) = \int_{-\infty}^{\mu-k\sigma} \frac{A}{\sqrt{2\pi\sigma^2}} e^{\frac{k^2}{2}+\frac{k(t-\mu)}{\sigma}} dt = \frac{Ae^{\frac{k^2}{2}}}{\sqrt{2\pi\sigma^2}} \left[e^{\frac{k(t-\mu)}{\sigma}} \frac{\sigma}{k} \right]_{t=-\infty}^{t=\mu-k\sigma} \\ = \frac{Ae^{\frac{k^2}{2}}}{\sqrt{2\pi\sigma^2}} \left[e^{\frac{k(\mu-k\sigma-\mu)}{\sigma}} * \frac{\sigma}{k} - e^{\frac{k(-\infty-\mu)}{\sigma}} \frac{\sigma}{k} \right] \\ = \frac{Ae^{\frac{k^2}{2}}}{\sqrt{2\pi\sigma^2}} \left[e^{-k^2} * \frac{\sigma}{k} - e^{\frac{k(-\infty-\mu)}{\sigma}} \frac{\sigma}{k} \right] \\ = \frac{Ae^{\frac{-k^2}{2}}}{\sqrt{2\pi k^2}} \end{aligned} \tag{B.2}$$

Now onto the more mysterious (II), we have

$$(II) = \int_{\mu-k\sigma}^{\infty} \frac{A}{\sqrt{2\pi\sigma^2}} e^{-\frac{(t-\mu)^2}{2\sigma^2}} dt$$

Making a variable transformation $s = (t-\mu)/\sqrt{2}\sigma$, we have $\sqrt{2}\sigma ds = dt$, and $t : \mu - k\sigma \rightarrow$

∞ becoming $s : -k/\sqrt{2} \to \infty$ i.e.

$$(II) = \int_{-k/\sqrt{2}}^{\infty} \frac{A\sqrt{2}\sigma}{\sqrt{2\pi}\sigma} e^{-s^2} ds$$
$$= \int_{-k/\sqrt{2}}^{\infty} \frac{A}{\sqrt{\pi}} e^{-s^2} ds = \frac{A}{\sqrt{2\pi}} \int_{-\infty}^{k} e^{-p^2/2} dp \tag{B.3}$$

where in the last step we make the substitution $p = -\sqrt{2}s$.

Now, we know from the definition of the Error function that

$$\mathrm{erf}(x) = \frac{2}{\sqrt{\pi}} \int_0^x e^{-t^2} dt$$
$$\implies \frac{1}{2}\left[1 + \mathrm{erf}\left(\frac{x}{\sqrt{2}}\right)\right] = \frac{1}{\sqrt{2\pi}} \int_{-\infty}^{x} e^{-t^2/2} dt \tag{B.4}$$

since

$$\frac{1}{\sqrt{2\pi}} \int_{-\infty}^{0} e^{-t^2/2} dt = \frac{1}{2} \tag{B.5}$$

Comparing (3) and (4), we get

$$(II) = \frac{A}{2}\left[1 + \mathrm{erf}\left(\frac{k}{\sqrt{2}}\right)\right] \tag{B.6}$$

which gives us the final answer,

$$\int_{-\infty}^{+\infty} f(t) dt = \frac{A e^{\frac{-k^2}{2}}}{\sqrt{2\pi k^2}} + \frac{A}{2}\left[1 + \mathrm{erf}\left(\frac{k}{\sqrt{2}}\right)\right] \tag{B.7}$$

which tends to the Gaussian integral A as $k \to \infty$, as expected. For finite k, the integral adds a correction to the Gaussian integral A by a function of k which is readily evaluable numerically. ROOT's TMath::Erf() was used to cast this integral as a parameter of the fit function, which also was able to provide uncertainties in this quantity during the χ^2 minimization process.

References

[1] Hans E. Suess and Harold C. Urey. Abundances of the Elements. *Rev. Mod. Phys.*, 28:53–74, Jan 1956. doi: 10.1103/RevModPhys.28.53.

[2] C.E. Rolfs, W.S. Rodney, and W.S. Rodney. *Cauldrons in the Cosmos: Nuclear Astrophysics*. Theoretical Astrophysics. University of Chicago Press, 1988. ISBN 9780226724577.

[3] E. Margaret Burbidge, G. R. Burbidge, William A. Fowler, and F. Hoyle. Synthesis of the Elements in Stars. *Rev. Mod. Phys.*, 29:547–650, Oct 1957. doi: 10.1103/RevModPhys.29.547.

[4] A. G. W. Cameron. On the Origin of the Heavy Elements. *The Astronomical Journal*, 62:9–10, 1957.

[5] A. G. W. Cameron. Nuclear Astrophysics. *Annual Review of Nuclear Science*, 8(1), 12 1958. ISSN 0066-4243. doi: 10.1146/annurev.ns.08.120158.001503.

[6] P. A. Denissenkov and F. D. A. Hartwick. Supermassive Stars as a Source of Abundance Anomalies of Proton-capture Elements in Globular Clusters. *Monthly Notices of the Royal Astronomical Society: Letters*, 437(1):L21–L25, 10 2013. ISSN 1745-3925. doi: 10.1093/mnrasl/slt133.

[7] Fred Hoyle. On Nuclear Reactions Occuring in Very Hot Stars. I. the Synthesis of Elements from Carbon to Nickel. *The Astrophysical Journal Supplement Series*, 1:121, 1954.

[8] George Wallerstein, Icko Iben, Peter Parker, Ann Merchant Boesgaard, Gerald M. Hale, Arthur E. Champagne, Charles A. Barnes, Franz Käppeler, Verne V. Smith, Robert D. Hoffman, Frank X. Timmes, Chris Sneden, Richard N. Boyd, Bradley S. Meyer, and David L. Lambert. Synthesis of the Elements in Stars: Forty Years of Progress. *Rev. Mod. Phys.*, 69:995–1084, Oct 1997. doi: 10.1103/RevModPhys.69.995.

[9] C.A. Bertulani and T. Kajino. Frontiers in Nuclear Astrophysics. *Progress in Particle and Nuclear Physics*, 89:56–100, 2016. ISSN 0146-6410. doi: https://doi.org/10.1016/j.ppnp.2016.04.001.

[10] Christian Iliadis. *Nuclear Physics of Stars*. John Wiley and Sons, 2015.

[11] Nikos Prantzos and Roland Diehl. Radioactive ^{26}Al in the Galaxy: Observations versus Theory. *Physics Reports*, 267(1):1–69, 1996. ISSN 0370-1573. doi: https://doi.org/10.1016/0370-1573(95)00055-0.

[12] Icko Iben Jr and Alvio Renzini. Asymptotic Giant Branch Evolution and Beyond. *Annual review of Astronomy and Astrophysics*, 21:271–342, 1983.

[13] M Arnould and K Takahashi. Nuclear Astrophysics. *Reports on Progress in Physics*, 62(3):395–462, jan 1999. doi: 10.1088/0034-4885/62/3/003.

[14] Jordi José, Margarita Hernanz, and Christian Iliadis. Nucleosynthesis in Classical Novae. *Nuclear Physics A*, 777:550–578, 2006.

[15] Public Domain Image. heasarc.gsfc.nasa.gov.

[16] Christian Iliadis, Art Champagne, Jordi Jose, Sumner Starrfield, and Paul Tupper. The Effects of Thermonuclear Reaction-Rate Variations on Nova Nucleosynthesis: A Sensitivity Study. *The Astrophysical Journal Supplement Series*, 142(1):105–137, sep 2002. doi: 10.1086/341400.

[17] A. L. Sallaska, C. Iliadis, A. E. Champange, S. Goriely, S. Starrfield, and F. X. Timmes. STARLIB: A Next-generation Reaction-rate Library For Nuclear Astrophysics. *The Astrophysical Journal Supplement Series*, 207(1):18, jul 2013. doi: 10.1088/0067-0049/207/1/18.

[18] Jordi Jose, Margarita Hernanz, Sachiko Amari, Katharina Lodders, and Ernst Zinner. The Imprint of Nova Nucleosynthesis in Presolar Grains. *The Astrophysical Journal*, 612(1):414–428, sep 2004. doi: 10.1086/422569.

[19] Lori N. Downen, Christian Iliadis, Jordi José, and Sumner Starrfield. Nuclear Thermometers For Classical Novae. *The Astrophysical Journal*, 762(2):105, dec 2012. doi: 10.1088/0004-637x/762/2/105.

[20] Keegan J. Kelly, Christian Iliadis, Lori Downen, Jordi José, and Art Champagne. Nuclear Mixing Meters For Classical Novae. *The Astrophysical Journal*, 777(2):130, oct 2013. doi: 10.1088/0004-637x/777/2/130.

[21] A. W. Shafter. The Galactic Nova Rate Revisited. *The Astrophysical Journal*, 834(2):196, jan 2017. doi: 10.3847/1538-4357/834/2/196.

[22] Donald D Clayton and Larry R Nittler. Astrophysics with Presolar Stardust. *Annu. Rev. Astron. Astrophys.*, 42:39–78, 2004.

[23] Donald D Clayton and Fred Hoyle. Grains of Anomalous Isotopic Composition from Novae. *The Astrophysical Journal*, 203:481–496, 1976.

[24] Sachiko Amari, Xia Gao, Larry R Nittler, Ernst Zinner, Jordi Jose, Margarita Hernanz, and Roy S Lewis. Presolar Grains from Novae. *The Astrophysical Journal*, 551(2):1065, 2001.

[25] Larry R Nittler and Peter Hoppe. Are Presolar Silicon Carbide Grains from Novae Actually from Supernovae? *The Astrophysical Journal*, 631(1):L89, 2005.

[26] Nan Liu, Larry R Nittler, Conel MO'D Alexander, Jianhua Wang, Marco Pignatari, Jordi José, and Ann Nguyen. Stellar Origins of Extremely ^{13}C and ^{15}N Enriched Presolar SiC Grains: Novae or Supernovae? *The Astrophysical Journal*, 820(2):140, 2016.

[27] A Parikh, K Wimmer, T Faestermann, Ralf Hertenberger, J José, H-F Wirth, C Hinke, R Krücken, D Seiler, K Steiger, et al. Isotopic $^{32}S/^{33}S$ Ratio as a Diagnostic of Presolar Grains from Novae. *Physics Letters B*, 737:314–319, 2014.

[28] Jordi Jose and Margarita Hernanz. Nucleosynthesis in Classical Novae: CO versus ONe White Dwarfs. *The Astrophysical Journal*, 494(2):680–690, feb 1998. doi: 10.1086/305244.

[29] C. Wrede, J. A. Caggiano, J. A. Clark, C. M. Deibel, A. Parikh, and P. D. Parker. Measurements of ^{31}S Energy Levels and Reevaluation of the Thermonuclear Resonant $^{30}P(p,\gamma)^{31}S$ Reaction Rate. *Phys. Rev. C*, 79:045803, Apr 2009. doi: 10.1103/PhysRevC.79.045803.

[30] S. Engel, D. Hutcheon, S. Bishop, L. Buchmann, J. Caggiano, M.L. Chatterjee, A.A. Chen, J. D'Auria, D. Gigliotti, U. Greife, D. Hunter, A. Hussein, C.C. Jewett, A.M. Laird, M. Lamey, W. Liu, A. Olin, D. Ottewell, J. Pearson, C. Ruiz, G. Ruprecht, M. Trinczek, C. Vockenhuber, and C. Wrede. Commissioning the DRAGON facility at ISAC. *Nuclear Instruments and Methods in Physics Research Section A: Accelerators, Spectrometers, Detectors and Associated Equipment*, 553(3):491–500, 2005. ISSN 0168-9002. doi: https://doi.org/10.1016/j.nima.2005.07.029.

[31] G. Bollen. FRIB—Facility for Rare Isotope Beams. *AIP Conference Proceedings*, 1224 (1):432–441, 2010. doi: 10.1063/1.3431449.

[32] GPA Berg, DW Bardayan, JC Blackmon, KA Chipps, M Couder, U Greife, U Hager, F Montes, KE Rehm, H Schatz, et al. A Recoil Separator for Nuclear Astrophysics SECAR. *Nuclear Instruments and Methods in Physics Research Section B: Beam Interactions with Materials and Atoms*, 376:165–167, 2016.

[33] H. A. Bethe. Nuclear Physics B. Nuclear Dynamics, Theoretical. *Rev. Mod. Phys.*, 9: 69–244, Apr 1937. doi: 10.1103/RevModPhys.9.69.

[34] D W Bardayan. Transfer Reactions in Nuclear Astrophysics. *Journal of Physics G: Nuclear and Particle Physics*, 43(4):043001, feb 2016. doi: 10.1088/0954-3899/43/4/043001.

[35] C. Wrede. The $^{30}P(p,\gamma)^{31}S$ Reaction in Classical Novae: Progress and Prospects. *AIP Advances*, 4(4):041004, 2014. doi: 10.1063/1.4864193.

[36] P.M. Endt and C. Van Der Leun. Energy Levels of A = 21–44 Nuclei (VI). *Nuclear Physics A*, 310(1):1–751, 1978. ISSN 0375-9474. doi: https://doi.org/10.1016/0375-9474(78)90611-5.

[37] P.M. Endt. Energy Levels of A = 21–44 Nuclei (VII). *Nuclear Physics A*, 521:1–400, 1990. ISSN 0375-9474. doi: https://doi.org/10.1016/0375-9474(90)90598-G.

[38] P.M. Endt. Supplement to Energy Levels of A = 21–44 Nuclei (VII). *Nuclear Physics A*, 633(1):1–220, 1998. ISSN 0375-9474. doi: https://doi.org/10.1016/S0375-9474(97)00613-1.

[39] Christian Ouellet and Balraj Singh. Nuclear Data Sheets for A=31. *Nuclear Data Sheets*, 114(2):209–396, 2013. ISSN 0090-3752. doi: https://doi.org/10.1016/j.nds.2013.03.001.

[40] Jun Chen and Balraj Singh. Nuclear Structure and Decay Data for A=31 Isobars. *Nuclear Data Sheets*, 184:29–405, 2022. ISSN 0090-3752. doi: https://doi.org/10.1016/j.nds.2022.08.002.

[41] Z. Ma, D. W. Bardayan, J. C. Blackmon, R. P. Fitzgerald, M. W. Guidry, W. R. Hix, K. L. Jones, R. L. Kozub, R. J. Livesay, M. S. Smith, J. S. Thomas, and D. W. Visser. Astrophysically Important ^{31}S States Studied with the ^{32}S$(p,d)^{31}$S Reaction. *Phys. Rev. C*, 76:015803, Jul 2007. doi: 10.1103/PhysRevC.76.015803.

[42] K. Setoodehnia, A. A. Chen, J. Chen, J. A. Clark, C. M. Deibel, J. Hendriks, D. Kahl, W. N. Lennard, P. D. Parker, D. Seiler, and C. Wrede. Level Structure of ^{31}S via ^{32}S$(p,d)^{31}$S. *Phys. Rev. C*, 102:045806, Oct 2020. doi: 10.1103/PhysRevC.102.045806.

[43] D. Irvine, A. A. Chen, A. Parikh, K. Setoodehnia, T. Faestermann, R. Hertenberger, H.-F. Wirth, V. Bildstein, S. Bishop, J. A. Clark, C. M. Deibel, J. Hendriks, C. Herlitzius, R. Krücken, W. N. Lennard, O. Lepyoshkina, R. Longland, G. Rugel, D. Seiler, K. Straub, and C. Wrede. Evidence for the Existence of the Astrophysically Important 6.40-MeV State of ^{31}S. *Phys. Rev. C*, 88:055803, Nov 2013. doi: 10.1103/PhysRevC.88.055803.

[44] J. Vernotte, G. Berrier-Ronsin, S. Fortier, E. Hourani, A. Khendriche, J.M. Maison, L.-H. Rosier, G. Rotbard, E. Caurier, and F. Nowacki. One-nucleon Pickup Reactions on ^{32}S: Experimental Results and Shell-model Calculations. *Nuclear Physics A*, 655(3): 415–439, 1999. ISSN 0375-9474. doi: https://doi.org/10.1016/S0375-9474(99)00301-2.

[45] H. Nann and B. H. Wildenthal. (p,t) and $(p,^3\mathrm{He})$ Reactions on ^{33}S. *Phys. Rev. C*, 19: 2146–2154, Jun 1979. doi: 10.1103/PhysRevC.19.2146.

[46] A. Parikh, K. Wimmer, T. Faestermann, R. Hertenberger, J. José, R. Longland, H.-F. Wirth, V. Bildstein, S. Bishop, A. A. Chen, J. A. Clark, C. M. Deibel, C. Herlitzius, R. Krücken, D. Seiler, K. Straub, and C. Wrede. Improving the ^{30}P$(p,\gamma)^{31}$S Rate in Oxygen-Neon novae: Constraints on J^π Values for Proton-threshold States in ^{31}S. *Phys. Rev. C*, 83:045806, Apr 2011. doi: 10.1103/PhysRevC.83.045806.

[47] C. Wrede, J. A. Caggiano, J. A. Clark, C. Deibel, A. Parikh, and P. D. Parker. New ^{30}P$(p,\gamma)^{31}$S Resonances and Oxygen-Neon Nova Nucleosynthesis. *Phys. Rev. C*, 76: 052802, Nov 2007. doi: 10.1103/PhysRevC.76.052802.

[48] Ian J Thompson. Coupled Reaction Channels Calculations in Nuclear Physics. *Computer Physics Reports*, 7(4):167–212, 1988.

[49] S. Burcher, K. A. Chipps, R. O. Hughes, C. S. Reingold, A. Saastamoinen, J. T. Harke, N. Cooper, S. Ahn, J. M. Allmond, H. Clark, J. A. Cizewski, M. R. Hall, J. Hooker, H. Jayatissa, K. L. Jones, S. Ota, S. D. Pain, K. Schmidt, A. Simon,

and S. Upadhyayula. Developing the ^{32}S$(p,d)^{31}$S$^{*}(p)(\gamma)$ Reaction To Probe The ^{30}P$(p,\gamma)^{31}$S Reaction Rate in Classical Novae. *Phys. Rev. C*, 105:045805, Apr 2022. doi: 10.1103/PhysRevC.105.045805.

[50] R.O. Hughes, J.T. Harke, R.J. Casperson, S. Ota, S. Fisher, J. Parker, C.W. Beausang, M. Dag, P. Humby, J. Koglin, E. McCleskey, A.B. McIntosh, A. Saastamoinen, A.S. Tamashiro, E. Wilson, and T.C. Wu. The Hyperion Particle-γ Detector Array. *Nuclear Instruments and Methods in Physics Research Section A: Accelerators, Spectrometers, Detectors and Associated Equipment*, 856:47–52, 2017. ISSN 0168-9002. doi: https://doi.org/10.1016/j.nima.2017.03.012.

[51] A. Kankainen, P.J. Woods, H. Schatz, T. Poxon-Pearson, D.T. Doherty, V. Bader, T. Baugher, D. Bazin, B.A. Brown, J. Browne, A. Estrade, A. Gade, J. José, A. Kontos, C. Langer, G. Lotay, Z. Meisel, F. Montes, S. Noji, F. Nunes, G. Perdikakis, J. Pereira, F. Recchia, T. Redpath, R. Stroberg, M. Scott, D. Seweryniak, J. Stevens, D. Weisshaar, K. Wimmer, and R. Zegers. Measurement of Key Resonance States for the ^{30}P$(p,\gamma)^{31}$S Reaction Rate, and the Production of Intermediate-mass Elements in Nova Explosions. *Physics Letters B*, 769:549–553, 2017. ISSN 0370-2693. doi: https://doi.org/10.1016/j.physletb.2017.01.084.

[52] D. Tonev, G. de Angelis, I. Deloncle, N. Goutev, G. De Gregorio, P. Pavlov, I.L. Pantaleev, S. Iliev, M.S. Yavahchova, P.G. Bizzeti, A. Demerdjiev, D.T. Dimitrov, E. Farnea, A. Gadea, E. Geleva, C.Y. He, H. Laftchiev, S.M. Lenzi, S. Lunardi, N. Marginean, R. Menegazzo, D.R. Napoli, F. Nowacki, R. Orlandi, H. Penttilä, F. Recchia, E. Sahin, R.P. Singh, M. Stoyanova, C.A. Ur, and H.-F. Wirth. Transition Probabilities in ^{31}P and ^{31}S: A test for Isospin Symmetry. *Physics Letters B*, 821:136603, 2021. ISSN 0370-2693. doi: https://doi.org/10.1016/j.physletb.2021.136603.

[53] N. S. Pattabiraman, D. G. Jenkins, M. A. Bentley, R. Wadsworth, C. J. Lister, M. P. Carpenter, R. V. F. Janssens, T. L. Khoo, T. Lauritsen, D. Seweryniak, S. Zhu, G. Lotay, P. J. Woods, Krishichayan, and P. Van Isacker. Analog $E1$ Transitions and Isospin Mixing. *Phys. Rev. C*, 78:024301, Aug 2008. doi: 10.1103/PhysRevC.78.024301.

[54] D. G. Jenkins, A. Meadowcroft, C. J. Lister, M. P. Carpenter, P. Chowdhury, N. J. Hammond, R. V. F. Janssens, T. L. Khoo, T. Lauritsen, D. Seweryniak, T. Davinson, P. J. Woods, A. Jokinen, H. Penttila, G. Martínez-Pinedo, and J. José. Reevaluation of the ^{30}P$(p,\gamma)^{31}$S Astrophysical Reaction Rate from a Study of the $T = 1/2$ Mirror Nuclei, ^{31}S and ^{31}P. *Phys. Rev. C*, 73:065802, Jun 2006. doi: 10.1103/PhysRevC.73.065802.

[55] D. A. Testov, A. Boso, S. M. Lenzi, F. Nowacki, F. Recchia, G. de Angelis, D. Bazzacco, G. Colucci, M. Cottini, F. Galtarossa, A. Goasduff, A. Gozzelino, K. Hadyńska-Klęk, G. Jaworski, P. R. John, S. Lunardi, R. Menegazzo, D. Mengoni, A. Mentana, V. Modamio, A. Nannini, D. R. Napoli, M. Palacz, M. Rocchini, M. Siciliano, and J. J. Valiente-Dobón. High-spin Intruder States in the Mirror Nuclei ^{31}S and ^{31}P. *Phys. Rev. C*, 104:024309, Aug 2021. doi: 10.1103/PhysRevC.104.024309.

[56] F. Della Vedova, S. M. Lenzi, M. Ionescu-Bujor, N. Mărginean, E. Farnea, M. Nespolo, G. de Angelis, M. Axiotis, D. Bazzacco, A. Bizzeti-Sona, P. G. Bizzeti, F. Brandolini, D. Bucurescu, A. Iordachescu, S. Lunardi, R. Menegazzo, D. R. Napoli, C. Rossi Alvarez, and C. A. Ur. Isospin Symmetry Along The N=Z Line In The sd Shell. *AIP Conference Proceedings*, 764(1):205–210, 2005. doi: 10.1063/1.1905312.

[57] J.M. Davidson, D.A. Hutcheon, D.R. Gill, T. Taylor, D.M. Sheppard, and W.C. Olsen. Energy Levels of ^{31}S. *Nuclear Physics A*, 240(2):253–262, 1975. ISSN 0375-9474. doi: https://doi.org/10.1016/0375-9474(75)90329-2.

[58] D. T. Doherty, P. J. Woods, G. Lotay, D. Seweryniak, M. P. Carpenter, C. J. Chiara, H. M. David, R. V. F. Janssens, L. Trache, and S. Zhu. Level Structure of ^{31}S: From Low Excitation Energies to the Region of Interest for Hydrogen Burning in Novae Through the ^{30}P$(p,\gamma)^{31}$S Reaction. *Phys. Rev. C*, 89:045804, Apr 2014. doi: 10.1103/PhysRevC.89.045804.

[59] Kankainen A., Eronen T., Fox S. P., Fynbo H. O. U., Hager U., Hakala J., Huikari J., Jenkins D. G., Jokinen A., Kopecky S., Moore I., Nieminen A., Penttilä H., Rinta-Antila S., Tengblad O., Wang Y., , and Äystö J. Excited States in ^{31}S Studied via Beta Decay of ^{31}Cl. *The European Physical Journal A - Hadrons and Nuclei*, 27:67–75, 2006. ISSN 1434-601X.

[60] M. B. Bennett, C. Wrede, B. A. Brown, S. N. Liddick, D. Pérez-Loureiro, D. W. Bardayan, A. A. Chen, K. A. Chipps, C. Fry, B. E. Glassman, C. Langer, N. R. Larson, E. I. McNeice, Z. Meisel, W. Ong, P. D. O'Malley, S. D. Pain, C. J. Prokop, H. Schatz, S. B. Schwartz, S. Suchyta, P. Thompson, M. Walters, and X. Xu. Isospin Mixing Reveals ^{30}P$(p,\gamma)^{31}$S Resonance Influencing Nova Nucleosynthesis. *Phys. Rev. Lett.*, 116:102502, Mar 2016. doi: 10.1103/PhysRevLett.116.102502.

[61] M. B. Bennett, C. Wrede, B. A. Brown, S. N. Liddick, D. Pérez-Loureiro, D. W. Bardayan, A. A. Chen, K. A. Chipps, C. Fry, B. E. Glassman, C. Langer, N. R. Larson, E. I. McNeice, Z. Meisel, W. Ong, P. D. O'Malley, S. D. Pain, C. J. Prokop, S. B. Schwartz, S. Suchyta, P. Thompson, M. Walters, and X. Xu. Isobaric Multiplet Mass Equation in the $A = 31$, $T = 3/2$ Quartets. *Phys. Rev. C*, 93:064310, Jun 2016. doi: 10.1103/PhysRevC.93.064310.

[62] M. B. Bennett, C. Wrede, S. N. Liddick, D. Pérez-Loureiro, D. W. Bardayan, B. A. Brown, A. A. Chen, K. A. Chipps, C. Fry, B. E. Glassman, C. Langer, N. R. Larson, E. I. McNeice, Z. Meisel, W. Ong, P. D. O'Malley, S. D. Pain, C. J. Prokop, H. Schatz, S. B. Schwartz, S. Suchyta, P. Thompson, M. Walters, and X. Xu. Detailed Study of the Decay ^{31}Cl$(\beta\gamma)^{31}$S. *Phys. Rev. C*, 97:065803, Jun 2018. doi: 10.1103/PhysRevC.97.065803.

[63] T. Budner, M. Friedman, C. Wrede, B. A. Brown, J. José, D. Pérez-Loureiro, L. J. Sun, J. Surbrook, Y. Ayyad, D. W. Bardayan, K. Chae, A. A. Chen, K. A. Chipps, M. Cortesi, B. Glassman, M. R. Hall, M. Janasik, J. Liang, P. O'Malley, E. Pollacco, A. Psaltis, J. Stomps, and T. Wheeler. Constraining the ^{30}P$(p,\ \gamma)^{31}$S Reaction Rate

in ONe Novae via the Weak, Low-Energy, β-Delayed Proton Decay of ^{31}Cl. *Phys. Rev. Lett.*, 128:182701, May 2022. doi: 10.1103/PhysRevLett.128.182701.

[64] M. Friedman, D. Pérez-Loureiro, T. Budner, E. Pollacco, C. Wrede, M. Cortesi, C. Fry, B. Glassman, M. Harris, J. Heideman, M. Janasik, B.T. Roeder, M. Roosa, A. Saastamoinen, J. Stomps, J. Surbrook, P. Tiwari, and J. Yurkon. GADGET: a Gaseous Detector with Germanium Tagging. *Nuclear Instruments and Methods in Physics Research Section A: Accelerators, Spectrometers, Detectors and Associated Equipment*, 940:93–102, 2019. ISSN 0168-9002. doi: https://doi.org/10.1016/j.nima.2019.05.100.

[65] C. Iliadis. Proton Single-particle Reduced Widths for Unbound States. *Nuclear Physics A*, 618(1):166–175, 1997. ISSN 0375-9474. doi: https://doi.org/10.1016/S0375-9474(97)00065-1.

[66] C. W. Woods, Nelson Stein, and J. W. Sunier. (^{6}Li, t) Reaction on Medium-mass Nuclei and the Mass and Spectrum of ^{61}Zn. *Phys. Rev. C*, 17:66–74, Jan 1978. doi: 10.1103/PhysRevC.17.66.

[67] J.G. Pronko and R.A. Lindgren. Angular Correlations of Sequential Particle Decay for Aligned Nuclei. *Nuclear Instruments and Methods*, 98(3):445–449, 1972. ISSN 0029-554X. doi: https://doi.org/10.1016/0029-554X(72)90226-1.

[68] E.C. Good, B. Sudarsan, K.T. Macon, C.M. Deibel, L.T. Baby, J.C. Blackmon, C. Benetti, J.C. Esparza, N. Gerken, K. Hanselman, G.W. McCann, A.B. Morelock, J.F. Perello, K.H. Pham, E. Rubino, E. Temanson, and I. Wiedenhöver. SABRE: The Silicon Array for Branching Ratio Experiments. *Nuclear Instruments and Methods in Physics Research Section A: Accelerators, Spectrometers, Detectors and Associated Equipment*, 1003:165299, 2021. ISSN 0168-9002. doi: https://doi.org/10.1016/j.nima.2021.165299.

[69] S E Hunt. The Development and Application of the Van de Graaff Accelerator. *Physics Education*, 2(3):140–145, may 1967. doi: 10.1088/0031-9120/2/3/304.

[70] W. T. Diamond, Y. Imahori, J. W. McKay, J. S. C. Wills, and H. Schmeing. Efficient Negative-ion Sources for Tandem Injection (invited). *Review of Scientific Instruments*, 67(3):1404–1409, 1996. doi: 10.1063/1.1146648.

[71] L.G. Christophorou, J.K. Olthoff, and R.J. Van Brunt. Sulfur Hexafluoride and the Electric Power Industry. *IEEE Electrical Insulation Magazine*, 13(5):20–24, 1997. doi: 10.1109/57.620514.

[72] FSU John D. Fox Laboratory Website. https://fsunuc.physics.fsu.edu. Access date: 10 Oct 2022.

[73] J.E. Spencer and H.A. Enge. Split-pole Magnetic Spectrograph for Precision Nuclear Spectroscopy. *Nuclear Instruments and Methods*, 49(2):181–193, 1967. ISSN 0029-554X. doi: https://doi.org/10.1016/0029-554X(67)90684-2.

[74] Harald A. Enge. Magnetic Spectrographs for Nuclear Reaction Studies. *Nuclear Instruments and Methods*, 162(1):161–180, 1979. ISSN 0029-554X. doi: https://doi.org/10.1016/0029-554X(79)90711-0.

[75] Catherine M. Deibel. Nuclear Astrophysics Prospects with the Yale Enge Splt-Pole Spectrograph at Florida State University, 2014. ARUNA Users Meeting.

[76] Catherine M. Deibel. *The $^{26m}Al(p,\gamma)^{27}Si$ Reaction Rate in ONe Novae*. Ph. D. Thesis, Yale University, 2008.

[77] Glenn F. Knoll. *Radiation Detection and Measurement*. John Wiley and Sons, 2000.

[78] Ted Roussaville. Tedector User's Manual. 2004.

[79] Advanced Measurement Technology Inc. ORTEC Model 113 Scintillation Preamplifier Manual. https://www.ortec-online.com/-/media/ametekortec/manuals/1/113-mnl.pdf, . Access Date: 13 Oct 2022.

[80] Mirion Technologies. Canberra/mirion 2003-BT Silcon Detector Preamplifier Datasheet. https://www.mirion.com/products/2003bt-silicon-detector-preamplifier. Access date: 13 Oct 2022.

[81] Advanced Measurement Technology Inc. ORTEC Model 474 Timing Filter Amplifier Operating And Service Manual. https://www.ortec-online.com/-/media/ametekortec/manuals/4/474-mnl.pdf, . Access date: 13 Oct 2022.

[82] Advanced Measurement Technology Inc. ORTEC Model VT120 Fast Timing Preamplifier Operating And Service Manual. https://www.ortec-online.com/-/media/ametekortec/manuals/v/vt120-mnl.pdf, . Access date: 13 Oct 2022.

[83] O.B. Tarasov and D. Bazin. Lise++: Radioactive Beam Production with In-flight Separators. *Nuclear Instruments and Methods in Physics Research Section B: Beam Interactions with Materials and Atoms*, 266(19):4657–4664, 2008. ISSN 0168-583X. doi: https://doi.org/10.1016/j.nimb.2008.05.110. Proceedings of the XVth International Conference on Electromagnetic Isotope Separators and Techniques Related to their Applications.

[84] E. Koshchiy, J.C. Blackmon, G.V. Rogachev, I. Wiedenhöver, L. Baby, P. Barber, D.W. Bardayan, J. Belarge, D. Caussyn, E.D. Johnson, K. Kemper, A.N. Kuchera, L.E. Linhardt, K.T. Macon, M. Matoš, B.S. Rasco, and D. Santiago-Gonzalez. ANASEN: The Array for Nuclear Astrophysics and Structure with Exotic Nuclei. *Nuclear Instruments and Methods in Physics Research Section A: Accelerators, Spectrometers, Detectors and Associated Equipment*, 870:1–11, 2017. ISSN 0168-9002. doi: https://doi.org/10.1016/j.nima.2017.07.030.

[85] B Davin, R.T de Souza, R Yanez, Y Larochelle, R Alfaro, H.S Xu, A Alexander, K Bastin, L Beaulieu, J Dorsett, G Fleener, L Gelovani, T Lefort, J Poehlman, R.J Charity, L.G Sobotka, J Elson, A Wagner, T.X Liu, X.D Liu, W.G Lynch, L Morris,

R Shomin, W.P Tan, M.B Tsang, G Verde, and J Yurkon. LASSA: A Large Area Silicon Strip Array for Isotopic Identification of Charged Particles. *Nuclear Instruments and Methods in Physics Research Section A: Accelerators, Spectrometers, Detectors and Associated Equipment*, 473(3):302–318, 2001. ISSN 0168-9002. doi: https://doi.org/10.1016/S0168-9002(01)00295-9.

[86] Mesytec GmbH. MDU-16 Datasheet. https://www.mesytec.com/products/datasheets/MDU-16.pdf. Access date: 13 Oct 2022.

[87] Erin C. Good. *A Study of $^{26m}Al(p,\gamma)^{27}Si$ with the Silicon Array for Branching Ratio Experiments (SABRE)*. Ph. D. Thesis, Louisiana State University, 2020.

[88] Krzysztof T Pozniak. FPGA-based, Specialized Trigger and Data Acquisition Systems for High-energy Physics Experiments. *Measurement Science and Technology*, 21(6): 062002, apr 2010. doi: 10.1088/0957-0233/21/6/062002.

[89] Krzysztof Iniewski. *Embedded Systems : Hardware, Design, and Implementation.* John Wiley and Sons, Inc., 2013. ISBN 9781118468654.

[90] Valentin T. Jordanov and Glenn F. Knoll. Digital Synthesis of Pulse Shapes in Real Time for High Resolution Radiation Spectroscopy. *Nuclear Instruments and Methods in Physics Research Section A: Accelerators, Spectrometers, Detectors and Associated Equipment*, 345(2):337–345, 1994. ISSN 0168-9002. doi: https://doi.org/10.1016/0168-9002(94)91011-1.

[91] D. Cester, M. Lunardon, G. Nebbia, L. Stevanato, G. Viesti, S. Petrucci, and C. Tintori. Pulse Shape Discrimination with Fast Digitizers. *Nuclear Instruments and Methods in Physics Research Section A: Accelerators, Spectrometers, Detectors and Associated Equipment*, 748:33–38, 2014. ISSN 0168-9002. doi: https://doi.org/10.1016/j.nima.2014.02.032.

[92] AN3250 : Pulse Shape Discrimination with Different CAEN Digitizers Running DPP-PSD Firmware. http://www.caen.it, 2014. Accessed: 08 Oct 2022.

[93] CoMPASS Quick Start: GD6300 rev 20, CoMPASS User Manual:UM5960 Rev 20. http://www.caen.it, 2019. Accessed: 08 Oct 2022.

[94] NSCLDAQ Online Reference. http://docs.nscl.msu.edu/daq/index.php. Access date: 08 Oct 2022.

[95] CAEN Digitizer Library User Manual : UM1935 Rev 22. http://www.caen.it, 2019. Accessed: 08 Oct 2022.

[96] John K Ousterhout et al. *Tcl: An Embeddable Command Language*. Citeseer, 1989.

[97] I. Antcheva, M. Ballintijn, B. Bellenot, M. Biskup, R. Brun, N. Buncic, Ph. Canal, D. Casadei, O. Couet, V. Fine, L. Franco, G. Ganis, A. Gheata, D. Gonzalez Maline, M. Goto, J. Iwaszkiewicz, A. Kreshuk, D. Marcos Segura, R. Maunder, L. Moneta, A. Naumann, E. Offermann, V. Onuchin, S. Panacek, F. Rademakers, P. Russo, and

M. Tadel. ROOT — A C++ Framework for Petabyte Data Storage, Statistical Analysis and Visualization. *Computer Physics Communications*, 182(6):1384–1385, 2011. ISSN 0010-4655. doi: https://doi.org/10.1016/j.cpc.2011.02.008.

[98] CAEN 1730 and 1725 User Manual. http://www.caen.it, 2019. Accessed: 08 Oct 2022.

[99] GD2827 - How to Make Coincidences with CAEN Digitizers, User Guide rev. 3. http://www.caen.it, 2017. Accessed: 10 Oct 2022.

[100] Dale William Visser. *Particle Decay Branching Ratios for States of Astrophysical Importance in ^{19}Ne*. Ph. D. Thesis, Yale University, 2003.

[101] M. Reese, J. Gerl, P. Golubev, and N. Pietralla. Automatic Intrinsic Calibration of Double-sided Silicon Strip Detectors. *Nuclear Instruments and Methods in Physics Research Section A: Accelerators, Spectrometers, Detectors and Associated Equipment*, 779:63–68, 2015. ISSN 0168-9002. doi: https://doi.org/10.1016/j.nima.2015.01.032.

[102] D. Martínez Santos and F. Dupertuis. Mass Distributions Marginalized over Per-event Errors. *Nuclear Instruments and Methods in Physics Research Section A: Accelerators, Spectrometers, Detectors and Associated Equipment*, 764:150–155, 2014. ISSN 0168-9002. doi: https://doi.org/10.1016/j.nima.2014.06.081.

[103] Souvik Das. A Simple Alternative to the Crystal Ball Function. *arXiv preprint arXiv:1603.08591*, 2016.

[104] Christopher L. H. Wrede. *Nuclear Energy Levels of Sulfur-31 and Astrophysical Implications*. PhD thesis, 2008.

[105] F Ajzenberg-Selove. Energy Levels of Light Nuclei A=14. *Nucl. Phys*, 523:1, 1991.

[106] M. Kamil, S. Triambak, G. C. Ball, V. Bildstein, A. Diaz Varela, T. Faestermann, P. E. Garrett, F. Ghazi Moradi, R. Hertenberger, N. Y. Kheswa, N. J. Mukwevho, B. M. Rebeiro, and H.-F. Wirth. Proton Capture on ^{30}P in Novae: On the Existence of States at 6.40 MeV and 6.65 MeV in ^{31}S. *Phys. Rev. C*, 105:055805, May 2022. doi: 10.1103/PhysRevC.105.055805.

[107] B. Alex Brown, W. A. Richter, and C. Wrede. Shell-model Studies of the Astrophysical Rapid-proton-capture Reaction $^{30}\mathrm{P}(p,\gamma)^{31}\mathrm{S}$. *Phys. Rev. C*, 89:062801, Jun 2014. doi: 10.1103/PhysRevC.89.062801.

[108] R. H. Cyburt, A. M. Amthor, A. Heger, E. Johnson, L. Keek, Z. Meisel, H. Schatz, and K. Smith. Dependence of X-ray Burst Models On Nuclear Reaction Rates. *The Astrophysical Journal*, 830(2):55, oct 2016. doi: 10.3847/0004-637X/830/2/55.

[109] D. Shapira, R.M. Devries, H.W. Fulbright, J. Tōke, and M.R. Clover. The Rochester Heavy Ion Detector. *Nuclear Instruments and Methods*, 129(1):123–130, 1975. ISSN 0029-554X. doi: https://doi.org/10.1016/0029-554X(75)90121-4.

Vita

Sudarsan Balakrishnan was born in Ernakulam, India in 1992. He graduated 12th grade from SBOA Public School, Ernakulam in 2010. Thereafter, he attended IIT Madras, India to graduate with honors in 2015, earning an integrated BS&MS in Physics. After a brief stint working as a project assistant in an optics lab, a curiosity to see quantum-mechanics problems in action and to explore his liking for signal-processing electronics lead him to pursue a Ph.D. in Experimental Nuclear Astrophysics at Louisiana State University in 2016. He hopes to continue pursuing both these interests going forward.